University of California
Santa Barbara

Topics in Modeling of Cochlear Dynamics: Computation, Response and Stability Analysis

A Thesis submitted in partial satisfaction
of the requirements for the degree

Master of Science
in
Mechanical Engineering

by

Maurice G. Filo

Committee in charge:

Professor Bassam Bamieh, Chair
Professor Frederic Gibou
Professor Igor Mezic

Month 2017

The Thesis of Maurice G. Filo is approved.

Professor Frederic Gibou

Professor Igor Mezic

Professor Bassam Bamieh, Committee Chair

Month 2017

Topics in Modeling of Cochlear Dynamics: Computation, Response and Stability Analysis

Maurice G. Filo

Abstract

Topics in Modeling of Cochlear Dynamics: Computation, Response and Stability Analysis

by

Maurice G. Filo

This thesis touches upon several topics in cochlear modeling. Throughout the literature, mathematical models of the cochlea vary according to the degree of biological realism to be incorporated. This thesis casts the cochlear model as a continuous space-time dynamical system using operator language. This framework encompasses a wider class of cochlear models and makes the dynamics more transparent and easier to analyze before applying any numerical method to discretize space. In fact, several numerical methods are investigated to study the computational efficiency of the finite dimensional realizations in space. Furthermore, we study the effects of the active gain perturbations on the stability of the linearized dynamics. The stability analysis is used to explain possible mechanisms underlying spontaneous otoacoustic emissions and tinnitus. On a different page, Dynamic Mode Decomposition (DMD) is introduced as a useful tool to analyze the response of nonlinear cochlear models. Cochlear response features are illustrated using DMD which has the advantage of explicitly revealing the spatial modes of vibrations occurring in the Basilar Membrane (BM). Finally, we address the dynamic estimation problem of BM vibrations using Extended Kalman Filters (EKF). Due to the limitations of noninvasive sensing schemes, such algorithms are inevitable to estimate the dynamic behavior of a living cochlea.

Contents

Abstract **iv**

List of Figures **vii**

List of Tables **xi**

1 Introduction & Brief Physiology **1**

2 Mathematical Model **5**
2.1 Model Dynamics 5
2.2 The Cochlear Model as an Infinite Dimensional Distributed System: Operator Approach 11

3 Numerical Realizations **13**
3.1 Finite Difference Method 13
3.2 Chebyshev Collocation Method 16
3.3 Spectral Method: Basis Expansion 17
3.4 Numerical Experiments on the Fluid Boundary Value Problem 21
3.5 Frequency Response Using Different Numerical Methods 23

4 Possible Sources of Instability in the Cochlea **29**
4.1 System Linearization 30
4.2 Stability Effect of the Gain Level 30
4.3 Stability Effect of Rapid Spatial Perturbations 30
4.4 Limit Cycles of the Nonlinear Model 39

5 Cochlear Dynamic Mode Decomposition **43**
5.1 Linear Algebra Preliminaries 43
5.2 Review on DMD 45
5.3 Cochlear Response Features using DMD 46
5.4 Conclusion 53

6 Estimating Basilar Membrane Vibration using Extended Kalman Filters **54**
6.1 Kalman Filter Framework in Distributed Environments 54
6.2 System Linearization 56
6.3 Numerical Results and Analysis 58

Bibliography **64**

List of Figures

1.1 Ear Anatomy 2
1.2 (a) Stretched Cochlea (b) Cochlear Partition 3

2.1 Model of the Stretched Cochlea 7
2.2 Boundary Value Problem 8
2.3 Model of the Cochlear Partition 9

3.1 Finite Difference Spatial Grid 15
3.2 Finite realization error of the fluid mass operator $\mathcal{M}_f$. The error is computed through the action of $\mathcal{M}_f$ on three different inputs shown in the first row. The second row shows the behavior of the error, for each input, as N_x is varied using the finite difference and Chebyshev collocation methods. The third and fourth rows depict the effect of the grid size N_x and the number of basis functions p on the finite realization error while using the trapezoidal and Clenshaw-Curtis quadratures for integration, respectively. 24
3.3 Finite realization error of the fluid mass operator $\mathcal{M}_f$ similar to Figure 3.2 but for three different test inputs with higher spatial variations. 25
3.4 Frequency Response relating the basilar membrane displacement u at a location x to the pressure at the eardrum p_e. 26
3.5 Frequency response error of the different numerical methods. The error is calculated as the deviation of the transfer function given in 3.22, as realized by each numerical method with 150 grid points, from the exact transfer function. The exact transfer function is approximated by a finite difference method with a very fine grid. 27
3.6 Frequency response error of the different numerical methods. The error is calculated as the deviation of the transfer function given in 3.22, as realized by each numerical method with 90 grid points, from the exact transfer function. The exact transfer function is approximated by a finite difference method with a very fine grid. 28

4.1 Sweeping the level of the active gain from 0 to 1 but remaining spatially constant. 31

4.2 Locus of the eigenvalues of the linearized cochlear dynamics as γ_0 varies from 0 (no active gain) up to 1 (full active gain). The Figure on the top shows the eigenvalues for different values of γ_0. The magenta crosses corresponds to $\gamma_0 = 0$, the blue dots corresponds to the range of γ_0 where the system is stable. The black asterisks correspond to $\gamma_0 = 0.89$ where the eigenvalues first cross to the right half plane rendering the system unstable. Finally, the red dot correspond to the range of γ_0 where the system is unstable ending with red circles for $\gamma_0 = 1$. 32
4.3 Magnitude and phase of the unstable mode of the linearized cochlear dynamics when $\gamma_0(x) = 0.89$. 33
4.4 Rapid spatial perturbation imposed at $x = 1.25cm$ on the gain profile $\gamma_0(x)$. ϵ denotes an arbitrary small number. 33
4.5 Frequency to location mapping. This intensity plot depicts the frequency response of the linearized cochlear dynamics for $\gamma_0(x) = 1$ as shown in equation (3.22) such that $\omega = 2\pi f$ with f denoting the frequency in kHz. The peaks of the intensity plot correspond to the characteristic frequency (CF) of each location. The CF of $x = 1.25cm$ is $3.6kHz$. 34
4.6 Perturbation of the eigenvalues of the linearized cochlear dynamics due to a rapid spatial perturbation of the gain function $\gamma_0(x)$ at location $x = 1.25cm$ whose characteristic frequency (CF) is $3.6kHz$. The plot to the left shows the eigenvalues of the unperturbed dynamics along with the velocities of the eigenvalues as the gain function is perturbed as shown in Figure 4.4. The plot to the right zooms in to the large velocity vectors. . 36
4.7 Distribution of eigenvalues for the linearized cochlear dynamics with a spatially perturbed active gain as shown in Figure 4.4 where $\epsilon = 0.01$. . 37
4.8 Unstable modes of the linearized cochlear dynamics with a spatially perturbed active gain as shown in Figure 4.4 where $\epsilon = 0.01$. 37
4.9 Rapid spatial perturbation imposed at $x = x_p cm$ on the gain profile $\gamma_0(x)$. ϵ denotes the intensity of the perturbation and γ_{max} denotes the maximum gain. 38
4.10 Instabilities caused by perturbations at different locations x_p for different values of γ_{max}. The value of ϵ indicates the minimum perturbation that causes instabilities around the corresponding location on the basilar membrane. 38
4.11 Temporal evolution of the basilar membrane profile without any input. The nonlinear model (2.11) was used to generate this plot with $\gamma_0(x) = 1$. A Limit cycle is born at the apical location ($x = 2.41cm$) of the unstable mode peak of the linearized dynamics shown in Figure 4.3. 39

4.12 Basilar membrane vibration at the location $x = 2.41cm$ with a characteristic frequency of $250Hz$. The Figure at the top shows the temporal evolution. That at the bottom shows the Fourier transform that confirms that the vibration has a frequency equal to the characteristic frequency at that location. 40
4.13 Temporal evolution of the basilar membrane profile without any input but with a spatial perturbation of the active gain $\gamma_0(x)$ as shown in Figure 4.9. The nonlinear model (2.11) was used to generate this plot with $\gamma_{max} = 1$, $\epsilon = 0.001$ and $x_p = 1.25cm$. A Limit cycle is born at the perturbed location ($x_p = 1.25cm$). 41
4.14 Basilar membrane vibration at the perturbed location $x = 1.25cm$ whose characteristic frequency is $3.6kHz$. The Figure at the top shows the temporal evolution. That at the bottom shows the Fourier transform that confirms that the vibration has a frequency equal to the characteristic frequency at that location in addition to the other close frequencies that are shown in Figure 4.7. 41
4.15 Basilar membrane vibration at the perturbed location $x = 1.25cm$ whose characteristic frequency is $3.6kHz$ for three different values of ϵ. The Figure at the top shows the temporal evolution. That at the bottom shows the Fourier transform. 42

5.1 Comparison between the Fourier transform and DMD. Figure (a) shows the Fourier transform of the vibrations everywhere on the basilar membrane. Figure(b) shows the ten most prominent (in magnitude) dynamic modes of vibration. Figure (c) overlays the Fourier transform and DMD at the corresponding frequencies. 49
5.2 The detuning phenomenon. The most dominant dynamic mode is extracted from simulations with a pure tone stimulus at $4.1kHz$ for different dB intensity levels ranging from $0dB$ which corresponds to the threshold of hearing up to $120dB$. 50
5.3 Frequency to location map of the nonlinear cochlear model at different dB intensity levels of the stimulus. 51
5.4 Dominant dynamic modes of the basilar membrane vibrations in the absence of a stimulus for $\gamma_0(x) = 0.95 + 0.05h(x - 1.25)$. 51
5.5 Dominant dynamic mode of the basilar membrane vibrations in the absence of a stimulus for $\gamma_0(x) = 0.9 + 0.1h(x - 1.25)$. 52
5.6 Dominant dynamic modes of the basilar membrane vibrations for a stimulus of two tones of 7 and $10kHz$ at $60dB$. 53

6.1 Snapshots of the true and estimated basilar membrane displacement profile. The figure to the top shows the true initial condition which is zero but assumed to be unknown. The estimated initial condition is randomly generated to asses the response of the extended Kalman filter to uncertain initial conditions. The subsequent figures show three snapshots of the BM displacement profile at $t = 0.1, 0.5$ and 3ms, respectively. 60
6.2 The evolution of the estimation error in the presence and absence of measurements. 61
6.3 Comparison of the relative estimation error for different number of measurements. 61
6.4 Estimation performance of the extended Kalman filter with a coarse spatial grid. (a) Snapshots of the true and estimated basilar membrane displacement profile. (b) The evolution of the estimation error in the presence and absence of measurements. 62
6.5 Estimation performance of the extended Kalman filter with defected parameters. (a) Snapshots of the true and estimated basilar membrane displacement profile. (b) The evolution of the estimation error in the presence and absence of measurements. 63

List of Tables

2.1 Parameter Description and Numerical Values 6

Chapter 1

Introduction & Brief Physiology

The physiological basis for cochlear sound processing continues to attract increased attention particularly with the advent of in vivo recordings in living animals ([1], [2], [3], [4]). Early in the past century (1937), the physical understanding of sound processing in the mammalian ear, particularly the cochlea, lead to the development of the nowclassical audio frequency decompositions (the Mel spectrum) which had a salient impact in the automated processing, storage, and understanding of sound signals ([5], [6], [7], [8]). It also became clear that even at this early stage of the auditory stream, sound pressure waves undergo active and nonlinear processing that impart an increased sensitivity to low amplitude sounds and an exquisite frequency selectivity in mechanical vibration that are subsequently transduced into the electrical signals traveling along the auditory nerve ([9], [10], [11], [12]). Moving higher in the auditory stream, several experiments looked into the neural signatures of sound features, such as pitch and complex tones in the auditory cortex ([13], [14], [15]).

With continuing investigation of the auditory pathways and availability of data, the introduction of efficient modeling of the various subsystems involved has become increasingly valuable both for scientific discovery and engineering. In addition to guiding experimental design, deciphering key players in audio perception can potentially impact the development of novel signal processing tools that increase the naturalness and robustness of sounds in audio applications.

This thesis touches upon several topics on the cochlea varying from mathematical modeling to numerical methods and stability analysis. Furthermore, tools such as Dynamic Mode Decomposition (DMD) and Kalman filters are employed as means of analyzing cochlear response. First, in chapter 2, we reformulate an existing class of cochlear models in a continuous space-time, descriptor state space form using operator language. This form has two advantages: (a) it encompasses a wider class of cochlear models and (b) it makes the dynamics more transparent and easier to analyze before applying any numerical method (that is, before discretizing space). In chapter 3, we investigate different numerical methods that realize the various spatial operators of the mathematical model. With the numerical methods in hand, we study the possible sources of instabilities in

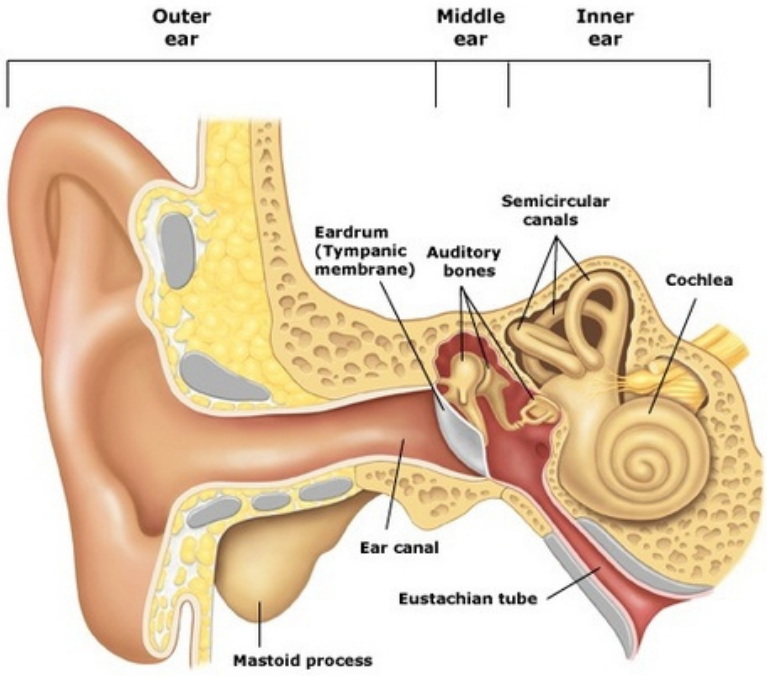

Figure 1.1: Ear Anatomy

chapter 4. In chapter 5, we show that Dynamic Mode Decomposition (DMD) is a useful tool to analyze cochlear response. Finally, in chapter 6, we apply the extended Kalman filter as a means of estimating the basilar membrane vibrations assuming we are given a set of measurements.The rest of this chapter gives a brief exposé of the physiology of the ear as an adaptive transduction device. For a more thorough reading on the physiology of the ear, we refer the reader to [16].

The primate ear is built to adapt for different sound intensity levels and across the entire audible frequency range (20Hz to 20 kHz). It is composed anatomically, of three principal parts: outer, middle and inner ear (refer to Figure 1.1). The outer ear is mainly composed of the pinna and the external auditory canal. The pinna collects and transforms the sound waves and plays a role in sound source localization. The external auditory canal serves as a filter, which resonates and amplifies tones ranging between 3 and 4 kHz. The middle ear is mainly composed of the ear drum (tympanic membrane), the ossicles and the neighboring cavity. Sound pressure waves pass through the external ear canal and reach the eardrum causing it to vibrate. The neighboring cavity balances the pressure between the middle and outer ear thus preventing eardrum vibrations in the absence of sound waves. Induced eardrum vibrations are then transmitted to the inner ear via three bone structures (ossicles) that collectively act both as an amplifier of the vibration force and as an impedance matching device between the air medium (middle

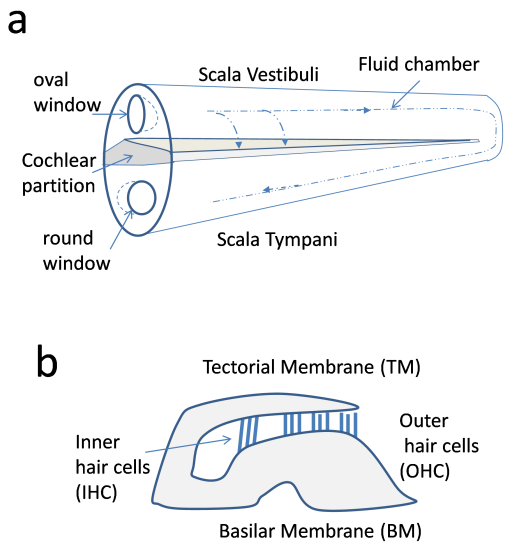

Figure 1.2: (a) Stretched Cochlea (b) Cochlear Partition

ear) and fluid medium (inner ear) thus preventing excessive energy loss as waves travel between the two different media. In the inner ear, the cochlea is the organ where the main nonlinear biomechanical processing takes place. It is a sensory organ where sound signals are transformed into electrical signals. The cochlea is divided into two chambers: Scala Vestibuli (SV) and Scala Tympani (ST) filled with incompressible fluid and are partly separated by the cochlear partition (refer to Figure). At one end of the SV, the oval window acts as an entry port where pressure waves arriving from the stapes of the middle ear enter the inner ear. These waves travel along the SV and enter the second chamber ST through a connection point (Helicotrema). Finally, a round window at the other end of the ST serves to release pressure traveling in the incompressible fluid. As the pressure waves travel along the two chambers, fluid pressure fluctuations permeate the first wall of the cochlear partition to cause vibrations in two connected wall structures termed the tectorial membrane (TM) and basilar membrane (BM). Anchored in the BM are rows of thin cells termed inner and outer hair cells which are moved as the two membranes vibrate in different directions. The inner hair cells are the main nerve cells that transduce the mechanical vibrations to electrical impulses. Finally, the outer hair cells act to amplify vibrations specifically under low pressure fluctuations. The mechanical characteristics of the BM varies along its length from being narrow and stiff at the oval window (entry point) to being wide and compliant at the apex. This party endows the cochlea with spatially-tuned resonances: lower frequencies cause slow vibrations closer to the apex while higher frequencies are closer to the oval window. Other factors that contribute to cochlear response include dynamics of the fluid and active feedback of the outer hair

cells.

Chapter 2

Mathematical Model

This chapter develops the details of the mathematical model. After describing the governing dynamics, the mathematical model is recast in a continuous space-time, descriptor form using operator language. The mathematical model in this thesis is based on [17]. However, our operator reformulation encompasses a wider class of cochlear models ([18], [19], [20], [21] among others). First, we present Table 2.1 that summarizes the model parameters with their numerical values that are going to be used throughout the thesis.

2.1 Model Dynamics

This section sequentially introduces the mechanical stages that describe the propagation of the vibrations in the ear. The dynamics of the middle ear is first given. Then the macro and micro-mechanical stages are introduced along with the mathematical model of the active gain.

2.1.1 Middle Ear

Starting with the middle ear, a second order mass-damping-spring system (2.1) is utilized to model air wave transformation and amplification, prior to its injection to the inner ear at the oval window (stapes). The input to the middle ear is the pressure at the ear drum, and the output is the displacement of the stapes.

$$\begin{aligned} p_e(t) &= m_m \ddot{s}(t) + c_m \dot{s}(t) + k_m s(t) \\ \dot{s}(0) &= s(0) = 0 \end{aligned} \tag{2.1}$$

where $s(t)$ is the acceleration of the stapes, $p_e(t)$ is the air pressure wave at the ear drum, and m_m, c_m and k_m are the mass, damping and stiffness factors of the middle ear respectively. Note that the terminologies, description and numerical values of the model parameters are given in Table 2.1. Arriving at the inner ear, a macro-mechanical

Symbols	Description	Numerical Values	Units
m_m	Mass per unit area of the middle ear	6.7×10^{-3}	$g.cm^{-2}$
c_m	Damping per unit area of the middle ear	2.36×10^{2}	$dyn.s.cm^{-3}$
k_m	Stiffness per unit area of the middle ear	4.23×10^{6}	$dyn.cm^{-3}$
H	Height of the extended cochlea	0.1	cm
L	Length of the extended cochlea	2.5	cm
ρ	Cochlea fluid density	0.1	$g.cm^{-3}$
N_x	Number of grid points along the BM/TM		
N_y	Number of grid points along the fluid chamber		
Δx	Discretization step along the BM/TM		cm
Δy	Discretization step along the fluid chamber		cm
x	Spatial variable along the length of the extended cochlea		cm
y	Spatial variable along the height of the extended cochlea		cm
m_1	Mass per unit area of the BM	3×10^{-3}	$g.cm^{-2}$
m_2	Mass per unit area of the TM	5×10^{-2}	$g.cm^{-2}$
$c_1(x)$	Damping per unit area at location x of the BM	$2e^{-0.2773x}(20 + 1500e^{-2x})$	$dyn.s.cm^{-3}$
$c_2(x)$	Damping per unit area at location x of the TM	$2e^{-0.2773x}(10e^{-2.2x})$	$dyn.s.cm^{-3}$
$c_3(x)$	BM/TM coupled damping per unit area at location x	$2e^{-0.2773}(2e^{-0.8x})$	$dyn.s.cm^{-3}$
$c_4(x)$	Active damping per unit area at location x	$2e^{-0.2773x}(1040e^{-2x})$	$dyn.s.cm^{-3}$
$k_1(x)$	Stiffness per unit area at location x of the BM	$1.1 \times 10^{9}e^{-4x}$	$dyn.cm^{-3}$
$k_2(x)$	Stiffness per unit area at location x of the TM	$7 \times 10^{6}e^{-4.4x}$	$dyn.cm^{-3}$
$k_3(x)$	BM/TM coupled stiffness per unit area at location x	$1 \times 10^{7}e^{-4x}$	$dyn.cm^{-3}$
$k_4(x)$	Active stiffness per unit area at location x	$6.15 \times 10^{8}e^{-4x}$	$dyn.cm^{-3}$
θ	Nonlinearity coupling factor	0.5	
λ	Spreading factor	0.08	cm
P_{ref}	Pressure reference at the threshold of hearing	2×10^{-4}	$dyn.cm^{-2}$
R	BM displacement normalization factor	1×10^{-7}	cm
$u(x,t)$	BM displacement at location x at time t		cm
$v(x,t)$	TM displacement at location x at time t		cm
$s(t)$	Stapes displacement at time t		cm
p_e	Pressure at the ear drum at time t		$dyn.cm^{-2}$
$p(x,y,t)$	Fluid pressure difference at location (x,y)		$dyn.cm^{-2}$
$\gamma_0(x)$	Linearized active gain profile at location x		

Table 2.1: Parameter Description and Numerical Values

and a micro-mechanical stage are introduced to produce BM vibrations in the cochlear partition as detailed next.

2.1.2 Macro-Mechanical Stage

This stage models the fluid dynamics responding to the vibration of the stapes. The cochlea has a spiral shape; however, for simplification purposes, it is stretched and rectified to become a rectangular shape as shown in Figure 2.1. Let $p_f(x, y, t)$ represent the fluid pressure at location (x, y) at time t. Thus the pressure difference is $(x, y, t) = p_f(x, y, t) - p_f(x, y, t)$. Since, $p(x, -y, t) = -p(x, y, t)$ and the model deals with the pressure difference rather than the pressure itself, the model can be simplified to only one chamber as illustrated in Figure 2.1. Linearizing the Navier-Stokes equations

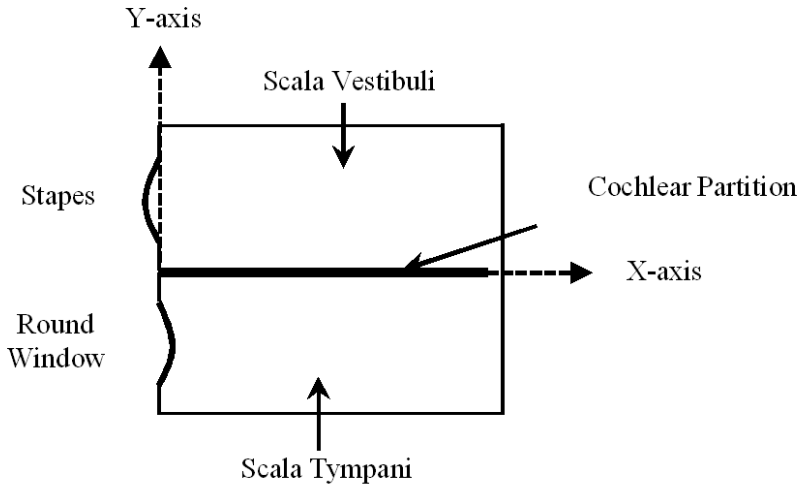

Figure 2.1: Model of the Stretched Cochlea

under the assumptions that the fluid is incompressible, inviscid and the vibrations of the cochlear partitions are negligible with respect to the cochlear dimensions, we arrive at a boundary value problem (summarized in Figure 2.2) where the Laplacian of the pressure difference inside the simplified chamber is zero. Here, the Basal wall at $(x = 0)$ is moving with the stapes and the chamber floor at $(y = 0)$ is moving with the BM. Therefore, the pressure variation along the x-axis (y-axis) is dependent on the force acting on the stapes (BM), respectively. On the other hand, the upper wall is considered to be rigid thus the vertical variation of the pressure difference is zero. Finally, the boundary at $(x = L)$ is considered to be a pressure release end. For future reference, the boundary

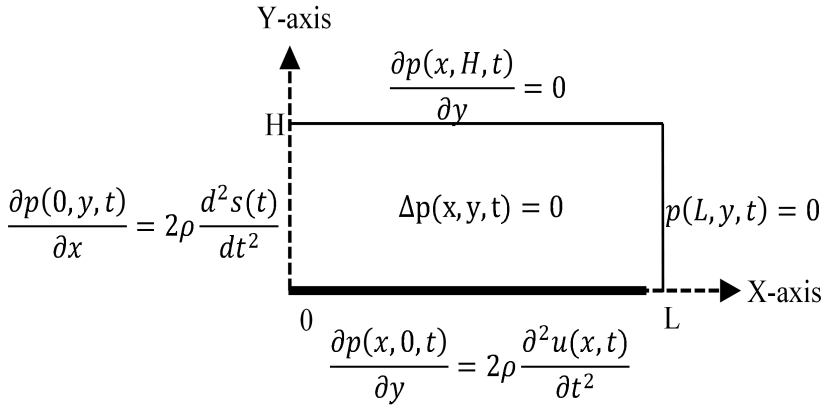

Figure 2.2: Boundary Value Problem

value problem is summarized in (2.2).

$$\begin{aligned}
(\frac{\partial^2}{\partial x^2} + \frac{\partial^2}{\partial y^2})p(x,y,t) &= 0 \\
\frac{\partial}{\partial x}p(0,y,t) &= 2\rho\frac{d^2}{dt^2}s(t) \\
p(L,y,t) &= 0 \\
\frac{\partial}{\partial y}p(x,0,t) &= 2\rho\frac{\partial^2}{\partial t^2}u(x,t) \\
\frac{\partial}{\partial y}p(x,H,t) &= 0
\end{aligned} \tag{2.2}$$

2.1.3 Micro-Mechanical Stage

This stage governs the dynamics of the cochlear partition represented by the two lumped membranes: the tactorial and basilar membranes. Figure 2.3 shows the model which is comprised of two arrays of second order mass-damper-spring systems decoupled horizontally but locally coupled vertically. This stage responds to the pressure difference that resulted from the Macro-Mechanical stage. Note that although individual systems in the array are decoupled horizontally, the coupling does exist via the fluid pressure within the cochlear partition and in the two chambers. The resultant system of equations is written in matrix form in (2.3).

$$m_P\frac{\partial^2}{\partial t^2}\xi(x,t) + c_P(x)\frac{\partial}{\partial t}\xi(x,t) + k_P(x)\xi(x,t) = F_P(x,t) \tag{2.3}$$

where

$$\xi(x,t) = \begin{bmatrix} u(x,t) \\ v(x,t) \end{bmatrix} \quad F_P(x,t) = \begin{bmatrix} p(x,0,t) \\ 0 \end{bmatrix} \quad m_P = \begin{bmatrix} m_1 & 0 \\ 0 & m_2 \end{bmatrix}$$

$$c_P(x) = \begin{bmatrix} c_1(x) + c_3(x) & -c_3(x) \\ -c_3(x) & c_2(x) + c_3(x) \end{bmatrix} \quad k_P(x) = \begin{bmatrix} k_1(x) + k_3(x) & -k_3(x) \\ -k_3(x) & k_2(x) + k_3(x) \end{bmatrix}$$

$u(x,t)$ and $v(x,t)$ are the BM and TM displacements, respectively. As seen earlier,

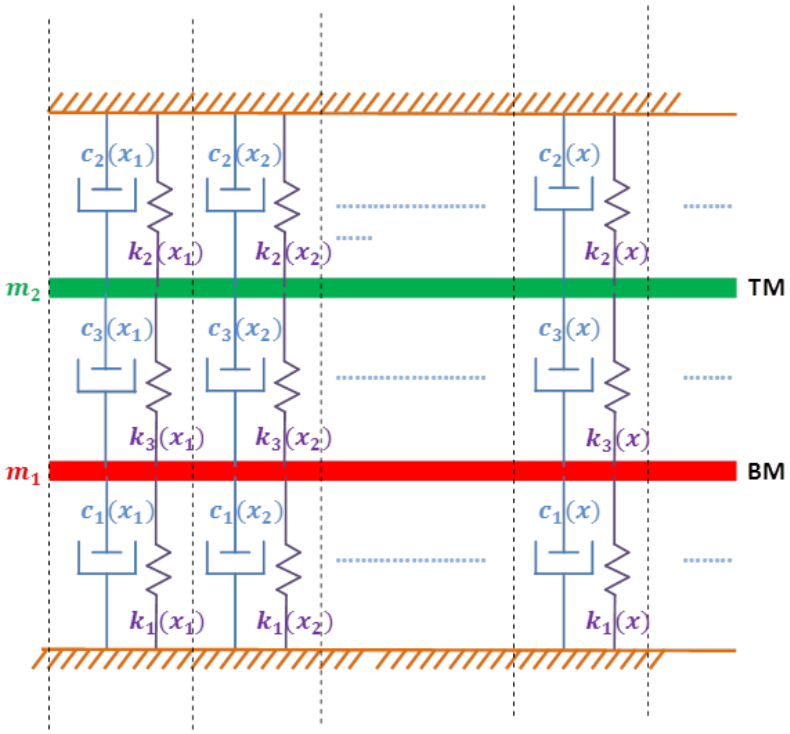

Figure 2.3: Model of the Cochlear Partition

the fluid pressure is applied on the cochlear partition. This corresponds to the passive excitation of the latter. To account for the Outer Hair cells which are responsible for the active nature of the cochlea, another active force term is introduced to (2.3). This active force depends on the difference between the TM/BM displacements and velocities and is shown in (2.4).

$$F_A(x,t) = \begin{bmatrix} \gamma \left[c_4(x) \frac{\partial}{\partial t} + k_4(x) \right] [u(x,t) - v(x,t)] \\ 0 \end{bmatrix} \tag{2.4}$$

Including the active term in the passive micro-mechanical model shown in (2.3) yields the active micro-mechanical model shown in (2.5).

$$m_p \frac{\partial^2}{\partial t^2}\xi(x,t)+[c_p(x)-\gamma c_A(x)]\,\frac{\partial}{\partial t}\xi(x,t)+[k_p(x)-\gamma k_A(x)]\,\xi(x,t)=F_p(x,t) \qquad x\in[0,L] \tag{2.5}$$

where

$$c_A(x)=\begin{bmatrix} c_4(x) & -c_4(x) \\ 0 & 0 \end{bmatrix} \qquad k_A(x)=\begin{bmatrix} k_4(x) & -k_4(x) \\ 0 & 0 \end{bmatrix}$$

γ is the active gain which is allowed to vary in a nonlinear nonlocal fashion depending on the BM profile.

2.1.4 Nonlinear Active Gain

The active gain γ is mathematically constructed to capture three essential features of the cochlear response.

- Compressive nonlinearity: the active gain should be high for small vibrations and low for large vibrations.
- Critical bands: the active gain at location x depends not only on the vibration at location x, but also on a range (critical band) centered around location x.
- Distortion products: the active gain should create harmonic frequencies. That is, the vibrations at locations x do not oscillate at a single frequency (natural frequency of location x), but also has different frequencies.

A suggested model for the active gain is given by equation (2.6).

$$\begin{aligned} \gamma(x,t) &= \frac{\gamma_0(x)}{1+\theta\tilde{u}(x,t)} \\ \tilde{u}(x,t) &= \frac{\int_0^L e^{\frac{-(x-s)^2}{\lambda^2}}\frac{u^2(s,t)}{R^2}ds}{\int_0^L e^{\frac{-(x-s)^2}{\lambda^2}}ds} \end{aligned} \tag{2.6}$$

where λ, θ and R are constants. Moreover, $\gamma_0(x)$ is the full gain profile. That is, when the basilar membrane is not moving, the active gain is at full throttle $\gamma(x,t)=\gamma_0(x)$. The full gain is typically taken to be unity i.e. $\gamma_0(x)=1$. Note that the integral in the denominator is a normalization factor.

2.2 The Cochlear Model as an Infinite Dimensional Distributed System: Operator Approach

In this section, we reformulate the model, that was previously developed, using operators. This formulation is easier to write down and analyze since it is independent of the numerical method used to solve the macro-mechanical stage. Furthermore, the linearization of the model in operator form is easier to carry out. The pressure $p(x,0,t)$ at the BM can be thought of as the solution of the macro-mechanical stage given by (2.2). As a matter of fact, $p(x,0,t)$ can be seen as the output of a linear time invariant system with a scalar input: stapes acceleration $\ddot{s}(t)$ and a distributed input: BM acceleration $\ddot{u}(x,t)$. Therefore, the pressure can be written as a superposition of two linear operators acting on the inputs: $p(x,0,t) = -\left(\mathcal{M}_s(\ddot{s}) + \mathcal{M}_f(\ddot{u})\right)$, where:

$$\begin{aligned} \mathcal{M}_s : \mathbb{R} &\to \mathbb{L}_2\left([0,L]\right) \\ \ddot{s} &\mapsto \mathcal{M}_s(\ddot{s}) \\ \mathcal{M}_f : \mathbb{L}_2\left([0,L]\right) &\to \mathbb{L}_2\left([0,L]\right) \\ \ddot{u} &\mapsto \mathcal{M}_f(\ddot{u}) \end{aligned} \tag{2.7}$$

such that $p(x,0,t) = -[\mathcal{M}_s(\ddot{s})](x,t) - [\mathcal{M}_f(\ddot{u})](x,t)$ solves (2.2). $\mathcal{M}_s$ and $\mathcal{M}_f$ are operators that correspond to the mass effect of the stapes and fluid on the BM. Hence we term $\mathcal{M}_f$ and $\mathcal{M}_s$ as the fluid mass and stapes mass operators, respectively. The complete model of the cochlea shown in equations (2.5) and (2.6) can thus be written as:

$$\begin{aligned} &\begin{bmatrix} m_1 & 0 \\ 0 & m_2 \end{bmatrix} \begin{bmatrix} \ddot{u} \\ \ddot{v} \end{bmatrix} + \begin{bmatrix} c_1 + c_3 - \gamma(u)c_4 & \gamma(u)c_4 - c_3 \\ -c_3 & c_2 + c_3 \end{bmatrix} \begin{bmatrix} \dot{u} \\ \dot{v} \end{bmatrix} \\ &\qquad + \begin{bmatrix} k_1 + k_3 - \gamma(u)k_4 & \gamma(u)k_4 - k_3 \\ -k_3 & k_2 + k_3 \end{bmatrix} \begin{bmatrix} u \\ v \end{bmatrix} = - \begin{bmatrix} \mathcal{M}_s(\ddot{s}) + \mathcal{M}_f(\ddot{u}) \\ 0 \end{bmatrix} \\ &\qquad [\gamma(u)]\,(x) = \frac{\gamma_0(x)}{1 + \theta\left[\mathcal{G}_\lambda\left(\frac{u^2}{R^2}\right)\right](x)} \end{aligned} \tag{2.8}$$

Note that we dropped the spatial and temporal variables (x and t, respectively) where necessary for convenience. $\mathcal{M}_s$ and $\mathcal{M}_f$ are spatial linear time invariant operators that solve the macro-mechanical stage. $\mathcal{G}_\lambda$ is a linear operator that performs a normalized Gaussian weighing.

$$\begin{aligned} \mathcal{G}_\lambda : \mathbb{L}_2\left([0,L]\right) &\to \mathbb{L}_2\left([0,L]\right) \\ u &\mapsto \mathcal{G}_\lambda(u) := \frac{\int_0^L e^{\frac{-(x-s)^2}{\lambda^2}} u(s,t)ds}{\int_0^L e^{\frac{-(x-s)^2}{\lambda^2}} ds} \end{aligned} \tag{2.9}$$

Note that $\mathbb{L}_2\left([0,L]\right)$ is the space of square integrable functions defined on $[0,L]$.

By defining the state space variable to be:

$$\psi := \begin{bmatrix} u \\ v \\ \dot{u} \\ \dot{v} \end{bmatrix} \tag{2.10}$$

the system (2.8) can be recast in descriptor state space form as follows:

$$\mathcal{E}\frac{\partial}{\partial t}\psi = \mathcal{A}_u\psi + \mathcal{B}\ddot{s} \tag{2.11}$$

where $\mathcal{E}$, $\mathcal{A}_u$ and $\mathcal{B}$ are matrices of operators defined as follows:

$$\mathcal{E} := \begin{bmatrix} \mathcal{I} & 0 & 0 & 0 \\ 0 & \mathcal{I} & 0 & 0 \\ 0 & 0 & m_1\mathcal{I} + \mathcal{M}_f & 0 \\ 0 & 0 & 0 & m_2\mathcal{I} \end{bmatrix} \quad \mathcal{B} := \begin{bmatrix} 0 \\ 0 \\ -\mathcal{M}_s \\ 0 \end{bmatrix} \quad [\gamma(u)](x) = \frac{\gamma_0(x)}{1 + \theta\left[\mathcal{G}_\lambda\left(\frac{u^2}{R^2}\right)\right](x)}$$

$$\mathcal{A}_u := \begin{bmatrix} 0 & 0 & \mathcal{I} & 0 \\ 0 & 0 & 0 & \mathcal{I} \\ \gamma(u)k_4 - (k_1 + k_3) & k_3 - \gamma(u)k_4 & \gamma(u)c_4 - (c_1 + c_3) & c_3 - \gamma(u)c_4 \\ k_3 & -(k_2 + k_3) & c_3 & -(c_2 + c_3) \end{bmatrix}$$

$\mathcal{I}$ is the identity operator. It is worth to emphasize here that $\mathcal{E}$ and $\mathcal{B}$ are linear operators, but $\mathcal{A}_u$ is a nonlinear operator that depends on the BM displacement u expressed as its subscript.

Chapter 3

Numerical Realizations

Capturing sharp cochlear response often demands relatively high computational efforts. Particularly, if cochlear models are to be used for audio signal processing, the computational load of simulations becomes critical. For such reasons, efficient numerical methods were devised to march simulations of the cochlea in time [22]. Furthermore, model order reduction techniques [23] were used. However, less attention was given to numerical methods that treat the spatial variable. This chapter deals with the numerical methods to realize three spatial operators: (1) the stapes mass operator $\mathcal{M}_s$, (2) the fluid mass operator $\mathcal{M}_f$ and (3) the Gaussian weighing operator $\mathcal{G}_\lambda$ given in (2.7) and (2.9). Three different methods are explained: finite difference, Chebyshev collocation and a spectral method.

3.1 Finite Difference Method

To realize the operators using a finite difference method, we first lay down an $(N_x + 1) \times (N_y + 1)$ two dimensional grid as shown in Figure 3.1. Thus

$$\begin{aligned} x_i &= i\Delta x \qquad \Delta x = \frac{L}{N_x} \qquad i = 0, 1, 2, ..., N_x \\ y_j &= j\Delta y \qquad \Delta y = \frac{H}{N_y} \qquad j = 0, 1, 2, ..., N_y \end{aligned}$$

Discretizing (2.2) in space using central difference approximations of the first and second spatial derivatives with careful incorporation of the boundary conditions, we obtain a second order finite difference scheme summarized as follows:

$$A_{FD} P_{FD}(t) = b_{FD}(t) \tag{3.1}$$

where $\Delta = \Delta_x^2 + \Delta_y^2$ and

$$A_{FD} = \frac{1}{\Delta x \Delta y}\begin{bmatrix} T & 2N & 0 & \cdots & \cdots & \cdots & \cdots & 0 \\ N & T & N & \ddots & & & & \vdots \\ 0 & N & T & N & \ddots & & & \vdots \\ \vdots & \ddots & \ddots & \ddots & \ddots & \ddots & & \vdots \\ \vdots & & \ddots & \ddots & \ddots & \ddots & \ddots & \vdots \\ \vdots & & & \ddots & N & T & N & 0 \\ \vdots & & & & \ddots & N & T & N \\ 0 & \cdots & \cdots & \cdots & \cdots & 0 & 2N & T \end{bmatrix} \quad P_{FD}(t) = \begin{bmatrix} P_{0,0}(t) \\ \vdots \\ P_{N_x+1,0}(t) \\ \vdots \\ \vdots \\ P_{0,N_y+1}(t) \\ \vdots \\ P_{N_x+1,N_y+1}(t) \end{bmatrix}$$

$$T = \begin{bmatrix} -2\Delta & 2\Delta_y^2 & 0 & \cdots & 0 \\ \Delta_y^2 & -2\Delta & \Delta_y^2 & \ddots & \vdots \\ 0 & \ddots & \ddots & \ddots & 0 \\ \vdots & \ddots & \Delta_y^2 & -2\Delta & \Delta_y^2 \\ 0 & \cdots & 0 & 0 & 1 \end{bmatrix} \qquad N = \Delta_x^2 \begin{bmatrix} 1 & 0 & 0 & \cdots & 0 \\ 0 & 1 & 0 & \ddots & \vdots \\ 0 & \ddots & \ddots & \ddots & 0 \\ \vdots & \ddots & 0 & 1 & 0 \\ 0 & \cdots & 0 & 0 & 0 \end{bmatrix}$$

$$b_{FD}(t) = 4\rho\left(\Delta_y S_2 \ddot{s}(t) + \Delta_x S_1^T \ddot{U}(t)\right)$$

$$U(t) = \begin{bmatrix} u(x_0,t) \\ u(x_1,t) \\ \vdots \\ u(x_{N_x},t) \\ u(x_{Nx+1},t) \end{bmatrix} \qquad S_1^T = \begin{bmatrix} \tilde{I} \\ 0 \\ \vdots \\ 0 \end{bmatrix} \qquad \tilde{I} = \begin{bmatrix} 1 & 0 & 0 & \cdots & 0 \\ 0 & 1 & 0 & \ddots & \vdots \\ 0 & \ddots & \ddots & \ddots & 0 \\ \vdots & \ddots & 0 & 1 & 0 \\ 0 & \cdots & 0 & 0 & 0 \end{bmatrix} \qquad S_2 = \begin{bmatrix} 1 \\ 1 \\ \vdots \\ 1 \end{bmatrix} \otimes \begin{bmatrix} 1 \\ 0 \\ \vdots \\ 0 \end{bmatrix}$$

Finally, the pressure at the lower boundary ($y = 0$),
$P_0(t) = \begin{bmatrix} P_{0,0}(t) & P_{1,0}(t) & \cdots & P_{N_x-1,0}(t) & P_{N_x,0}(t) \end{bmatrix}^T$ is given by:

$$P_0(t) = 4\rho S_1 A_{FD}^{-1}\left(\Delta_y S_2 \ddot{s}(t) + \Delta_x S_1^T \ddot{U}(t)\right) \tag{3.2}$$

Therefore, the operators $\mathcal{M}_s$ and $\mathcal{M}_f$ are realized by the matrices $M_s \in \mathbb{R}^{N_x+1}$ and $M_f \in \mathbb{R}^{(N_x+1)\times(N_x+1)}$, respectively, as follows:

$$\begin{aligned} M_s &= -4\rho\Delta_y S_1 A_{FD}^{-1} S_2 \\ M_f &= -4\rho\Delta_x S_1 A_{FD}^{-1} S_1^T \end{aligned} \tag{3.3}$$

Next, we construct a numerical realization of the linear operator $\mathcal{G}_\lambda$ so that the active gain in (2.6) can be efficiently calculated. Using the trapezoidal rule on the lower boundary of the mesh grid in Figure 3.1, we can calculate a realization $G_\lambda \in \mathbb{R}^{(Nx+1)\times(Nx+1)}$ of $\mathcal{G}_\lambda$

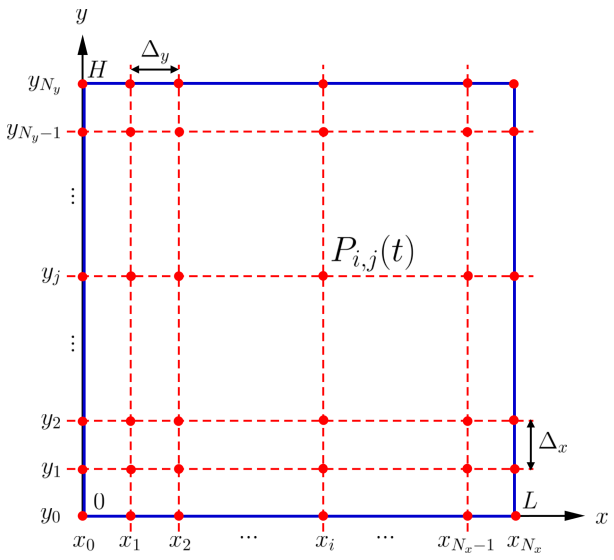

Figure 3.1: Finite Difference Spatial Grid

to approximate the integral in (2.9) as follows:

$$\tilde{u}(x,t) \approx \frac{\sum_{j=0}^{N_x} e^{\frac{-(i-j)^2\Delta_x^2}{\lambda^2}} \frac{u^2(s_j,t)}{R^2} \Delta_x w_j}{\sum_{j=0}^{N_x} e^{\frac{-(i-j)^2\Delta_x^2}{\lambda^2}} \Delta_x w_j}$$

$$= \frac{1}{\sum_{j=0}^{N_x} e^{\frac{-(i-j)^2\Delta_x^2}{\lambda^2}} \Delta_x w_j} \left[e^{-(i-0)^2\frac{\Delta_x^2}{\lambda^2}} \quad e^{-(i-1)^2\frac{\Delta_x^2}{\lambda^2}} \quad \cdots \quad e^{-(i-N_x+1)^2\frac{\Delta_x^2}{\lambda^2}} \quad e^{-(i-N_x)^2\frac{\Delta_x^2}{\lambda^2}} \right] W \frac{U^2(t)}{R^2}$$

where w_j are the integration weights. For the trapezoidal rule, $w_j = 1$ everywhere except at the two boundaries where they are set to 0.5.

$$W = \begin{bmatrix} 0.5 & 0 & \cdots & \cdots & 0 \\ 0 & 1 & \ddots & & \vdots \\ \vdots & \ddots & \ddots & \ddots & \vdots \\ \vdots & & \ddots & 1 & 0 \\ 0 & \cdots & \cdots & 0 & 0.5 \end{bmatrix} \qquad U^2(t) = \begin{bmatrix} u^2(x_0,t) \\ u^2(x_1,t) \\ \vdots \\ u^2(x_{N_x-1},t) \\ u^2(x_{N_x},t) \end{bmatrix}$$

Now, define

$$\tilde{U}^2(t) = \begin{bmatrix} \tilde{u}^2(x_0,t) \\ \tilde{u}^2(x_1,t) \\ \vdots \\ \tilde{u}^2(x_{N_x-1},t) \\ \tilde{u}^2(x_{N_x},t) \end{bmatrix}$$

$$\tilde{G}_\lambda = \begin{bmatrix} e^{-(0-0)^2\frac{\Delta_x^2}{\lambda^2}} & e^{-(0-1)^2\frac{\Delta_x^2}{\lambda^2}} & \cdots & e^{-(0-N_x+1)^2\frac{\Delta_x^2}{\lambda^2}} & e^{-(0-N_x)^2\frac{\Delta_x^2}{\lambda^2}} \\ e^{-(1-0)^2\frac{\Delta_x^2}{\lambda^2}} & e^{-(1-1)^2\frac{\Delta_x^2}{\lambda^2}} & \cdots & e^{-(1-N_x+1)^2\frac{\Delta_x^2}{\lambda^2}} & e^{-(1-N_x)^2\frac{\Delta_x^2}{\lambda^2}} \\ \vdots & \vdots & & \vdots & \vdots \\ e^{-(N_x-1-0)^2\frac{\Delta_x^2}{\lambda^2}} & e^{-(N_x-1-1)^2\frac{\Delta_x^2}{\lambda^2}} & \cdots & e^{-(N_x-1-N_x+1)^2\frac{\Delta_x^2}{\lambda^2}} & e^{-(N_x-1-N_x)^2\frac{\Delta_x^2}{\lambda^2}} \\ e^{-(N_x-0)^2\frac{\Delta_x^2}{\lambda^2}} & e^{-(N_x-1)^2\frac{\Delta_x^2}{\lambda^2}} & \cdots & e^{-(N_x-N_x+1)^2\frac{\Delta_x^2}{\lambda^2}} & e^{-(N_x-N_x)^2\frac{\Delta_x^2}{\lambda^2}} \end{bmatrix}$$

Finally,

$$G_\lambda = diag\left(\tilde{G}_\lambda W.\vec{1}\right)^{-1}\tilde{G}_\lambda W \tag{3.4}$$

where $\vec{1}$ is a vector of ones and $diag(v)$ is a matrix with the vector v on its diagonal.

3.2 Chebyshev Collocation Method

To realize the operators using a Chebyshev collocation method, we lay down a two dimensional grid similar to that shown in Figure 3.1, but with a non-uniform step size as follows:

$$\begin{aligned} x_i &= \frac{L}{2}\left(1 - cos\left(\frac{\pi i}{N_x}\right)\right) \quad i = 0, 1, 2, ..., N_x - 1, N_x \\ y_i &= \frac{H}{2}\left(1 - cos\left(\frac{\pi j}{N_y}\right)\right) \quad j = 0, 1, 2, ..., N_y - 1, N_y \end{aligned} \tag{3.5}$$

Let D_x and D_y be the Chebyshev differential matrices in the x and y directions respectively. Hence (2.2) is discretized as follows:

$$\begin{aligned} \left[I_{N_y+1} \otimes D_x^2 + D_y^2 \otimes I_{N_x+1}\right] P_{CC}(t) &= 0 \\ \left[I_{N_y+1} \otimes (S_0^x D_x)\right] P_{CC}(t) &= 2\rho\vec{1}_{N_y+1}\ddot{s}(t) \\ \left[I_{N_y+1} \otimes S_L^x\right] P_{CC}(t) &= 0 \\ \left[(S_0^y D_y) \otimes I_{N_x+1}\right] P_{CC}(t) &= 2\rho\ddot{U}(t) \\ \left[(S_H^y D_y) \otimes I_{N_x+1}\right] P_{CC}(t) &= 0 \end{aligned} \tag{3.6}$$

where

$$S_0^x = \begin{bmatrix}1 & 0 & \cdots & 0\end{bmatrix}_{N_x+1} \qquad S_L^x = \begin{bmatrix}0 & \cdots & 0 & 1\end{bmatrix}_{N_x+1}$$
$$S_0^y = \begin{bmatrix}1 & 0 & \cdots & 0\end{bmatrix}_{N_y+1} \qquad S_H^y = \begin{bmatrix}0 & \cdots & 0 & 1\end{bmatrix}_{N_y+1}$$

$\otimes$ is the Kronecker product, I_{N_x+1} and I_{N_y+1} are the identity matrices with the corresponding sizes and $\vec{1}_{N_y+1}$ is the one vector with the corresponding size. Therefore the solution of (3.6) is given by

$$P_{CC}(t) = A_{CC}^{\dagger} b_{CC}$$

where † is the matrix pseudo-inverse and

$$A_{CC} = \begin{bmatrix} I_{N_y+1} \otimes D_x^2 + D_y^2 \otimes I_{N_x+1} \\ I_{N_y+1} \otimes (S_0^x D_x) \\ I_{N_y+1} \otimes S_L^x \\ (S_0^y D_y) \otimes I_{N_x+1} \\ (S_H^y D_y) \otimes I_{N_x+1} \end{bmatrix}$$

$$b_{CC} = 2\rho \begin{bmatrix} \vec{0}_{(N_x+1)(N_y+1)} \\ \vec{1}_{N_y+1} \\ \vec{0}_{N_y+1} \\ \vec{0}_{N_x+1} \\ \vec{0}_{N_x+1} \end{bmatrix} \ddot{s}(t) + 2\rho \begin{bmatrix} 0_{(N_x+1)(N_y+1)\times N_x+1} \\ 0_{N_y+1\times N_x+1} \\ 0_{N_y+1\times N_x+1} \\ I_{N_x+1} \\ 0_{N_x+1\times N_x+1} \end{bmatrix} \ddot{U}(t)$$

Therefore, the solution to (3.6) is given by

$$P_{CC}(t) = 2\rho A_{CC}^{\dagger} S_3 \ddot{s}(t) + 2\rho A_{CC}^{\dagger} S_4 \ddot{U}(t)$$

where

$$S_3 = \begin{bmatrix} \vec{0}_{(N_x+1)(N_y+1)} \\ \vec{1}_{N_y+1} \\ \vec{0}_{N_y+1} \\ \vec{0}_{N_x+1} \\ \vec{0}_{N_X+1} \end{bmatrix} \qquad S_4 = \begin{bmatrix} 0_{(N_x+1)(N_y+1)\times N_x 1+1} \\ 0_{N_y+1\times N_x+1} \\ 0_{N_y+1\times N_x+1} \\ I_{N_x+1} \\ 0_{N_x+1\times N_x+1} \end{bmatrix}$$

Finally, the pressure at the lower boundary ($y = 0$) is given by (3.7)

$$P_0(t) = 2\rho S_1 A_{CC}^{\dagger} \left(S_3 \ddot{s}(t) + S_4 \ddot{U}(t) \right) \tag{3.7}$$

Finally, the operators $\mathcal{M}_s$ and $\mathcal{M}_f$ are realized by the matrices $M_s \in \mathbb{R}^{N_x+1}$ and $M_f \in \mathbb{R}^{(N_x+1)\times(N_x+1)}$, respectively, as follows:

$$\begin{aligned} M_s &= -2\rho S_1 A_{CC}^{\dagger} S_3 \\ M_f &= -2\rho S_1 A_{CC}^{\dagger} S_4 \end{aligned} \tag{3.8}$$

3.3 Spectral Method: Basis Expansion

The macro-mechanical stage can be seen as a static linear system with two inputs: the stapes and basilar membrane vibrations. By the superposition principle of linear systems, we will study each input by itself and then add them up. So, first, lets consider the basilar membrane vibration and set the stapes vibration to be zero. In other words,

lets solve the boundary value problem given by (3.9).

$$\begin{aligned}(\frac{\partial^2}{\partial x^2}+\frac{\partial^2}{\partial y^2})p(x,y,t)&=0\\ \frac{\partial}{\partial x}p(0,y,t)&=0\\ p(L,y,t)&=0\\ \frac{\partial}{\partial y}p(x,0,t)&=2\rho\frac{\partial^2}{\partial t^2}u(x,t)\\ \frac{\partial}{\partial y}p(x,H,t)&=0\end{aligned} \tag{3.9}$$

Define the operator ∇_x as

$$\begin{aligned}\nabla_x : D(\nabla_x) &\to L^2[0,L]\\ f(.) &\mapsto \nabla_x f(.)=\frac{\partial^2}{\partial x^2}f(.)\end{aligned}$$

where

$$D(\nabla_x)=\left\{f\in\mathbb{L}^2([0,L]),\frac{\partial^2}{\partial x^2}f\in\mathbb{L}^2([0,L]),\frac{\partial}{\partial x}f(0)=f(L)=0\right\}$$

and $\mathbb{L}^2([0,L])$ is the space of square integrable functions. It can be shown that this operator is self adjoint with discrete infinitely countable eigenvalues λ_n and orthogonal eigenfunctions ϕ_n given by (3.10).

$$\lambda_n=-(n+\frac{1}{2})^2\frac{\pi^2}{L^2}\longleftrightarrow\phi_n(x)=\sqrt{\frac{2}{L}}cos\left[(n+\frac{1}{2})\frac{\pi}{L}x\right]\quad n=0,1,2,... \tag{3.10}$$

Then the pressure can be expanded in the basis formed of the eigenfunctions $\phi_n(x)$ for $n=0,1,2,...$ as follows:

$$p(x,y,t)=\sum_{n=0}^{\infty}\alpha_n(y,t)\phi_n(x) \tag{3.11}$$

where $\alpha_n(y,t)$ for $n=0,1,2,...$ are the coefficients of $p(x,y,t)$ in the $\phi_n(x)$ basis.

$$\alpha_n(y,t)=\langle p(.,y,t),\phi_n\rangle=\int_0^L p(\chi,y,t)\phi_n(\chi)d\chi$$

Substituting, (3.11) in (3.9) and projecting onto the basis functions, we get a family of differential equations given by (3.12)

$$\begin{aligned}
&\frac{\partial^2}{\partial y^2}\alpha_n(y,t) + \lambda_n\alpha_n(y,t) = 0 \\
&\qquad \frac{\partial}{\partial y}\alpha_n(0,t) = \left\langle 2\rho\frac{\partial^2}{\partial t^2}u(.,t), \phi_n(x)\right\rangle \;\; = \int_0^L 2\rho\frac{\partial^2}{\partial t^2}u(\chi,t), \phi_n(\chi)d\chi \\
&\qquad \frac{\partial}{\partial y}\alpha_n(H,t) = 0 \\
&\quad (n = 0, 1, 2, ...)
\end{aligned} \tag{3.12}$$

Note that time can be treated as a dummy parameter in the differential equations. Solving (3.12) for $\alpha_n(y,t)$ and substituting in (3.11), we get:

$$p(x,y,t) = \sum_{n=0}^{\infty} \frac{e^{(n+\frac{1}{2})\frac{\pi}{L}(y-2H)} + e^{-(n+\frac{1}{2})\frac{\pi}{L}y}}{(n+\frac{1}{2})\frac{\pi}{L}(e^{-2H(n+\frac{1}{2})\frac{\pi}{L}} - 1)}\phi_n(x)\int_0^L 2\rho\frac{\partial^2}{\partial t^2}u(\chi,t)\phi_n(\chi)d\chi$$

Hence, the pressure at the lower boundary ($y = 0$) is given by

$$\begin{aligned}
p(x,0,t) &= \sum_{n=0}^{\infty} \frac{e^{-(n+\frac{1}{2})\frac{\pi}{L}(2H)} + 1}{(n+\frac{1}{2})\frac{\pi}{L}(e^{-2H(n+\frac{1}{2})\frac{\pi}{L}} - 1)}\phi_n(x)\int_0^L 2\rho\frac{\partial^2}{\partial t^2}u(\chi,t)\phi_n(\chi)d\chi \\
&= \sum_{n=0}^{\infty} -\frac{\coth\left[(n+\frac{1}{2})\frac{\pi H}{L}\right]}{(n+\frac{1}{2})\frac{\pi}{L}}\phi_n(x)\int_0^L 2\rho\frac{\partial^2}{\partial t^2}u(\chi,t)\phi_n(\chi)d\chi
\end{aligned}$$

Therefore,

$$p(x,0,t) = -\frac{4\rho}{\pi}\sum_{n=0}^{\infty}\frac{\coth\left[(n+\frac{1}{2})\frac{\pi H}{L}\right]}{n+\frac{1}{2}}cos\left[(n+\frac{1}{2})\frac{\pi}{L}x\right]\int_0^L \frac{\partial^2}{\partial t^2}u(\chi,t)cos\left[(n+\frac{1}{2})\frac{\pi}{L}\chi\right]d\chi \tag{3.13}$$

On the other hand, lets consider the stapes vibration and set the basilar membrane vibration to zero. In other words, lets solve the boundary value problem given by (3.14).

$$\begin{aligned}
(\frac{\partial^2}{\partial x^2} + \frac{\partial^2}{\partial y^2})p(x,y,t) &= 0 \\
\frac{\partial}{\partial x}p(0,y,t) &= 2\rho\frac{d^2}{dt^2}s(t) \\
p(L,y,t) &= 0 \\
\frac{\partial}{\partial y}p(x,0,t) &= 0 \\
\frac{\partial}{\partial y}p(x,H,t) &= 0
\end{aligned} \tag{3.14}$$

It is easy to show that the solution to (3.14) is given by (3.15)

$$p(x,y,t) = 2\rho \frac{d^2}{dt^2} s(t)\,[x-L] \tag{3.15}$$

Therefore, by the superposition principle, the complete analytic expression of the pressure at the lower boundary ($y=0$) is given by (3.16)

$$\begin{aligned} p(x,0,t) = & -2\rho \frac{d^2}{dt^2} s(t)\,[L-x] \\ & - \frac{4\rho}{\pi} \sum_{n=0}^{\infty} \frac{\coth\left[(n+\frac{1}{2})\frac{\pi H}{L}\right]}{n+\frac{1}{2}} \cos\left[(n+\frac{1}{2})\frac{\pi}{L}x\right] \int_0^L \frac{\partial^2}{\partial t^2} u(\chi,t) \cos\left[(n+\frac{1}{2})\frac{\pi}{L}\chi\right] d\chi \end{aligned} \tag{3.16}$$

There are several ways of calculating the integral in (3.16). We will investigate two methods: trapezoidal and Fredholm operations (using Clenshaw-Curtis quadrature rules).

3.3.1 Trapezoidal Integration

We discretize the x-axis in a similar manner to that performed in Figure 3.1, that is $x_i = i\Delta_x$ where $\Delta_x = \frac{L}{N_x}$ for $i = 0, 1, ..., N_x - 1, N_x$. Then, we use the trapezoidal rule to calculate the integral to get the pressure at the lower boundary ($y=0$).

$$P_0(t) = -2\rho(L\vec{1} - \vec{x})\ddot{s}(t) - \frac{4\rho\Delta_x}{\pi} A_T \ddot{U}(t) \tag{3.17}$$

where

$$W = \begin{bmatrix} \frac{1}{2} & 0 & 0 & \cdots & 0 \\ 0 & 1 & 0 & & \vdots \\ \vdots & \ddots & \ddots & \ddots & \vdots \\ \vdots & & \ddots & 1 & 0 \\ 0 & \cdots & \cdots & 0 & \frac{1}{2} \end{bmatrix} \qquad \vec{x} = \begin{bmatrix} x_0 \\ x_1 \\ \vdots \\ x_{N_x-1} \\ x_{N_x} \end{bmatrix} \qquad \vec{1} = \begin{bmatrix} 1 \\ 1 \\ \vdots \\ 1 \\ 1 \end{bmatrix}$$

$$A_T = \sum_{n=0}^{p} \frac{\coth\left[(n+\frac{1}{2})\frac{\pi H}{L}\right]}{n+\frac{1}{2}} \cos\left[(n+\frac{1}{2})\frac{\pi}{L}\vec{x}\right] \cos\left[(n+\frac{1}{2})\frac{\pi}{L}\vec{x}^T\right] W$$

Finally, the operators $\mathcal{M}_s$ and $\mathcal{M}_f$ are realized by the matrices $M_s \in \mathbb{R}^{N_x+1}$ and $M_f \in \mathbb{R}^{(N_x+1)\times(N_x+1)}$, respectively, as follows:

$$\begin{aligned} M_s &= 2\rho(L\vec{1} - \vec{x}) \\ M_f &= \frac{4\rho\Delta_x}{\pi} A_T \end{aligned} \tag{3.18}$$

3.3.2 Fredholm Operator, Clenshaw-Curtis Quadrature

Define the linear operator Λ_n for $n = 0, 1, 2, ...$ as

$$\begin{aligned} \Lambda_n : \mathbb{L}^2([0, L]) &\longrightarrow \mathbb{L}^2([0, L]) \\ f(.) &\longrightarrow \Lambda_n f(.) \end{aligned}$$

where

$$\begin{aligned} (\Lambda_n f)(x) &= \int_0^L K_n(x, \chi) f(\chi) d\chi \\ K_n(x, \chi) &= \cos\left[(n + \frac{1}{2})\frac{\pi}{L}x\right] \cos\left[(n + \frac{1}{2})\frac{\pi}{L}\chi\right] \end{aligned} \tag{3.19}$$

Hence, Λ_n for $n = 0, 1, 2, ...$ are a family of Fredholm operators with $K_n(x, \chi)$ as their corresponding Kernel. Then, (3.16) can be written as :

$$p(x, 0, t) = -2\rho \frac{d^2}{dt^2} s(t) [L - x] - \frac{4\rho}{\pi} \frac{\partial^2}{\partial t^2} \sum_{n=0}^{\infty} \frac{\coth\left[(n + \frac{1}{2})\frac{\pi H}{L}\right]}{n + \frac{1}{2}} [\Lambda_n u(t)](x)$$

Discretize the x dimension using a Chebyshev Collocation grid similar to [24] and obtain a matrix realization F_n for the Fredholm operators Λ_n for $n = 1, 2, ..., p$ using Clenshaw-Curtis quadratures. Thus the pressure at the lower boundary ($y = 0$) can be written as:

$$P_0(t) = -2\rho(L\vec{1} - \vec{x})\ddot{s}(t) - \frac{4\rho}{\pi} A_F \ddot{U}(t) \tag{3.20}$$

where

$$A_F = \sum_{n=0}^{p} \frac{\coth\left[(n + \frac{1}{2})\frac{\pi H}{L}\right]}{n + \frac{1}{2}} F_n$$

Finally, the operators $\mathcal{M}_s$ and $\mathcal{M}_f$ are realized by the matrices $M_s \in \mathbb{R}^{N_x+1}$ and $M_f \in \mathbb{R}^{(N_x+1)\times(N_x+1)}$, respectively, as follows:

$$\begin{aligned} M_s &= 2\rho(\vec{x} - L\vec{1}) \\ M_f &= \frac{4\rho}{\pi} A_F \end{aligned} \tag{3.21}$$

3.4 Numerical Experiments on the Fluid Boundary Value Problem

In this section, we will test the accuracy of the different finite realization schemes of the fluid mass operator $\mathcal{M}_f$. To do so, we calculate the action of the matrix M_f, the finite realization of $\mathcal{M}_f$, on three test inputs with different spatial variations: $f(x) = e^{-x}cos(x)$, $e^{-x}cos(30x)$ and $e^{-x}cos(60x)$. Since the action of $\mathcal{M}_f$ on such inputs is not analytically

tractable, we assume that the finite realization with a very fine $(N_x^e+1)\times(N_y^e+1)-$grid is exact. This realization is denoted by M_f^e defined on the grid points: $\{(x_i^e, y_j^e)\}$. In this section, we use a finite difference method with $N_x^e = 2000, N_y^e = 100$ to realize M_f^e. In order to get an idea of the finite realization error for each method, we first evaluate f at the fine grid points $\{x_i^e\}$ to form an $N_x^e + 1$ vector denoted by f^e. Then, for each finite realization method, we proceed as follows:

1. Compute the finite realization $M_f \in \mathbb{R}^{(N_x+1)\times(N_x+1)}$ of $\mathcal{M}_f$ defined on the grid points $\{x_i\}$, for $i = 1, 2, ..., N_x - 1, N_x$.
2. Evaluate f at the grid points $\{x_i\}$ to form an $N_x + 1$ vector denoted by f^a.
3. Compute $g^e = M_f^e f^e$.
4. Using Chebyshev interpolation, evaluate g^e at $\{x_i\}$ to form an N_x+1 vector denoted by g^{interp}.
5. Compute the error in the $\mathcal{L}_2$ norm sense: $||M_f f^a - g^{interp}||_{\mathcal{L}_2}$.

Figure 3.2 summarizes the results. The test inputs are shown in the first row of the Figure . The second row shows that Chebyshev collocation method clearly outperforms the finite difference method. The third row shows that the choices of the grid size N_x and the number of basis functions p are related. For a given N_x, p should not exceed a certain value. This can be explained by over-fitting: as we include more basis functions by increasing p, a finer grid is required to capture the faster spatial variations of those basis functions. Hence, good values of p lie in a range with a lower limit set by the number of important basis functions that shouldn't be truncated, and an upper limit that is set by the capability of the grid resolution to capture the spatial variations of the faster basis functions. This range becomes narrower as the spatial variation of the input is faster. This can be explained by the need for more basis functions to capture the more rapidly varying input on one hand, and the limitation of the grid resolution on the other hand. These trends are also exhibited by the Clenshaw-Curtis quadrature rule for integration as illustrated in the fourth row. However, the critical value of p, at which the accuracy suddenly degrades is around half of that corresponding to the trapezoidal integration method. Hence, although the Cleshaw-Curtis quadrature rule achieves considerably higher accuracy, it is more susceptible to over-fitting and thus p must be chosen carefully. Since the basilar membrane my exhibit rapid spatial variations, we further test the finite realizations of $\mathcal{M}_f$ on even spatially faster test inputs: $f(x) = e^{-x}cos(90x)$, $e^{-x}cos(140x)$ and $e^{-x}cos(180x)$. Figure 3.3 illustrates the results in a similar fashion to Figure 3.2. We notice that the Chebyshev collocation and Clenshaw-Curtis integration methods degrade with faster spatially varying inputs. This indicates that the Chebyshev grid performs weakly for rapid spatial variations which is typical in the cochlear response. For rapid spatial variations, the finite difference method and the basis expansion with trapezoidal integration have comparable performances. The latter has a

better performance with the cost of choosing the right number of basis functions p. The right choice of p gives a better performance than the finite difference method.

3.5 Frequency Response Using Different Numerical Methods

This section further illustrates the effectiveness of the different numerical methods. The complete model of the middle/inner ear is considered in the linear regime where the active gain γ is preset to a constant. Define the Fourier transform of the pressure at the ear drum to be $\hat{p}_e(j\omega)$ and that of the basilar membrane vibration at a location x to be $\hat{u}(x, j\omega)$, where $\omega = 2\pi f$ denotes the angular frequency and f is expressed in Hertz. The transfer function relating the basilar membrane displacement at a given location to the pressure at the ear drum can be shown to be:

$$\frac{\hat{u}(x, j\omega)}{\hat{p}_e(j\omega)} = \mathcal{C}\left(j\omega\mathcal{E} - \mathcal{A}\right)^{-1}\mathcal{B}\frac{-\omega^2}{k_m - m_m\omega^2 + c_m j\omega} \tag{3.22}$$

where m_m, c_m and k_m are the mass, damping and stiffness of the middle ear given in table 2. The operators $\mathcal{A}, \mathcal{B}$ and $\mathcal{E}$ are given in 2.11 such that $\mathcal{A}$ is equal to $\mathcal{A}_u$ with a fixed unit active gain, say $\gamma(u) = 0.8$. Furthermore, $\mathcal{C}$ is an operator that selects the basilar membrane displacement from the state space variable given in (2.10).

$$\mathcal{C} := \begin{bmatrix}\mathcal{I} & 0 & 0 & 0\end{bmatrix} \tag{3.23}$$

To compare the accuracy of the different numerical methods, we assume that the finite difference realization with a very fine $2001 \times 101-$grid gives the exact frequency response shown in Figure 3.4. We test the different numerical methods by computing the error from the exact frequency response for two grid sizes $N_x = 150$ and 80. Since the frequency response is a complex quantity, the absolute value of the real and imaginary parts of the error are plotted at each location for every frequency. Figure 3.5 shows the error plots for all four methods. Clearly, the basis expansion method with trapezoidal integration has the lowest error. Moreover, as one would expect, the finite difference method has the worst performance. However, for a coarser grid ($N_x = 80$), the finite difference method shows better performance than the Chebyshev collocation and Clenshaw-Curtis integration methods as illustrated in Figure 3.6. Still, with the right choice of the number of basis functions p, the trapezoidal integration method is outperforming the other methods.

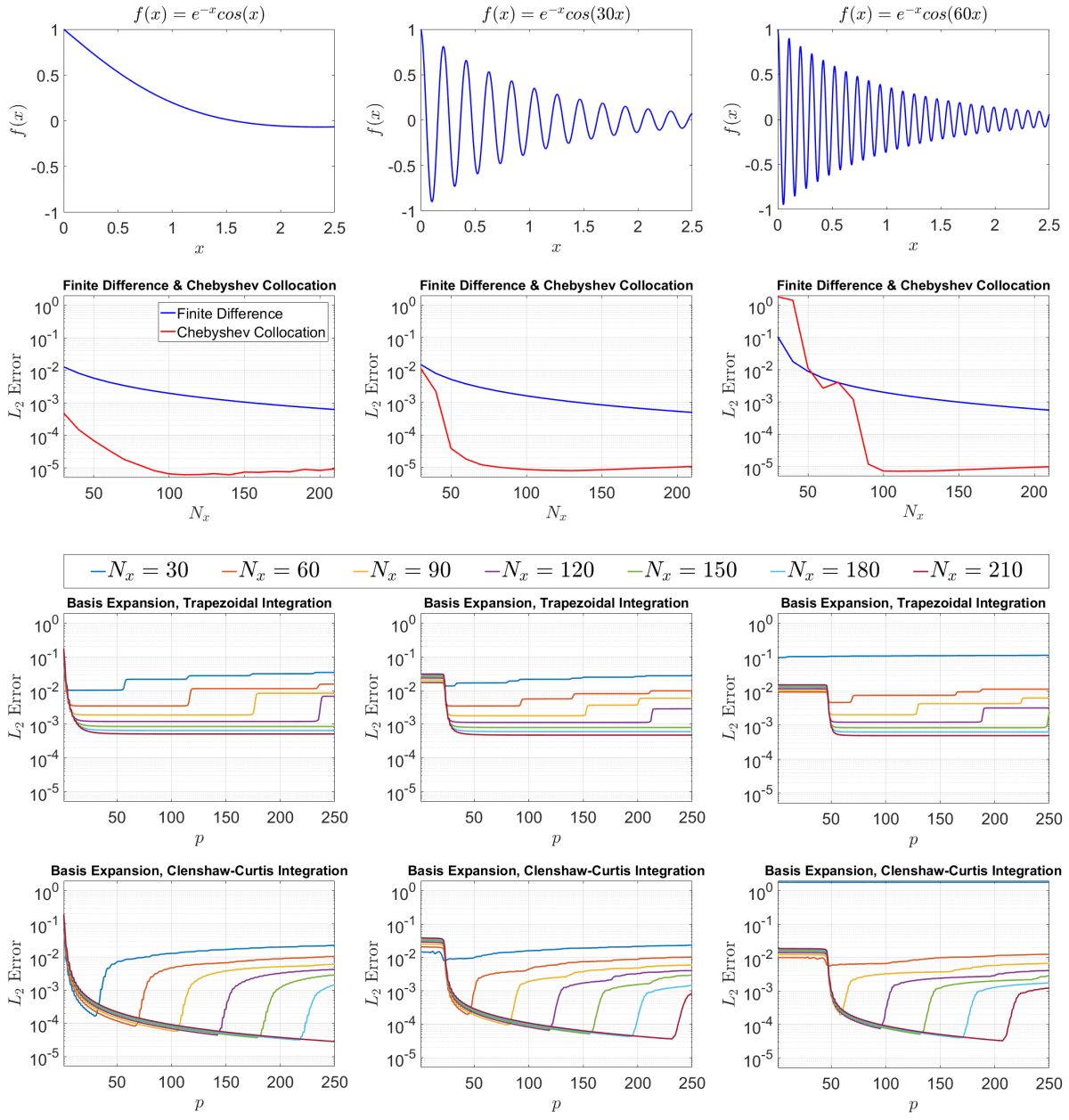

Figure 3.2: Finite realization error of the fluid mass operator $\mathcal{M}_f$. The error is computed through the action of $\mathcal{M}_f$ on three different inputs shown in the first row. The second row shows the behavior of the error, for each input, as N_x is varied using the finite difference and Chebyshev collocation methods. The third and fourth rows depict the effect of the grid size N_x and the number of basis functions p on the finite realization error while using the trapezoidal and Clenshaw-Curtis quadratures for integration, respectively.

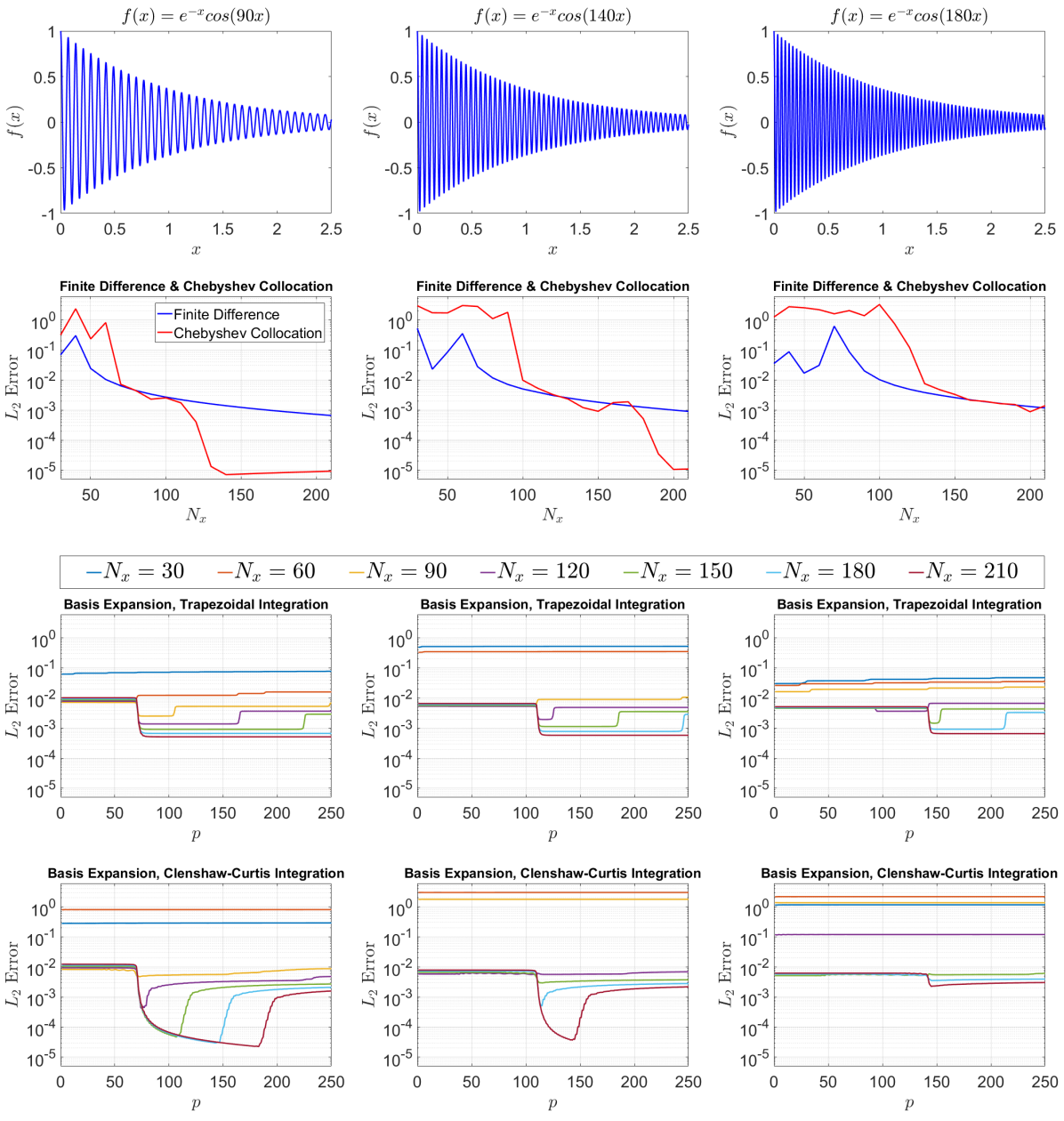

Figure 3.3: Finite realization error of the fluid mass operator $\mathcal{M}_f$ similar to Figure 3.2 but for three different test inputs with higher spatial variations.

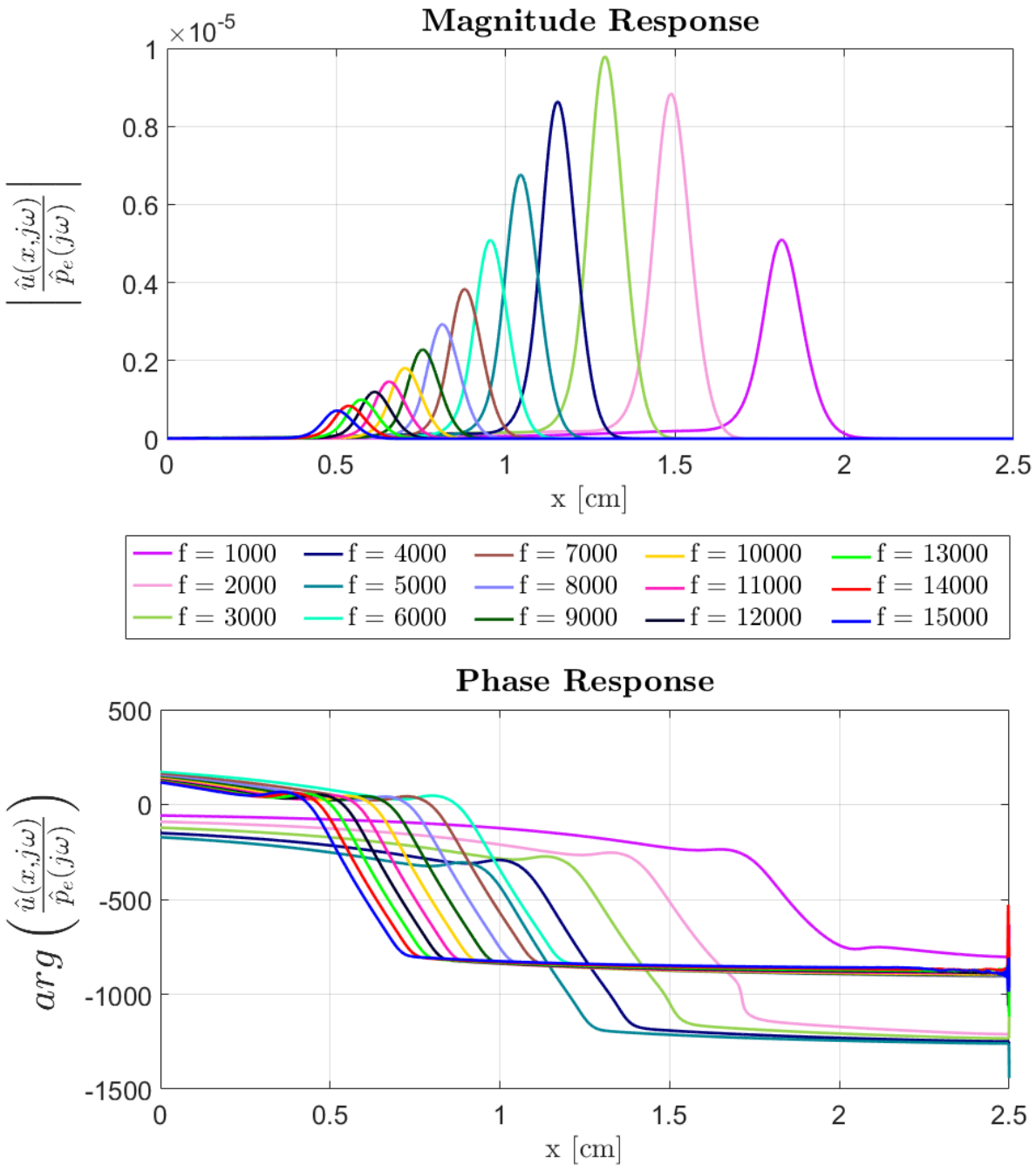

Figure 3.4: Frequency Response relating the basilar membrane displacement u at a location x to the pressure at the eardrum p_e.

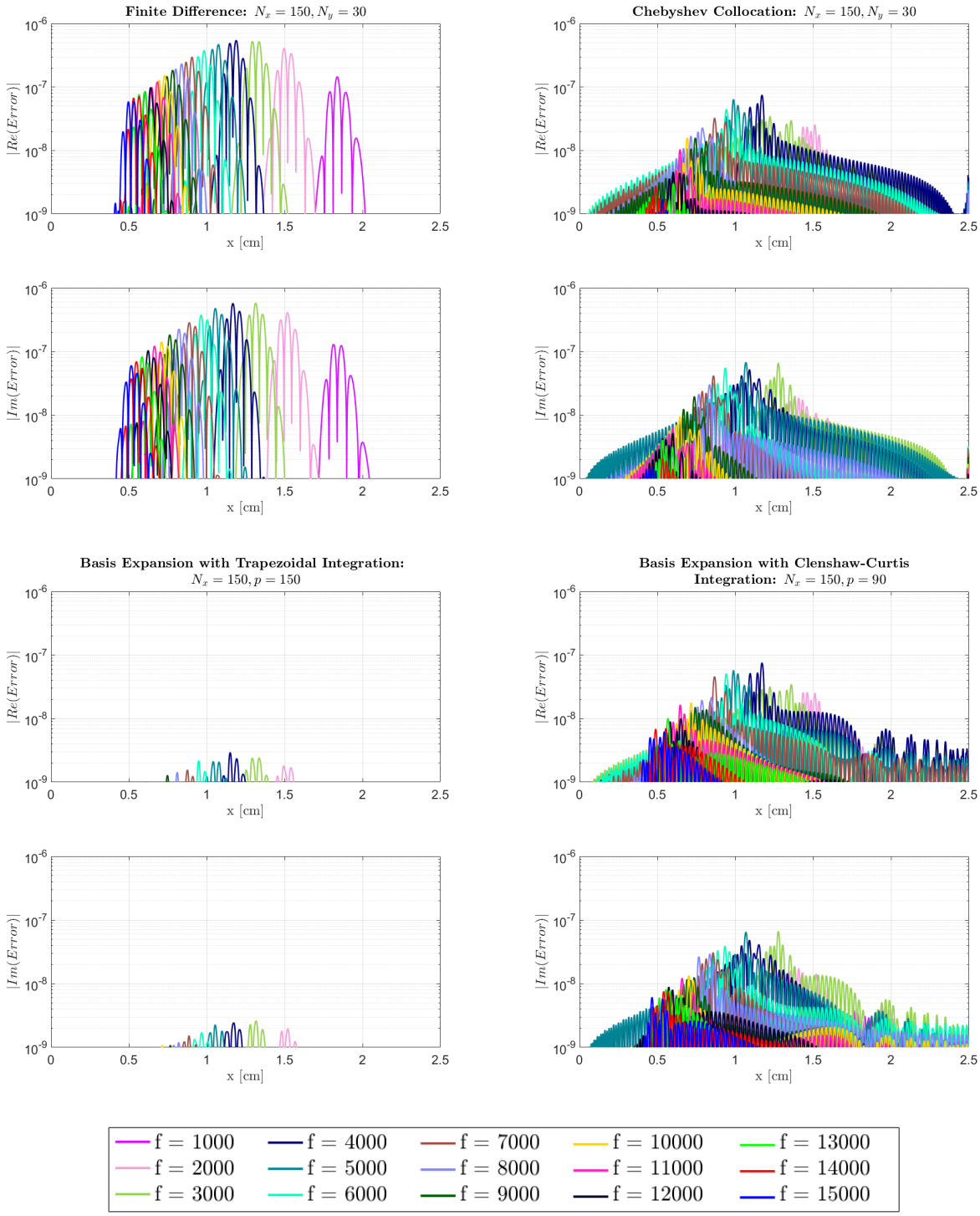

Figure 3.5: Frequency response error of the different numerical methods. The error is calculated as the deviation of the transfer function given in 3.22, as realized by each numerical method with 150 grid points, from the exact transfer function. The exact transfer function is approximated by a finite difference method with a very fine grid.

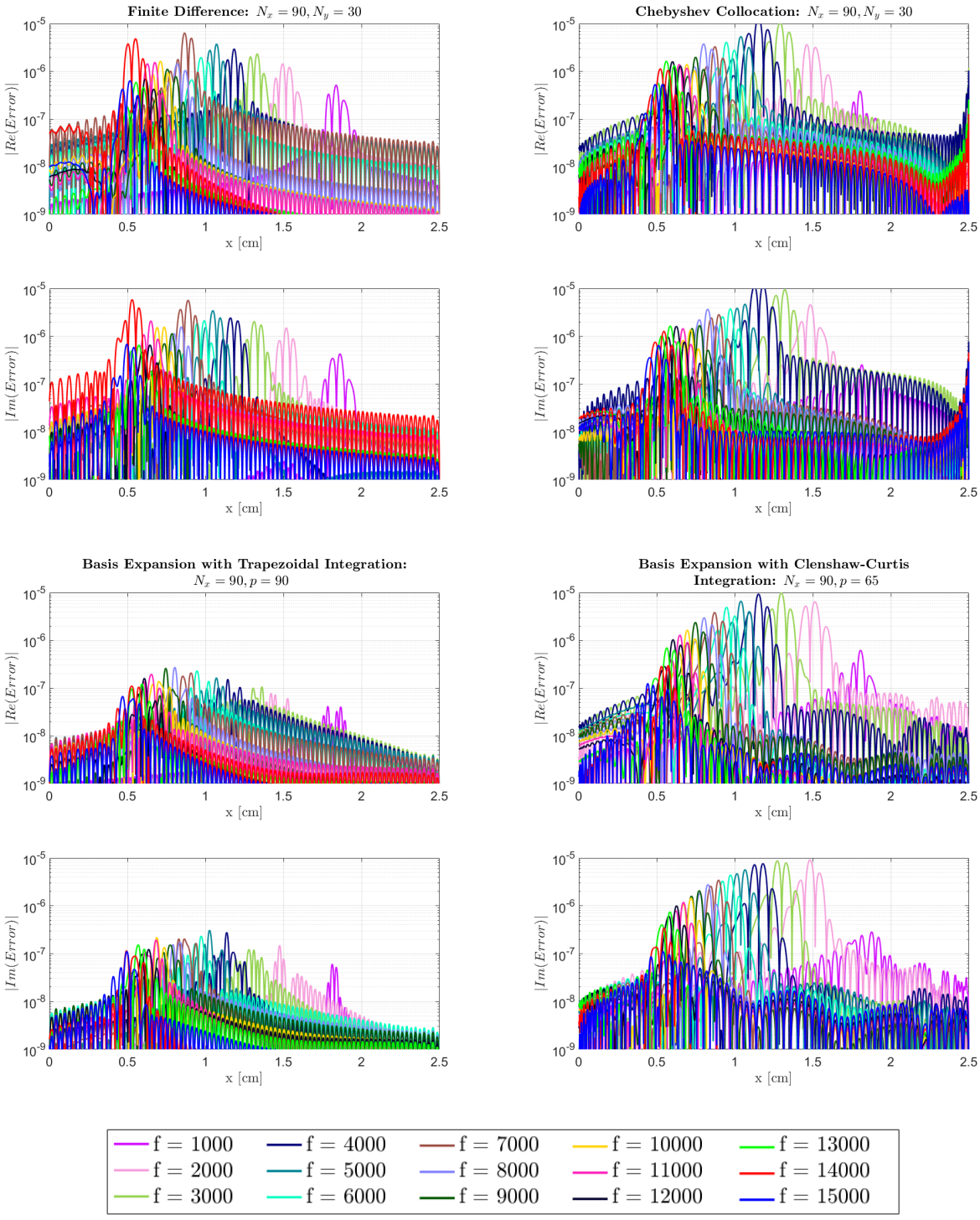

Figure 3.6: Frequency response error of the different numerical methods. The error is calculated as the deviation of the transfer function given in 3.22, as realized by each numerical method with 90 grid points, from the exact transfer function. The exact transfer function is approximated by a finite difference method with a very fine grid.

Chapter 4

Possible Sources of Instability in the Cochlea

In this chapter, we analyze the stability of the cochlear model developed in the previous chapters. The cochlea is a highly sensitive device that is capable of sensing sound waves across a broad spectrum of frequencies ($20 - 20000$Hz) and across a wide range of sound intensities ranging from 0dB (threshold of hearing) up to 120dB (sound of a jet engine). The cochlea was believed to be a passive device that acts like a Fourier analyzer: each frequency causes a vibration at a particular location on the basilar membrane (BM). This mechanism was discovered by the Nobel Prize winner George von Békésy who carried out his experiments on cochleae of human cadavers. However, in 1948, Thomas Gold hypothesized that the ear is rather an active device that has a component termed the cochlear amplifier. Although Gold's hypothesis was rejected by von Békésy, David Kemp validated it thirty years later by measuring emissions from the ear. These emissions, termed otoacoustic emissions (OAEs) are sound waves that are produced by the cochlea and can be measured in the ear canal.

It is widely accepted that the outer hair cells, anchored on the cochlear partition, are responsible for the active gain in the cochlea that produces these emissions. However, the underlying mechanism is still not well understood. For example, spontaneous otoacoustic emissions (SOAEs) –emissions generated in the absence of any stimulus – are studied in [25]. The authors showed that random active gain profiles cause instabilities in a linear model of the cochlea. Their analysis was carried out through Monte Carlo simulations by studying the stability for 400 different randomly generated active gain profiles with a spatially-invariant mean. In this chapter, we study two possible sources of instabilities. The first one being the level of the active gain and the second being the rapid spatial variations of the spatial gain. Our analysis is carried out on the linearization of the cochlear model. Furthermore, rather than just looking at the eigenvalues, we study the rate of change of the eigenvalues due to small perturbations in the active gain profile.

4.1 System Linearization

The general linearization around any given state $\bar{\psi}$ will be given in details in chapter 6 for the application of the extended Kalman filter. However, for the rest of the current chapter, we linearize around the origin (fixed point) to study the stability. In fact, the linearization around $\bar{\psi} = 0$ yields the original dynamics (2.11) but with the nonlinear time-varying active gain $\gamma(u)$ replaced by the time-invariant gain $\gamma_0(x)$.

$$\mathcal{E}\frac{\partial}{\partial t}\psi = \mathcal{A}\psi + \mathcal{B}\ddot{s} \tag{4.1}$$

where

$$\mathcal{A} := \begin{bmatrix} 0 & 0 & \mathcal{I} & 0 \\ 0 & 0 & 0 & \mathcal{I} \\ \gamma_0 k_4 - (k_1 + k_3) & k_3 - \gamma_0 k_4 & \gamma_0 c_4 - (c_1 + c_3) & c_3 - \gamma_0 c_4 \\ k_3 & -(k_2 + k_3) & c_3 & -(c_2 + c_3) \end{bmatrix}$$

Equipped with the linearized dynamics (4.1), we carry out two different approaches to analyze the stability. The first approach studies the effect of the gain level $\gamma_0(x)$. This approach assumes a spatially constant gain $\gamma_0(x) = \gamma_0$. Tools such as root locus come in handy for this approach to study the stability versus the value of γ_0. On the other hand, the second approach studies the effect of the spatial variation of $\gamma_0(x)$ on stability.

4.2 Stability Effect of the Gain Level

In this section, we study the stability of the linearized cochlear dynamics (4.1) as we vary a spatially constant gain from 0 (indicating no gain at all) up to 1 (indicating full active gain) as shown in Figure 4.1. For each value of γ_0, we compute the eigenvalues of the operator $\mathcal{E}^{-1}\mathcal{A}$ and plot them in the complex plane as shown in Figure 4.2. The root locus, in Figure 4.2, demonstrates that when $\gamma_0 = 0.89$, a conjugate pair of eigenvalues crosses the imaginary axis towards the right half plane. Thus for $\gamma_0 \geq 0.89$, the linearized dynamics become unstable. In fact, the root locus shows that the unstable pair of eigenvalues are very sensitive to the variations of γ_0: they move much faster, as we vary γ_0, than all the other eigenvalues close to the imaginary axis. The frequency of the unstable eigenvalues is around $250Hz$. The magnitude and phase of the unstable eigenfunction corresponding to the unstable eigenvalue are plotted in Figure 4.3 demonstrating an instability at an apical location corresponding to $250Hz$.

4.3 Stability Effect of Rapid Spatial Perturbations

In this section, we impose a rapid spatial perturbation on the gain profile $\gamma_0(x)$. First, we analyze the effect of an infinitesimal perturbation of the gain profile on the rate of

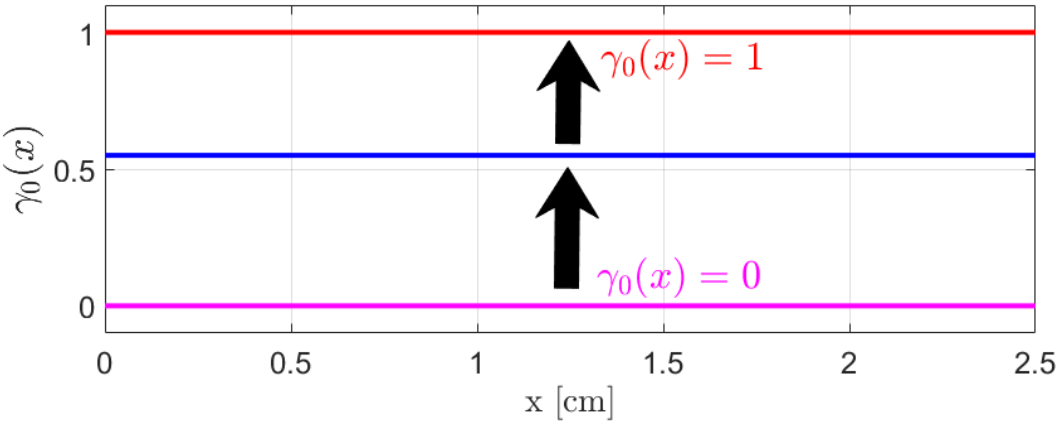

Figure 4.1: Sweeping the level of the active gain from 0 to 1 but remaining spatially constant.

change of the eigenvalues. Then, we investigate the effect of different perturbations at different locations with various gain levels.

4.3.1 Rate of variation of the perturbed eigenvalues

We study the stability effect of a small but rapid spatial perturbation at some location, say $x = 1.25cm$, as illustrated in Figure 4.4. The location on the basilar membrane at $x = 1.25cm$ has a characteristic frequency of $3.6kHz$ as shown in Figure 4.5. That is, for a stimulus at a frequency of $3.6kHz$, the maximal vibration at the basilar membrane occurs at the location $x = 1.25cm$.
We are interested in the rate of change of the eigenvalues of $\mathcal{A}$ with respect to the perturbation ϵ. For this reason, we give an eigenvalue perturbation analysis of the operator $\bar{\mathcal{A}} := \mathcal{E}^{-1}\mathcal{A}$. The gain given in Figure 4.4 can be written as:

$$\gamma_0(x) = 1 - \epsilon\gamma_1(x)$$

where $\gamma_1(x)$ is a step function:

$$\gamma_1(x) = \begin{cases} 1, & x \leq 1.25 \\ 0, & x > 1.25 \end{cases}$$

This allows us to write the operator $\bar{\mathcal{A}}$ as

$$\bar{\mathcal{A}} = \bar{\mathcal{A}}_0 + \epsilon\bar{\mathcal{A}}_1 \tag{4.2}$$

where $\bar{\mathcal{A}}_0 := \mathcal{E}^{-1}\mathcal{A}_0$ and $\bar{\mathcal{A}}_1 := \mathcal{E}^{-1}\mathcal{A}_1$ such that:

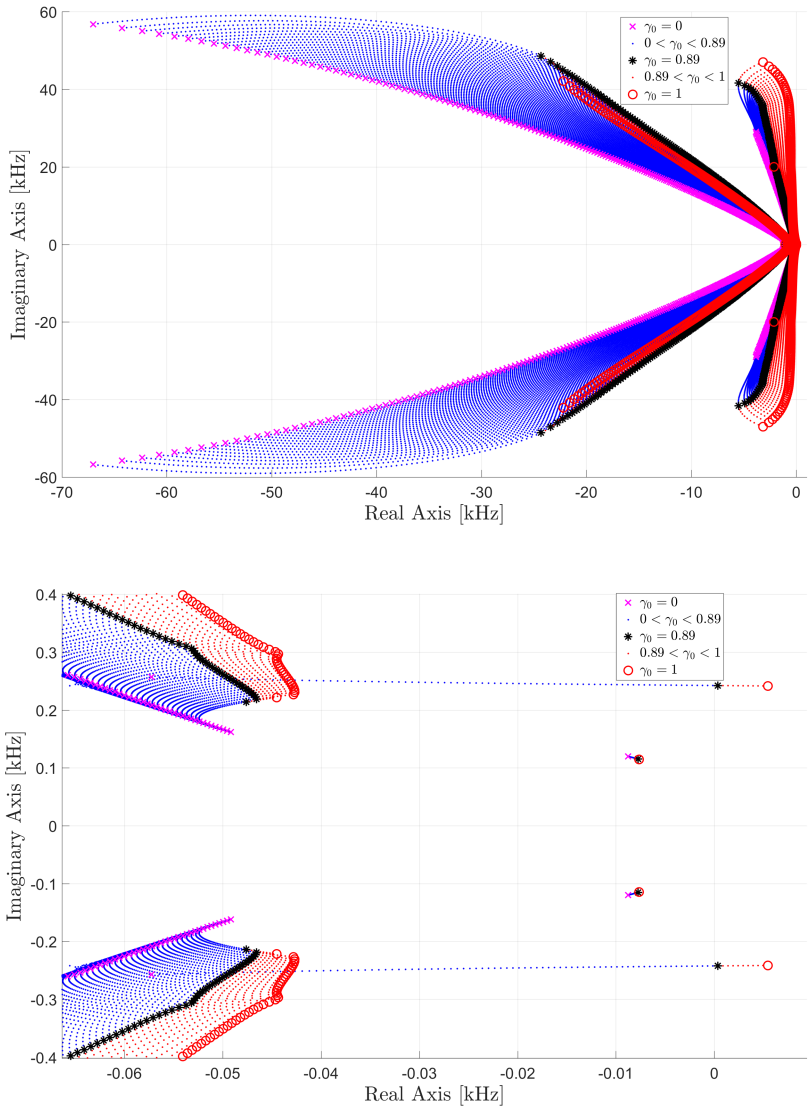

Figure 4.2: Locus of the eigenvalues of the linearized cochlear dynamics as γ_0 varies from 0 (no active gain) up to 1 (full active gain). The Figure on the top shows the eigenvalues for different values of γ_0. The magenta crosses corresponds to $\gamma_0 = 0$, the blue dots corresponds to the range of γ_0 where the system is stable. The black asterisks correspond to $\gamma_0 = 0.89$ where the eigenvalues first cross to the right half plane rendering the system unstable. Finally, the red dot correspond to the range of γ_0 where the system is unstable ending with red circles for $\gamma_0 = 1$.

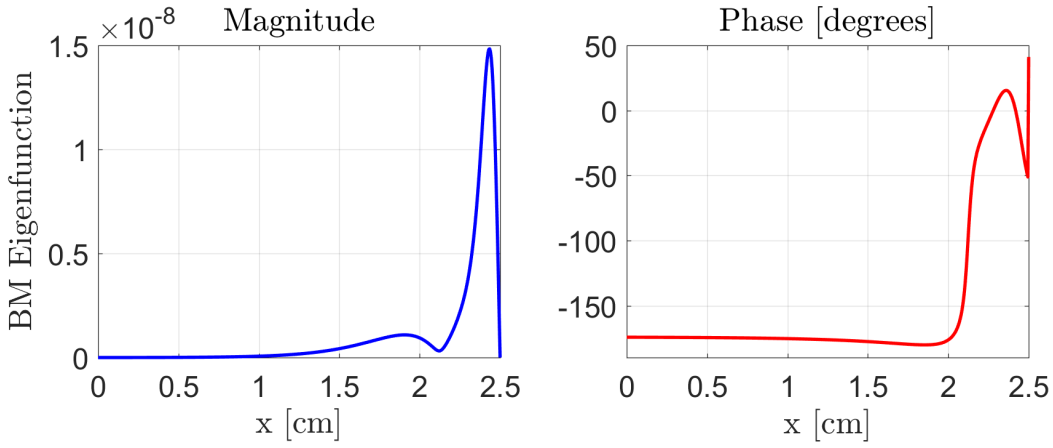

Figure 4.3: Magnitude and phase of the unstable mode of the linearized cochlear dynamics when $\gamma_0(x) = 0.89$.

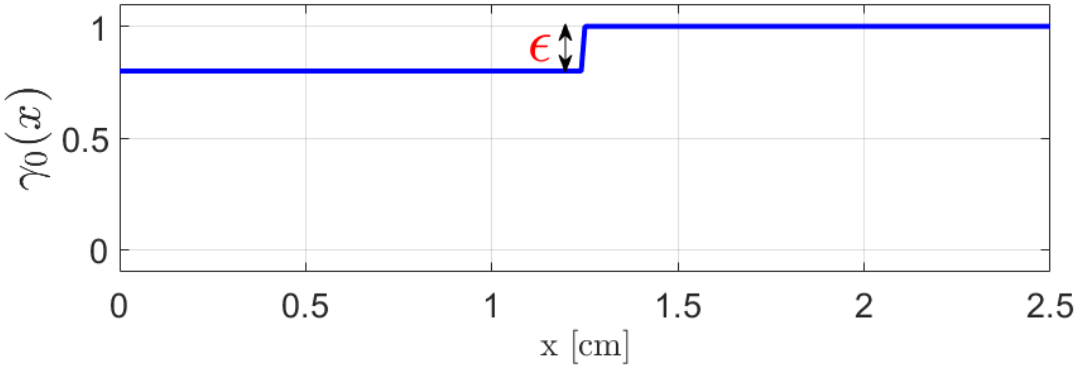

Figure 4.4: Rapid spatial perturbation imposed at $x = 1.25cm$ on the gain profile $\gamma_0(x)$. ϵ denotes an arbitrary small number.

$$\mathcal{A}_0 := \begin{bmatrix} 0 & 0 & \mathcal{I} & 0 \\ 0 & 0 & 0 & \mathcal{I} \\ k_4 - (k_1 + k_3) & k_3 - k_4 & c_4 - (c_1 + c_3) & c_3 - c_4 \\ k_3 & -(k_2 + k_3) & c_3 & -(c_2 + c_3) \end{bmatrix}$$

$$\mathcal{A}_1 := \gamma_1 \begin{bmatrix} 0 & 0 & 0 & 0 \\ 0 & 0 & 0 & 0 \\ -k_4 & k_4 & -c_4 & c_4 \\ 0 & 0 & 0 & 0 \end{bmatrix}$$

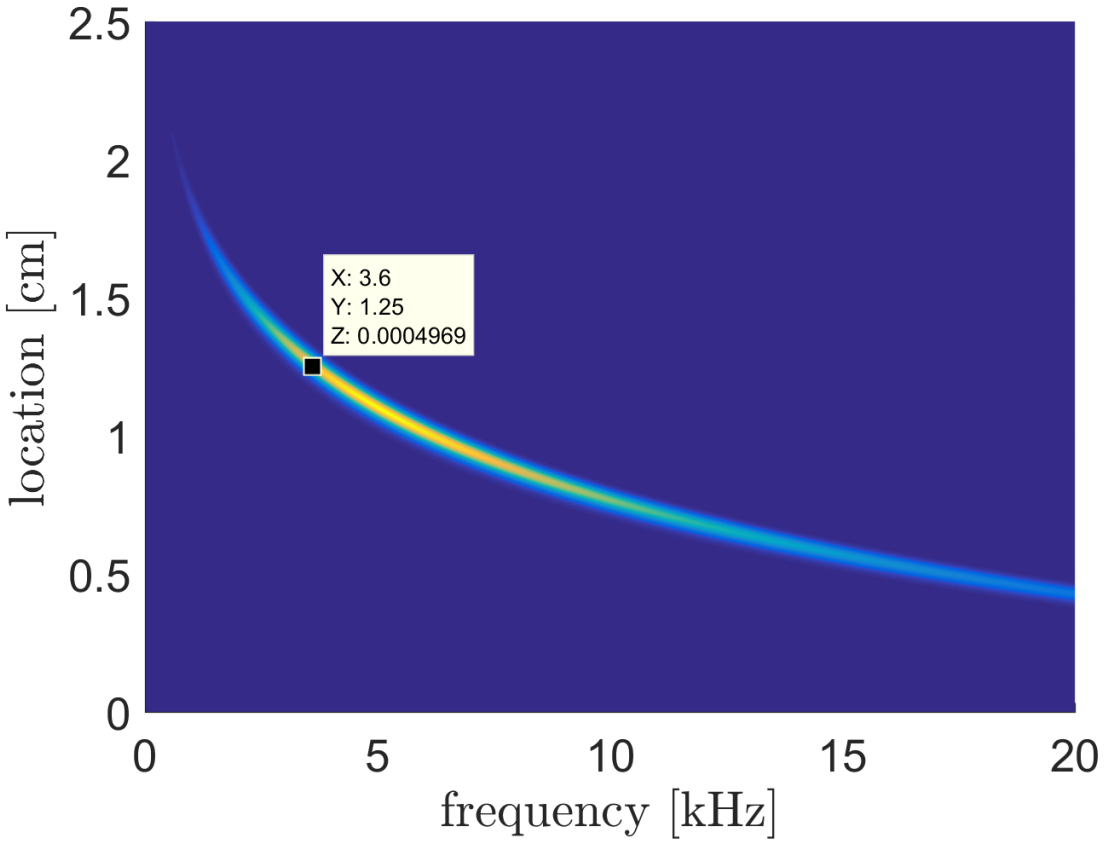

Figure 4.5: Frequency to location mapping. This intensity plot depicts the frequency response of the linearized cochlear dynamics for $\gamma_0(x) = 1$ as shown in equation (3.22) such that $\omega = 2\pi f$ with f denoting the frequency in kHz. The peaks of the intensity plot correspond to the characteristic frequency (CF) of each location. The CF of $x = 1.25cm$ is $3.6kHz$.

Now suppose that λ is an eigenvalue of $\bar{\mathcal{A}}$ with ϕ being the corresponding right eigenfunction. Then,

$$\bar{\mathcal{A}}\ \phi = \lambda\phi$$

Since λ, ϕ and ψ are all functions of ϵ, we expand them in Taylor series around $\epsilon = 0$ up to first order:

$$\lambda = \lambda_0 + \epsilon\lambda_1 + \mathcal{O}(\epsilon^2)$$
$$\phi = \phi_0 + \epsilon\phi_1 + \mathcal{O}(\epsilon^2)$$
$$\psi = \psi_0 + \epsilon\psi_1 + \mathcal{O}(\epsilon^2)$$

Note that $\lambda_1 = \frac{d}{d\epsilon}\lambda(\epsilon = 0)$. By replacing all the expansion in (4.2), we get:

$$\left(\bar{\mathcal{A}}_0 + \epsilon\bar{\mathcal{A}}_1\right)\left(\phi_0 + \epsilon\phi_1\right) = \left(\lambda_0 + \epsilon\lambda_1\right)\left(\phi_0 + \epsilon\phi_1\right) + \mathcal{O}(\epsilon^2)$$

Collecting same orders in ϵ, we arrive at:

$$\begin{aligned}\epsilon^0: &\quad \bar{\mathcal{A}}_0\phi_0 = \lambda_0\phi_0\\ \epsilon^1: &\quad \bar{\mathcal{A}}_1\phi_0 + \bar{\mathcal{A}}_0\phi_1 = \lambda_1\phi_0 + \lambda_0\phi_1\end{aligned}$$

The first equation suggests that λ_0 is an eigenvalue of $\bar{\mathcal{A}}_0$ with ϕ_0 being the corresponding right eigenfunction. Let ψ_0 be the left eigenfunction of $\bar{\mathcal{A}}_0$ corresponding to the eigenvalue λ_0, that is $\bar{\mathcal{A}}_0^*\psi_0 = \lambda_0\psi_0$, where $\bar{\mathcal{A}}_0^*$ is the adjoint of $\bar{\mathcal{A}}_0$. We then project the second equation on ψ_0 and proceed as follows.

$$\begin{aligned}\langle\psi_0, \bar{\mathcal{A}}_1\phi_0 + \bar{\mathcal{A}}_0\phi_1\rangle &= \langle\psi_0, \lambda_1\phi_0 + \lambda_0\phi_1\rangle\\ \langle\psi_0, \bar{\mathcal{A}}_1\phi_0\rangle + \langle\psi_0, \bar{\mathcal{A}}_0\phi_1\rangle &= \lambda_1\langle\psi_0, \phi_0\rangle + \lambda_0\langle\psi_0, \phi_1\rangle\\ \langle\psi_0, \bar{\mathcal{A}}_1\phi_0\rangle + \langle\bar{\mathcal{A}}_0^*\psi_0, \phi_1\rangle &= \lambda_1\langle\psi_0, \phi_0\rangle + \lambda_0\langle\psi_0, \phi_1\rangle\\ \langle\psi_0, \bar{\mathcal{A}}_1\phi_0\rangle + \lambda_0\langle\psi_0, \phi_1\rangle &= \lambda_1\langle\psi_0, \phi_0\rangle + \lambda_0\langle\psi_0, \phi_1\rangle\end{aligned}$$

where $\langle,\rangle$ denotes the inner product. Canceling the same terms on both sides of the equation and solving for λ_1, we finally get:

$$\lambda_1 = \frac{\langle\psi_0, \bar{\mathcal{A}}_1\phi_0\rangle}{\langle\psi_0, \phi_0\rangle}$$

Therefore, the rate of change of λ with respect to ϵ is described by the following equation:

$$\frac{d}{d\epsilon}\lambda(\epsilon = 0) = \frac{\langle\psi_0, \mathcal{E}^{-1}\mathcal{A}_1\phi_0\rangle}{\langle\psi_0, \phi_0\rangle} \tag{4.3}$$

where ϕ_0 and ψ_0 are the left and right eigenfunctions of $\bar{\mathcal{A}}_0 = \mathcal{E}^{-1}\mathcal{A}_0$ corresponding to the eigenvalue λ_0, respectively. Equation (4.3), in fact, represents the initial velocity of the eigenvalues of the linearized dynamics of the cochlea as we begin to spatially perturb the gain function $\gamma_0(x)$ at the location $x = 1.25cm$. Figure 4.6 illustrates the behavior of the eigenvalues of $\bar{\mathcal{A}}$ as ϵ is slightly perturbed from zero. The plot to the left shows the eigenvalues of $\bar{\mathcal{A}}_0$ in the complex plane, in red. The velocities of the eigenvalues, $\frac{d}{d\epsilon}\lambda(\epsilon = 0)$, are also shown as blue vectors. It is clear that the velocities are negligible for all the eigenvalues except those close to the characteristic frequency (CF) of the perturbation location. The Figure to the right zooms in to the relatively large vectors to show that the eigenvalues with frequencies close to the CF of $x = 1.25cm$ move rapidly in different directions. In fact some of them move to the right half plane and render the linearized dynamics unstable. For example, we take $\epsilon = 0.01$ and the eigenvalues are shown in Figure 4.7. Clearly, several eigenvalues with frequencies close to the characteristic frequency of $x = 1.25cm$ lie in the right half plane. The magnitude and phase of the eigenfunctions corresponding to the unstable eigenvalues are depicted in Figure 4.8. Again, the unstable modes have peaks close to the location of the perturbation of the active gain.

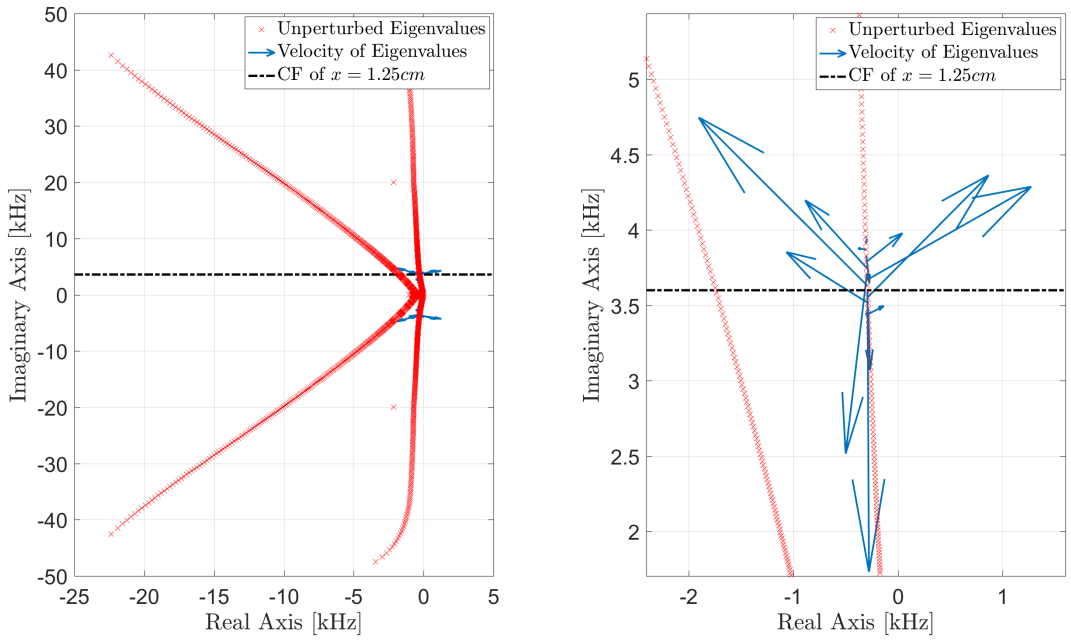

Figure 4.6: Perturbation of the eigenvalues of the linearized cochlear dynamics due to a rapid spatial perturbation of the gain function $\gamma_0(x)$ at location $x = 1.25cm$ whose characteristic frequency (CF) is $3.6kHz$. The plot to the left shows the eigenvalues of the unperturbed dynamics along with the velocities of the eigenvalues as the gain function is perturbed as shown in Figure 4.4. The plot to the right zooms in to the large velocity vectors.

4.3.2 Stability effect of the perturbation location

In this section, we consider the profile for the linearized active gain shown in Figure 4.9 such that:

$$\gamma_0(x) = (\gamma_{max} - \epsilon) + \epsilon h(x - x_p) \tag{4.4}$$

where $h(.)$ is the Heaviside function. We study the effect of the three parameters: the maximal gain γ_{max}, the perturbation ϵ and the location of the perturbation x_p on the stability of the linearized dynamics. For each γ_{max} and x_p, we find the value of ϵ that causes eigenvalues with corresponding frequencies to cross the imaginary axis to the right half plane. Figure 4.10 plots the minimum values of ϵ that causes instabilities for different (x_p, γ_{max}). The results show that it is more likely to have instabilities in a bounded region. As a matter of fact, γ_{max} can be designed to bound the locations of instabilities arising from rapid spatial variations. For example, for $\gamma_{max} = 0.785$, the instabilities are bounded for $0.55 < x_p < 1.25$. Thus, the frequencies are band limited to $[3.5kHz, 14kHz]$.

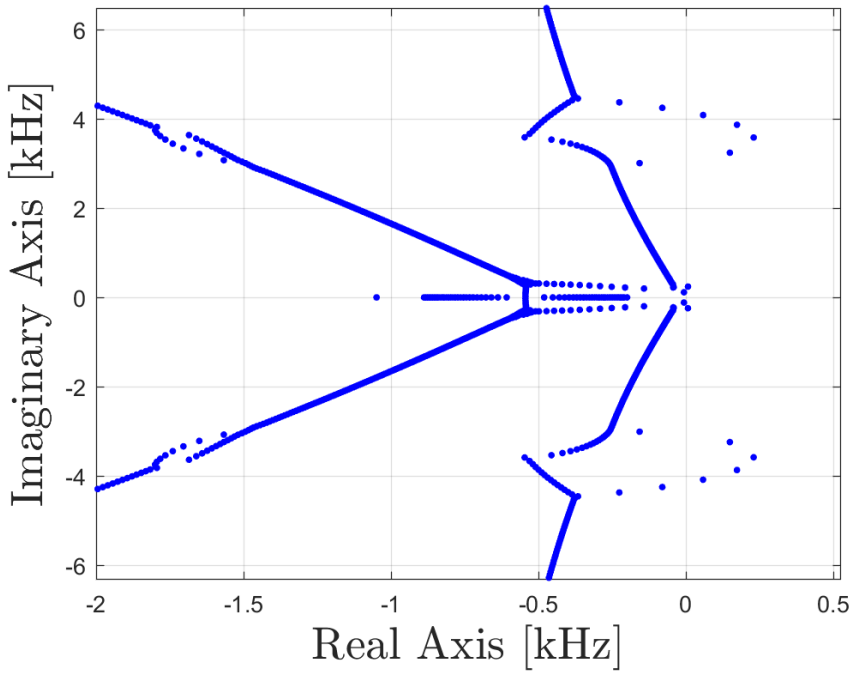

Figure 4.7: Distribution of eigenvalues for the linearized cochlear dynamics with a spatially perturbed active gain as shown in Figure 4.4 where $\epsilon = 0.01$.

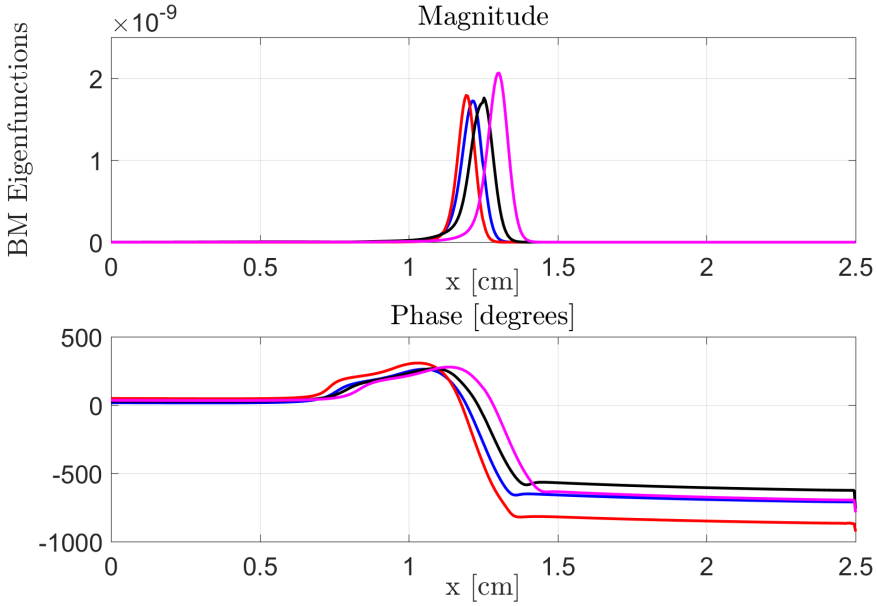

Figure 4.8: Unstable modes of the linearized cochlear dynamics with a spatially perturbed active gain as shown in Figure 4.4 where $\epsilon = 0.01$.

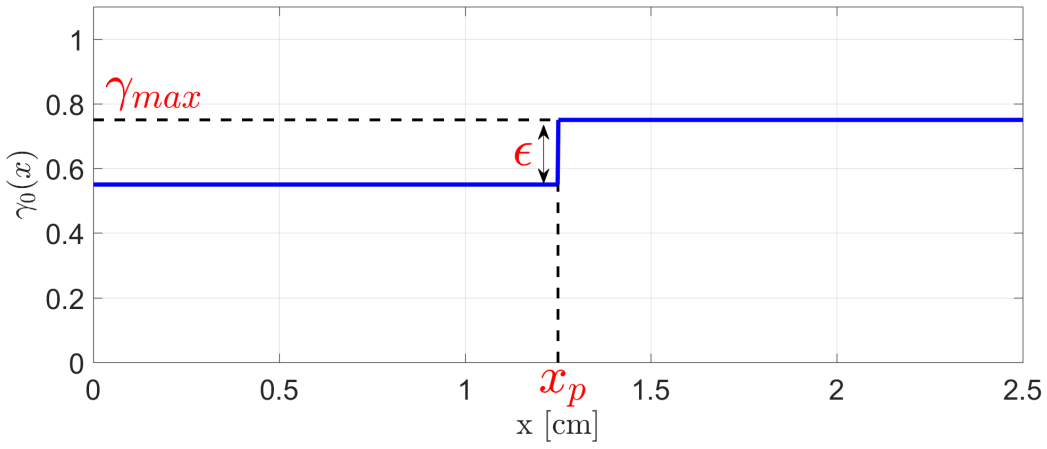

Figure 4.9: Rapid spatial perturbation imposed at $x = x_p cm$ on the gain profile $\gamma_0(x)$. ϵ denotes the intensity of the perturbation and γ_{max} denotes the maximum gain.

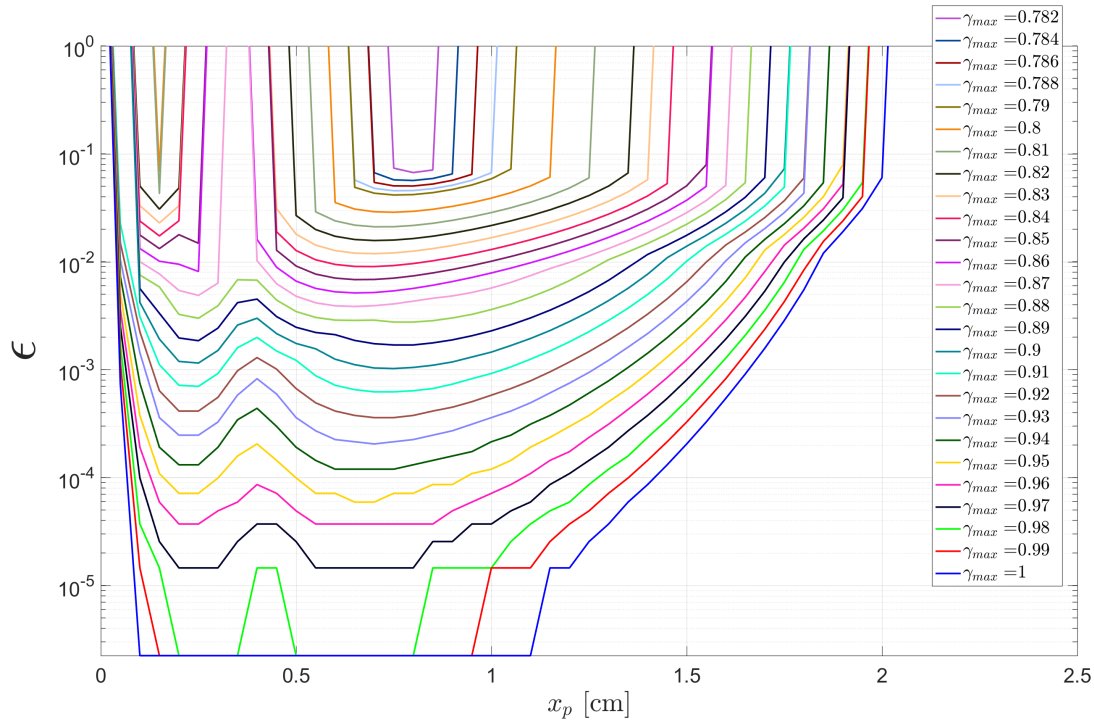

Figure 4.10: Instabilities caused by perturbations at different locations x_p for different values of γ_{max}. The value of ϵ indicates the minimum perturbation that causes instabilities around the corresponding location on the basilar membrane.

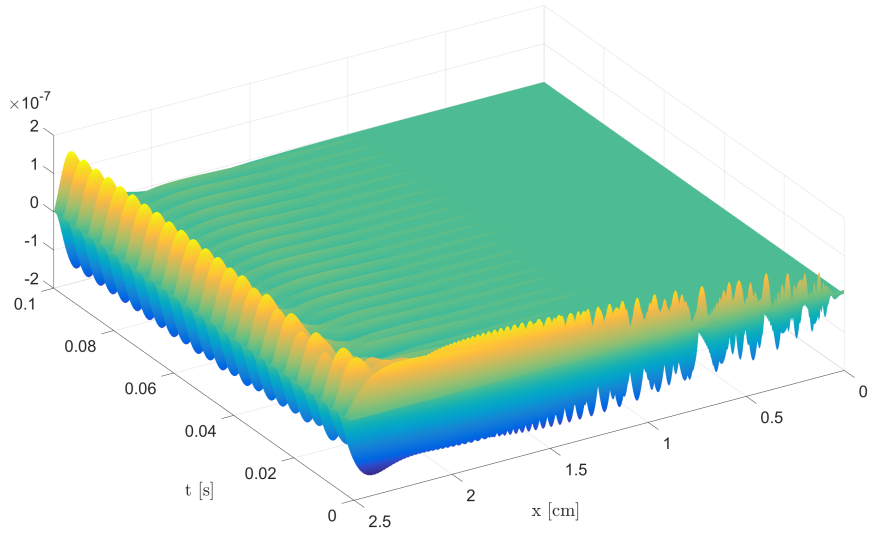

Figure 4.11: Temporal evolution of the basilar membrane profile without any input. The nonlinear model (2.11) was used to generate this plot with $\gamma_0(x) = 1$. A Limit cycle is born at the apical location ($x = 2.41cm$) of the unstable mode peak of the linearized dynamics shown in Figure 4.3.

4.4 Limit Cycles of the Nonlinear Model

The previous two sections propose two different sources of instabilities in the cochlear model. The stability analysis was carried out for the linearized dynamics. We show now the behavior of the nonlinear model in the presence of these instabilities. For the first kind of instability, we use the nonlinear model (2.11) with $\gamma_0(x) = 1$. We show the temporal evolution of the basilar membrane in the 3D plot of Figure 4.11. Clearly, a limit cycle is formed around the location of the unstable mode peak of the linearized dynamics. This limit cycle is caused by the saturating effect of the nonlinear active gain $\gamma(u)$ since for small BM vibrations, $\gamma(u)$ is large; and for large BM vibrations $\gamma(u)$ is small. Moreover, we place a virtual probe on the apical location $x = 2.41cm$ to measure the basilar membrane vibrations $u(x = 2.41, t)$. This is the location that corresponds to the peak of the unstable mode shown in Figure 4.3. The vibration grows until it reach a maximum value as shown in the first plot of Figure 4.12. Let $\hat{u}(x = 2.41, j\omega)$ denote the Fourier transform of the time signal $u(x = 2.41, t)$. The second plot in Figure 4.12 shows the magnitude of $\hat{u}(x = 2.41, j2\pi f)$ which verifies that the prominent frequency is the same as the characteristic frequency corresponding to $x = 2.41cm$.
On the other hand, for the second kind of instability we use again the nonlinear model (2.11) but with a spatially perturbed $\gamma_0(x)$ as shown in Figure 4.9 with $\epsilon = 0.001$, $\gamma_{max} = 1$ and $x_p = 1.25cm$. Figure 4.13 shows the time evolution of the basilar membrane displacement profile. It clearly shows a limit cycle that emerges at the location of the

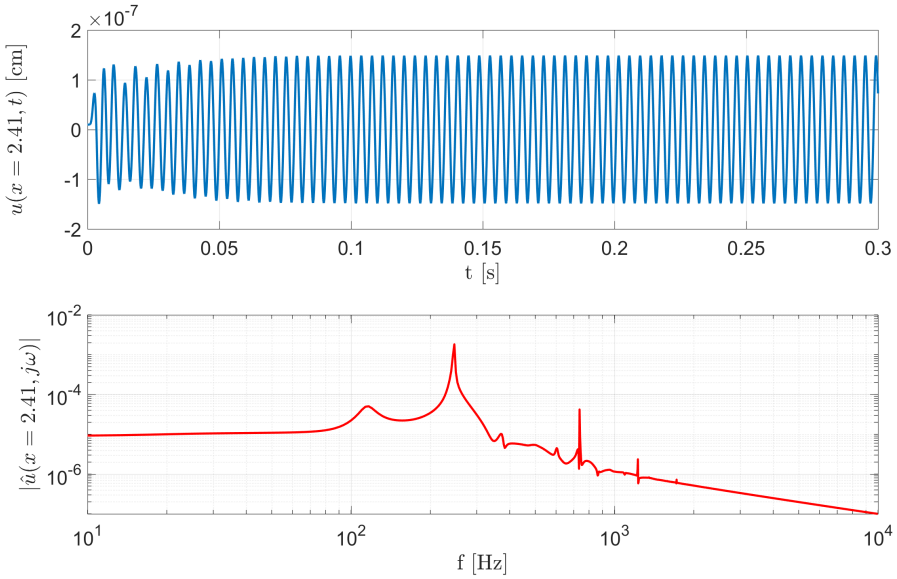

Figure 4.12: Basilar membrane vibration at the location $x = 2.41cm$ with a characteristic frequency of $250Hz$. The Figure at the top shows the temporal evolution. That at the bottom shows the Fourier transform that confirms that the vibration has a frequency equal to the characteristic frequency at that location.

perturbation. To look at the frequency content of the vibrations, we place a virtual probe on the location of the perturbation and compute the Fourier transform as depicted in Figure 4.14. The main frequency of the vibration at the location of the perturbation is the same as the characteristic frequency of the latter. However, additional frequencies, close to the characteristic frequency, are also present. The additional frequencies correspond to the unstable eigenvalues of the linearized dynamics shown in Figure 4.7.
Finally, we look at the effect of the value of ϵ on the nonlinear dynamics. Figure 4.15 shows that as ϵ is increased, the magnitude of the limit cycle slightly increases. Moreover, after some value of ϵ, the frequencies of the limit cycle merge and become a single frequency but shifted or "detuned" to a lower frequency. This larger value of ϵ sort of "masks" the other frequencies corresponding to the unstable eigenvalues of the linearized dynamics. This phenomenon will be addressed in more details in the next chapter.

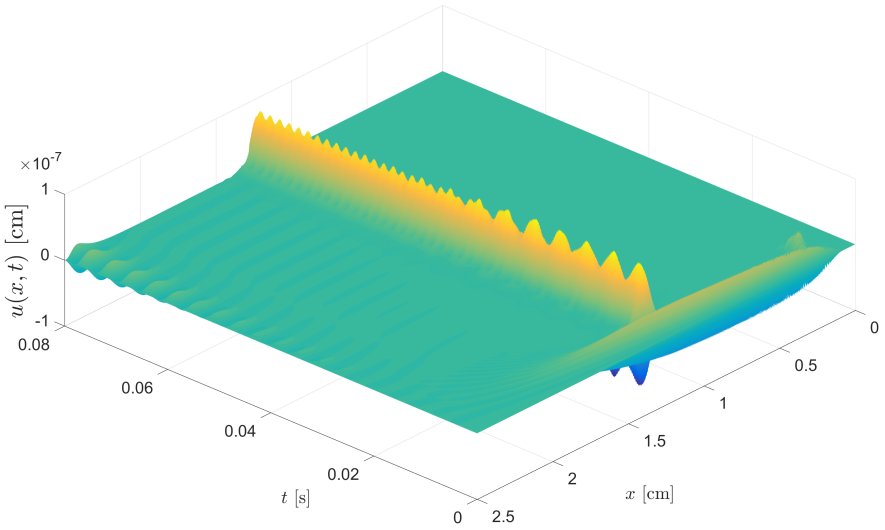

Figure 4.13: Temporal evolution of the basilar membrane profile without any input but with a spatial perturbation of the active gain $\gamma_0(x)$ as shown in Figure 4.9. The nonlinear model (2.11) was used to generate this plot with $\gamma_{max} = 1$, $\epsilon = 0.001$ and $x_p = 1.25cm$. A Limit cycle is born at the perturbed location ($x_p = 1.25cm$).

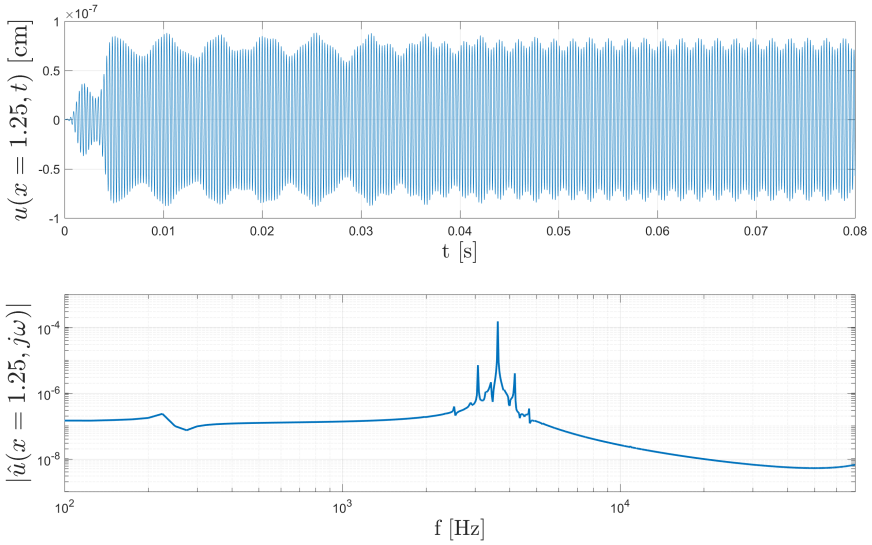

Figure 4.14: Basilar membrane vibration at the perturbed location $x = 1.25cm$ whose characteristic frequency is $3.6kHz$. The Figure at the top shows the temporal evolution. That at the bottom shows the Fourier transform that confirms that the vibration has a frequency equal to the characteristic frequency at that location in addition to the other close frequencies that are shown in Figure 4.7.

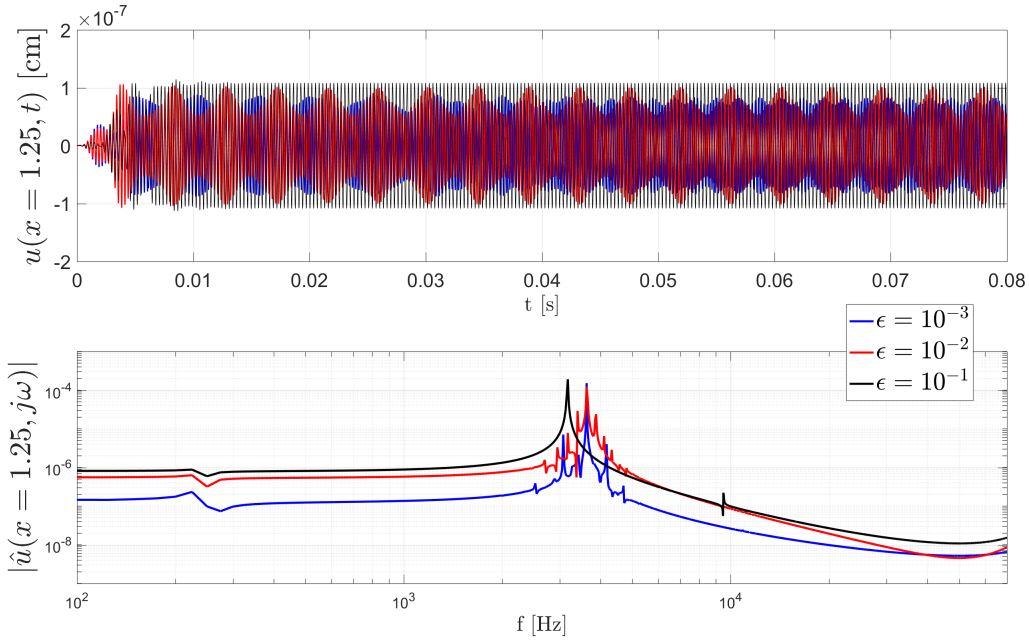

Figure 4.15: Basilar membrane vibration at the perturbed location $x = 1.25cm$ whose characteristic frequency is $3.6kHz$ for three different values of ϵ. The Figure at the top shows the temporal evolution. That at the bottom shows the Fourier transform.

Chapter 5

Cochlear Dynamic Mode Decomposition

For a linear dynamical system, one can infer almost all the information underlying the dynamics from the eigenvalues and eigenfunctions of the system A matrix. As a matter of fact, the eigenfunctions provide information about the modes and the eigenvalues provide information about the frequencies and decay rates of the corresponding modes. However, for a general nonlinear dynamical system, it is not possible to compute the modes, frequencies and decay rates from the system equations. Dynamic mode decomposition (DMD), on the other hand, has proven to give accurate approximations of the eigenvalues and eigenfunctions from data without using the system equations. In fact, DMD uses the data to compute an approximation of the A matrix in a lower dimensional subspace where the data evolve. Hence, the lower dimensional approximation is used to approximate the eigenvalues and eigenfunctions of the nonlinear system evolving in the tangent space defined by the given data. To our knowledge, DMD hasn't been applied on cochlear response yet. It is a useful tool to compute the modes of vibration and their frequencies exhibited by the nonlinear cochlear model. Moreover, DMD is particularly useful to test whether these modes are persistent or decaying in time. Furthermore, DMD can also be used to compare different cochlear models by comparing their dynamic modes rather than their temporal evolution which can be misleading: for example a small phase shift between two different models can yield a large temporal error.

This chapter first reviews the theory behind DMD. Then DMD is applied on various cochlear responses to illustrate the features that are present: detuning, otoacoustic emissions, distortion products and frequency to location mapping.

5.1 Linear Algebra Preliminaries

Before we start with the details of DMD, we state two important notions in linear algebra that are required for the derivations.

Theorem 5.1 *Consider a discrete time-invariant dynamical system defined by the evolution equation: $\psi_n = A\psi_{n-1}$ starting from a given initial condition $\psi_0 \in \mathbb{R}^{N_x}$. Let $\mu = \begin{bmatrix}\mu_1 & \mu_2 & \cdots & \mu_{N_x}\end{bmatrix}$ and $P = \begin{bmatrix}p_1 & p_2 & \cdots & p_{N_x}\end{bmatrix}$, where μ_i and p_i are the eigenvalues and eigenvectors of A, respectively. Define $\psi_{\mathbf{0}}^{\mathbf{N_t-1}} = \begin{bmatrix}\psi_0 & \psi_1 & \cdots & \psi_{N_t-1}\end{bmatrix} \in \mathbb{R}^{N_x \times N_t}$. Then:*

$$\psi_{\mathbf{0}}^{\mathbf{N_t-1}} = PD_\alpha V_{and}$$

where $\alpha := P^{-1}\psi_0$ is the coordinates of ψ_0 in the basis $\{p_1, p_2, ..., p_{N_x}\}$, $D_\alpha := diag(\alpha)$ and V_{and} is the Vandermonde matrix defined as:

$$V_{and} := \begin{bmatrix} 1 & \mu_1 & \mu_1^2 & \cdots & \mu_1^{N_t-1} \\ 1 & \mu_2 & \mu_2^2 & \cdots & \mu_2^{N_t-1} \\ \vdots & \vdots & \vdots & \cdots & \vdots \\ 1 & \mu_{N_x} & \mu_{N_x}^2 & \cdots & \mu_{N_x}^{N_t-1} \end{bmatrix} \in \mathbb{R}^{N_x \times N_t}$$

Proof: Using the eigenvalues and eigenvectors of A, one can write ψ_n in terms of the initial condition ψ_0:

$$\begin{aligned} \psi_n &= PD_\mu^n P^{-1}\psi_0 \\ &= PD_\mu^n \alpha \\ &= PD_\alpha \mu^n \end{aligned}$$

where $\mu^n := \begin{bmatrix}\mu_1^n & \mu_2^n & \cdots & \mu_{N_x}^n\end{bmatrix}^T$. Then,

$$\begin{aligned} \psi_{\mathbf{0}}^{\mathbf{N_t-1}} &= \begin{bmatrix}\psi_0 & \psi_1 & \psi_2 & \cdots & \psi_{N_t-1}\end{bmatrix} \\ &= \begin{bmatrix}PP^{-1}\psi_0 & PD_\alpha\mu & PD_\alpha\mu^2 & \cdots & PD_\alpha\mu^{N_t-1}\end{bmatrix} \\ &= PD_\alpha V_{and} \end{aligned}$$

■

Theorem 5.2 *Let $A : \mathbb{R}^{N_x} \mapsto \mathbb{R}^{N_x}$ be an $N_x \times N_x$ matrix. Let $\psi_{\mathbf{0}}^{\mathbf{N_t-1}} = \begin{bmatrix}\psi_0 & \psi_1 & \cdots & \psi_{N_t-1}\end{bmatrix} \in \mathbb{R}^{N_x \times N_t}$ whose columns span a subspace $\mathcal{S}_U$ of $\mathbb{R}^{N_x}$. Then, the optimal representation of A in the subspace $\mathcal{S}_U$ is given by $F : \mathbb{R}^r \mapsto \mathbb{R}^r$, such that*

$$F = U^* A U$$

where r is the rank of $\psi_{\mathbf{0}}^{\mathbf{N_t-1}}$ and $U \in \mathbb{R}^{N_x \times r}$ is a matrix whose columns form an orthonormal basis of $\mathcal{S}_U$. Note that U can be obtained from the economy singular value decomposition: $\psi_{\mathbf{0}}^{\mathbf{N_t-1}} = U\Sigma_r V^*$.

Proof: Let $\{u_1, u_2, ...u_r\}$ be an orthonormal basis of $\mathcal{S}_U$, obtained from the columns of U. Let w and $y \in \mathbb{R}^{N_x}$ such that $y = Aw$. The projections of w and y onto $\mathcal{S}_U$ are $w_r = U^*w$ and $y_r = U^*y$, respectively. Then, the matrix F maps w_r to y_r: $y_r = Fw_r$. To

compute F, we proceed as follows:

$$y_r = U^* y = U^* A w$$

In general, w may lie outside $\mathcal{S}_U$. However, the optimal approximation of w in $\mathcal{S}_U$ is its projection. The projection of w onto $\mathcal{S}_U$, expressed in the basis $\{u_1, u_2, ...u_r\}$, is Uw_r, thus $w \approx Uw_r$. Finally, we get $y_r \approx U^* AU w_r$. Therefore,

$$F = U^* AU$$

■

5.2 Review on DMD

The goal of dynamic mode decomposition is to decouple the spatial modes of a dynamically evolving function in separate frequencies. To be more precise, suppose we are given a function ψ of space x and time t. The goal of DMD is to find a sequence of basis functions $\phi_n(x)$, a sequence of amplitudes α_n, a sequence of decaying rates σ_n and a sequence of angular frequencies ω_n to expand ψ as follows:

$$\psi(x,t) = \sum_{n=1}^{\infty} \phi_n(x) \alpha_n e^{(\sigma_n + j\omega_n)t} \tag{5.1}$$

where $j = \sqrt{-1}$. This expansion suggests that $\psi(x,t)$ is comprised of a set of spatial modes $\phi_n(x)$. Each mode has an amplitude α_n and is evolving in time with a single frequency ω_n and a decaying rate σ_n. In practice, $\psi(x,t)$ is given as data discretized in time and space so that $\psi_i \in \mathbb{R}^{N_x}$ is a vector that represents a snapshot at a time instant $t_i = i\Delta t$ with $i = 0, 1, ..., N_t$ and Δt is the time step. Then, the DMD is given by $\psi_{\mathbf{0}}^{\mathbf{N_t - 1}} = \phi D_\alpha V_{and}$ that is the discrete space-time version of 5.1. where

$$\psi_{\mathbf{0}}^{\mathbf{N_t - 1}} := \begin{bmatrix} \psi_0 & \psi_1 & \cdots & \psi_{N_t - 1} \end{bmatrix} \in \mathbb{R}^{N_x \times N_t} \qquad \phi := \begin{bmatrix} \phi_1 & \phi_2 & \cdots & \phi_r \end{bmatrix} \in \mathbb{R}^{N_x \times r}$$

$$\alpha := \begin{bmatrix} \alpha_1 \\ \alpha_2 \\ \vdots \\ \alpha_r \end{bmatrix} \qquad V_{and} := \begin{bmatrix} 1 & \mu_1 & \mu_1^2 & \cdots & \mu_1^{N_t - 1} \\ 1 & \mu_2 & \mu_2^2 & \cdots & \mu_2^{N_t - 1} \\ \vdots & \vdots & \vdots & \cdots & \vdots \\ 1 & \mu_r & \mu_r^2 & \cdots & \mu_r^{N_t - 1} \end{bmatrix} \in \mathbb{R}^{r \times N_t}$$

such that $\mu_n = e^{(\sigma_n + j\omega_n)\Delta t}$ and r is the rank of $\psi_{\mathbf{0}}^{\mathbf{N_t - 1}}$. D_α is a diagonal matrix that arranges the vector α on the diagonal. V_{and} is the Vandermonde matrix. The rest of this section explains how to compute ϕ, α and V_{and}.

To proceed with the decomposition, we write the time evolution as follows: $\psi_n = A\psi_{n-1}$, where $A \in \mathbb{R}^{N_x \times N_x}$ is the best linear mapping that maps one snapshot to the next. If we know A, the DMD can be obtained by making use of theorem 5.1 which demonstrates

that the spatial modes are the eigenvectors of A, the amplitudes are the coordinates of the initial condition ψ_0 expressed in the basis formed of the eigenvectors, the decay rates and the frequencies are $\sigma_n + j\omega_n = \frac{1}{\Delta t}\log\mu_n$.
However, in practice, A is unknown. Even if we approximate it, computing the eigenvalues and eigenvectors of an $N_x \times N_x$ matrix is inefficient, especially if $N_x > N_t$. For this reason, theorem 5.2 is employed to provide an optimal representation of the matrix A in the subspace $\mathcal{S}_U$ spanned by the columns of $\psi_{\mathbf{0}}^{\mathbf{N_t-1}}$. This can be easily done using the economy singular value decomposition: $\psi_{\mathbf{0}}^{\mathbf{N_t-1}} = U\Sigma_r V^*$. Thus $F_{DMD} = U^*AU$. To compute F_{DMD}, by first defining another snapshot matrix $\psi_{\mathbf{1}}^{\mathbf{N_t}} := \begin{bmatrix}\psi_1 & \psi_2 & \cdots & \psi_{N_t}\end{bmatrix} \in \mathbb{R}^{N_x \times N_t}$. Since $\psi_n = A\psi_{n-1}$ for $n = 1, 2, ..., N_t$, then:

$$\begin{aligned}
\psi_{\mathbf{1}}^{\mathbf{N_t}} &= A\psi_{\mathbf{0}}^{\mathbf{N_t-1}} \\
\psi_{\mathbf{1}}^{\mathbf{N_t}} &= AU\Sigma_r V^* \\
\psi_{\mathbf{1}}^{\mathbf{N_t}} V\Sigma_r^{-1} &= AU \\
\implies F_{DMD} &= U^*AU \\
&= U^*\psi_{\mathbf{1}}^{\mathbf{N_t}} V\Sigma_r^{-1}
\end{aligned}$$

With $F_{DMD} \in \mathbb{R}^{r\times r}$ at hand, we apply theorem 5.1 on $\xi_n = F_{DMD}\xi_{n-1}$ rather than $\psi_n = A\psi_{n-1}$, where $\xi_n = U^*\psi_n$ is the projection of ψ_n onto $\mathcal{S}_U$. We get:

$$\xi_{\mathbf{0}}^{\mathbf{N_t-1}} = PD_\alpha V_{and}$$

where $P \in \mathbb{R}^{r\times r}$ is a matrix whose columns are the eigenvectors of F_{DMD}, $\alpha = P^{-1}\xi_0 = P^{-1}U^*\psi_0$, and V_{and} is the Vandermonde matrix formed from the eigenvalues $\mu = \begin{bmatrix}\mu_1 & \mu_2 & \cdots & \mu_r\end{bmatrix}^T$ of F_{DMD}. Recalling that ξ_n is the coordinates of the projection of ψ_n onto $\mathcal{S}_U$ expressed in the basis formed by the columns of U, we approximate $\psi_n \approx U\xi_n$. Therefore,

$$\psi_{\mathbf{0}}^{\mathbf{N_t-1}} \approx U\xi_{\mathbf{0}}^{\mathbf{N_t-1}} = (UP)D_\alpha V_{and}$$

To summarize, given a snapshots matrix $\psi_{\mathbf{0}}^{\mathbf{N_t}} = \begin{bmatrix}\psi_0 & \psi_1 & \psi_2 & \cdots & \psi_{N_t}\end{bmatrix}$, the dynamic mode decomposition can be calculated by following the steps in algorithm 1. This algorithm spits out the dynamic modes ϕ_n, each with amplitude α_n and evolving in time with a single frequency and decay rate $\sigma_n + j\omega_n = \frac{1}{\Delta t}\log(\mu_n)$, for $n = 1, 2, ..., r$.

5.3 Cochlear Response Features using DMD

In this section, we show important features present in the response of the cochlea using dynamic mode decomposition. In particular, we show the detuning phenomenon, frequency to location maps, distortion products and limit cycles that might be sources of spontaneous otoacoustic emissions and/or tinnitus. In the literature, these phenomena were shown using Fourier transforms. This is done by taking the Fourier transform of

Algorithm 1 DMD

1: Compute the economy singular value decomposition of $\psi_{\mathbf{0}}^{\mathbf{N_t-1}} \in \mathbb{R}^{N_x \times N_t}$:

$$\begin{aligned}\psi_{\mathbf{0}}^{\mathbf{N_t-1}} &:= \begin{bmatrix}\psi_0 & \psi_1 & \psi_2 & \cdots & \psi_{N_t-1}\end{bmatrix} \\ &= U\Sigma_r V^*\end{aligned}$$

with $r = \text{rank}(\psi_{\mathbf{0}}^{\mathbf{N_t-1}})$.

2: Compute the optimal low dimensional representation of the linear evolution matrix:

$$F_{DMD} = U^* \psi_{\mathbf{1}}^{\mathbf{N_t}} V \Sigma_r^{-1} \in \mathbb{R}^{r \times r}$$

where $\psi_{\mathbf{1}}^{\mathbf{N_t}} := \begin{bmatrix}\psi_1 & \psi_2 & \psi_3 & \cdots & \psi_{N_t}\end{bmatrix} \in \mathbb{R}^{N_x \times N_t}$.

3: Compute the eigenvalues μ_n and eigenvectors p_n of F_{DMD}.

4: Form the following matrices:

$$P := \begin{bmatrix}p_1 & p_2 & p_3 & \cdots & p_r\end{bmatrix} \in \mathbb{R}^{r \times r}$$

$$V_{and} := \begin{bmatrix}1 & \mu_1 & \mu_1^2 & \cdots & \mu_1^{N_t-1} \\ 1 & \mu_2 & \mu_2^2 & \cdots & \mu_2^{N_t-1} \\ \vdots & \vdots & \vdots & \cdots & \vdots \\ 1 & \mu_r & \mu_r^2 & \cdots & \mu_r^{N_t-1}\end{bmatrix} \in \mathbb{R}^{r \times N_t}$$

$$D_\alpha := \text{diag}(\alpha) \qquad \text{with } \alpha = P^{-1}U^*\psi_0 = \begin{bmatrix}\alpha_1 & \alpha_2 & \alpha_3 & \cdots & \alpha_r\end{bmatrix}^T \in \mathbb{R}^r$$

5: The DMD is thus given by:

$$\psi_{\mathbf{0}}^{\mathbf{N_t-1}} = \phi D_\alpha V_{and}$$

where:

$$\begin{aligned}\phi &= UP \\ &= \begin{bmatrix}\phi_1 & \phi_2 & \phi_3 & \cdots & \phi_r\end{bmatrix} \in \mathbb{R}^{r \times r}\end{aligned}$$

the time evolution of the local basilar membrane displacement at every location. This method doesn't immediately provide information about the spatial mode of vibration of the basilar membrane as a whole. To do so, further post processing of the Fourier transform is required. Moreover, it cannot predict the decay rate of a particular mode of vibration if it exists.
Before we describe the cochlear response features, we give a brief comparison between the DMD and Fourier transform approaches. We note that for all the subsequent simulations in this chapter, $\gamma_0(x) = 1$ unless explicitly stated otherwise. As an example, we apply a pressure wave at the ear drum comprised of four frequencies: $1, 4, 6$ and $10kHz$ at $60dB$ relative to the sound pressure level at the threshold of hearing ($20\mu Pa$). Figure 5.1 shows the results. The surface plot in Figure 5.1(a) shows the Fourier transform of the vibrations at each location on the basilar membrane. Whereas, Figure 5.1(b) extracts from the simulation the ten most prominent dynamic modes of vibration, where each mode vibrates at a single frequency shown in the legend of the Figure 5.1. To compare both approaches, we overlay the two Figure s such that each dynamic mode is superposed at the corresponding frequency. Figure 5.1(c) clearly shows the matching between the two different approaches.

5.3.1 Detuning

Each region on the basilar membrane responds maximally to a sound pressure wave carrying a certain frequency. This region is called the characteristic place (CP) which responds maximally to the corresponding, so called, characteristic frequency (CF). However, the characteristic place for a certain frequency is slightly variable depending on the magnitude of the stimulant. As a matter of fact, as the stimulant intensity increases, the characteristic place slightly shifts towards the stapes. This is known as detuning. To illustrate this phenomenon, we simulate the nonlinear model 2.11 at a particular single frequency, say $4.1kHz$, at different dB levels ranging from $0dB$ up to $120dB$. DMD is then used to extract the most prominent dynamic mode. Figure 5.2 shows that the characteristic place for $4.1kHz$ is at $x = 1.185cm$ for a stimulus at $0dB$ and shifts to $x = 1.079cm$ for a stimulus at $120dB$.

5.3.2 Frequency to Location Maps

For the linear cochlear model, one can plot the frequency to location map using the transfer function as done in Figure 4.5. For the nonlinear model, DMD can be employed to compute the frequency to location mapping for every dB intensity level of the stimulus. To do so, we apply a pure tone at the eardrum for different frequencies and dB intensity levels. For each simulation, we extract the most dominant dynamic mode. The characteristic place is, thus, defined to be at the peak of the dynamic mode. Figure 5.3 shows the frequency to location maps calculated using DMD for different stimulus intensity levels ranging from $0dB$ up to $120dB$. In fact, Figure 5.3 can be used to analyze

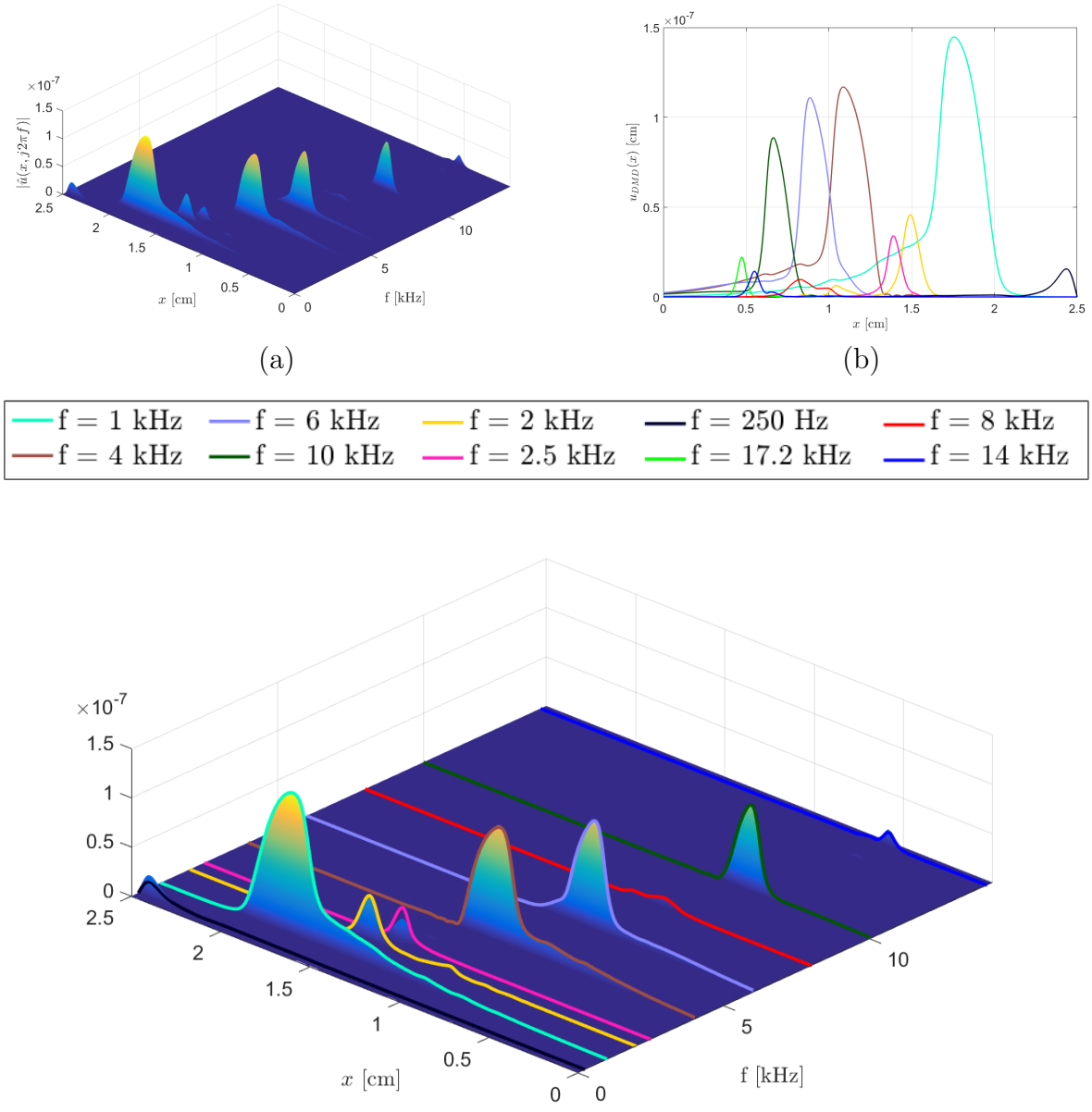

Figure 5.1: Comparison between the Fourier transform and DMD. Figure (a) shows the Fourier transform of the vibrations everywhere on the basilar membrane. Figure(b) shows the ten most prominent (in magnitude) dynamic modes of vibration. Figure (c) overlays the Fourier transform and DMD at the corresponding frequencies.

the detuning phenomenon everywhere on the basilar membrane. Particularly, it suggests that detuning at apical locations on the basilar membrane is less than basal locations

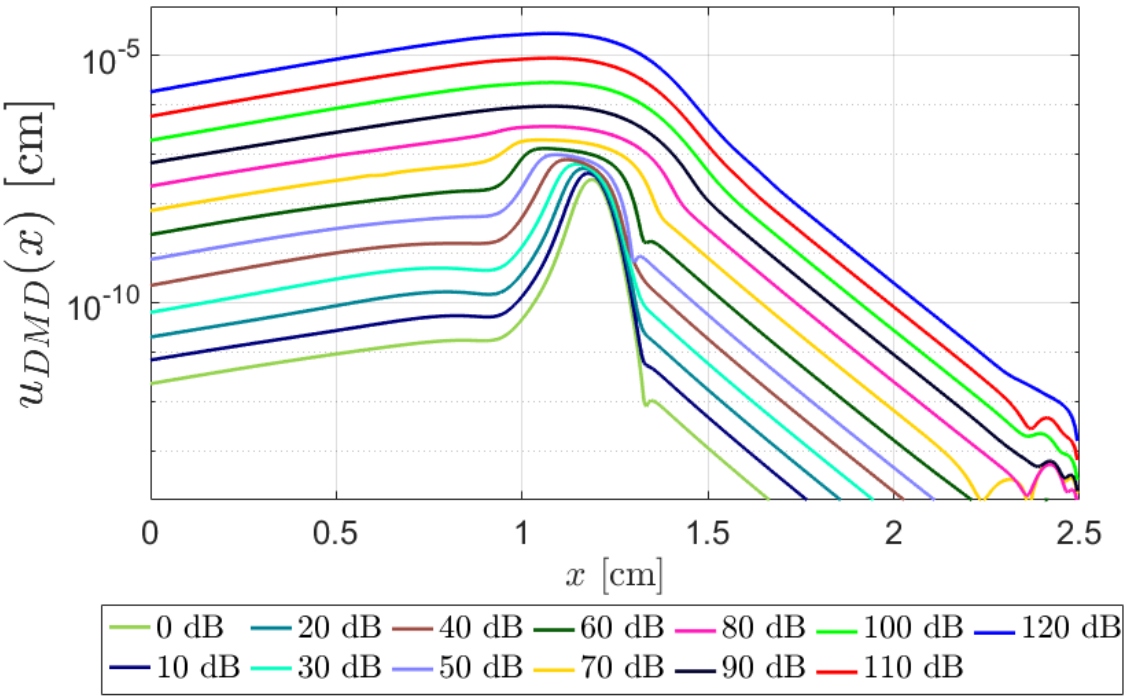

Figure 5.2: The detuning phenomenon. The most dominant dynamic mode is extracted from simulations with a pure tone stimulus at $4.1kHz$ for different dB intensity levels ranging from $0dB$ which corresponds to the threshold of hearing up to $120dB$.

where detuning can shift the characteristic place around $0.35cm$ towards the stapes.

5.3.3 Linear Instabilities and Limit Cycles

In chapter 4, possible sources of instabilities were discussed by linearizing the dynamics around the origin for different profiles of $\gamma_0(x)$. In this section, we show the dynamic modes corresponding to the two different types of linearized instabilities. To do so, we carry out a long simulation of the nonlinear model for $\gamma_0(x) = 0.95 + 0.05h(x - 1.25)$ in the absence of a stimulus, where $h(.)$ is the Heaviside function. This corresponds to the profile shown in Figure 4.9 for $\gamma_{max} = 1$, $\epsilon = 0.05$ and $x_p = 1.25cm$. This profile gives rise to the two different types of instabilities simultaneously. Figure 5.4 shows the dominant dynamic modes. The blue curve, representing the dynamic mode vibrating at $245Hz$, corresponds to the limit cycle caused by the linearized instability of a high gain level. On the other hand, the red, magenta and black curves represent the dynamic modes caused by the linearized instabilities due to the spatial gain perturbation.
As mentioned earlier in section 4.4, for larger values of the perturbation ϵ, the different

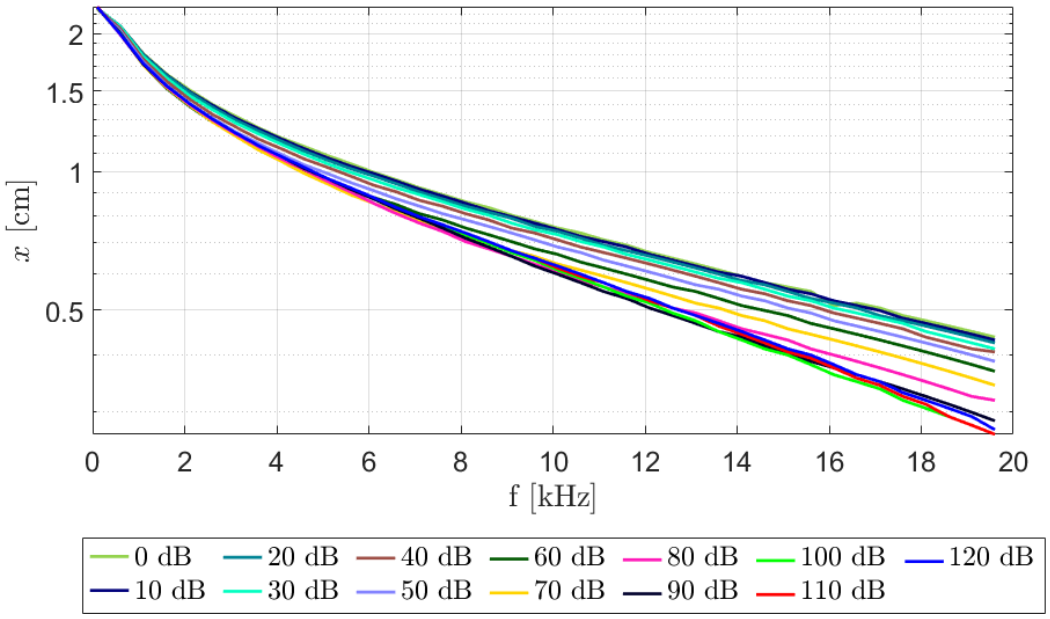

Figure 5.3: Frequency to location map of the nonlinear cochlear model at different dB intensity levels of the stimulus.

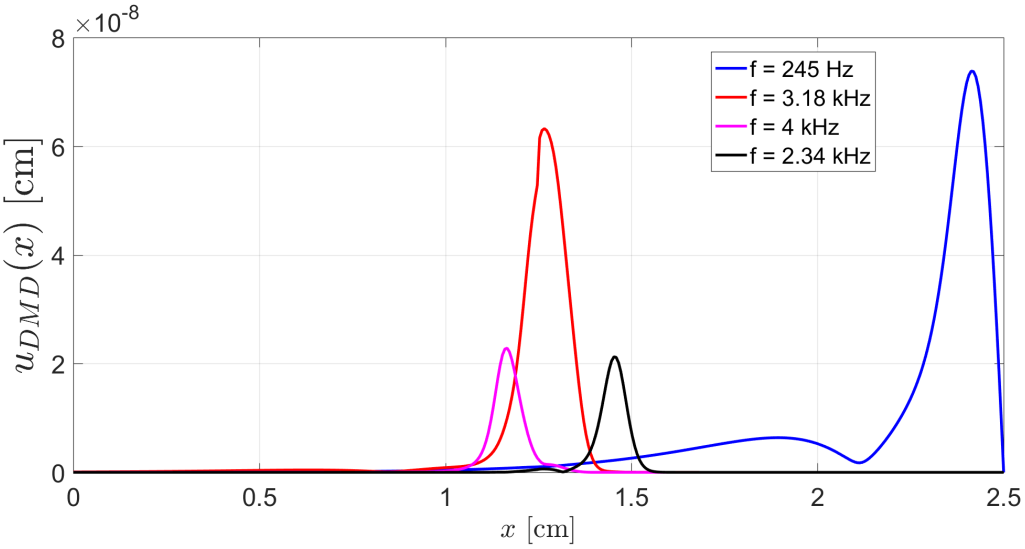

Figure 5.4: Dominant dynamic modes of the basilar membrane vibrations in the absence of a stimulus for $\gamma_0(x) = 0.95 + 0.05h(x - 1.25)$.

frequencies of the vibration at the location of perturbation merge to become a single frequency. In addition to that, it is observed that the 3 modes of vibration corresponding

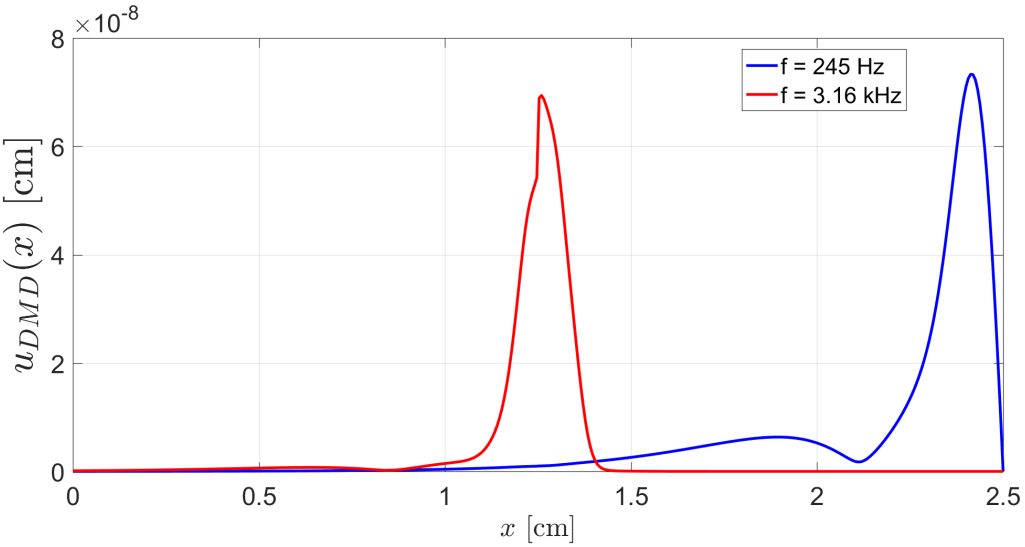

Figure 5.5: Dominant dynamic mode of the basilar membrane vibrations in the absence of a stimulus for $\gamma_0(x) = 0.9 + 0.1h(x - 1.25)$.

to the linearized instability at the perturbation also merge to become a single dynamic mode. As an example, we set the linearized active gain $\gamma_0(x) = 0.9 + 0.1h(x - 1.25)$ and compute the dominating dynamic modes. Figure 5.5 shows that only one dynamic mode vibrating at $3.17kHz$ emerges from the large gain perturbation. This observation might be related to tinnitus or spontaneous otoacoustic emission where a single frequency is perceived. A large perturbation of the structural properties at a particular location at the basilar membrane causes the perception/emission of a single pure tone.

5.3.4 Distortion Products

When the ear is stimulated with two tones, the ear produces additional fill-in frequencies called the distortion-products otoacoustic emissions. Perhaps the most dominant distortion product is the Cubic Distortion Tone (CDT): if a sound wave comprised of two frequencies f_1 and f_2 ($f_1 < f_2$) stimulates the ear, a CDT of frequency $2f_1f_2$ is emitted back to the eardrum. This is believed to be caused by vibrations at the characteristic place of the CDT. For example, we stimulate the ear by two tones of $f_1 = 7kHz$ and $f_2 = 10kHz$ at $60dB$. The most prominent distortion product corresponds to the dynamic mode vibrating at a frequency of $4kHz$. This is the mode corresponding to the CDT. Additional persistent dynamic modes vibrate at 1 and $2kHz$. We note that other modes, not shown here, also exist for this stimulus. These modes have smaller magnitudes and are not persistent in the sense that their decay rates are large. Decaying modes might be useful in the analysis of the transient behavior which is not in the scope of this paper.

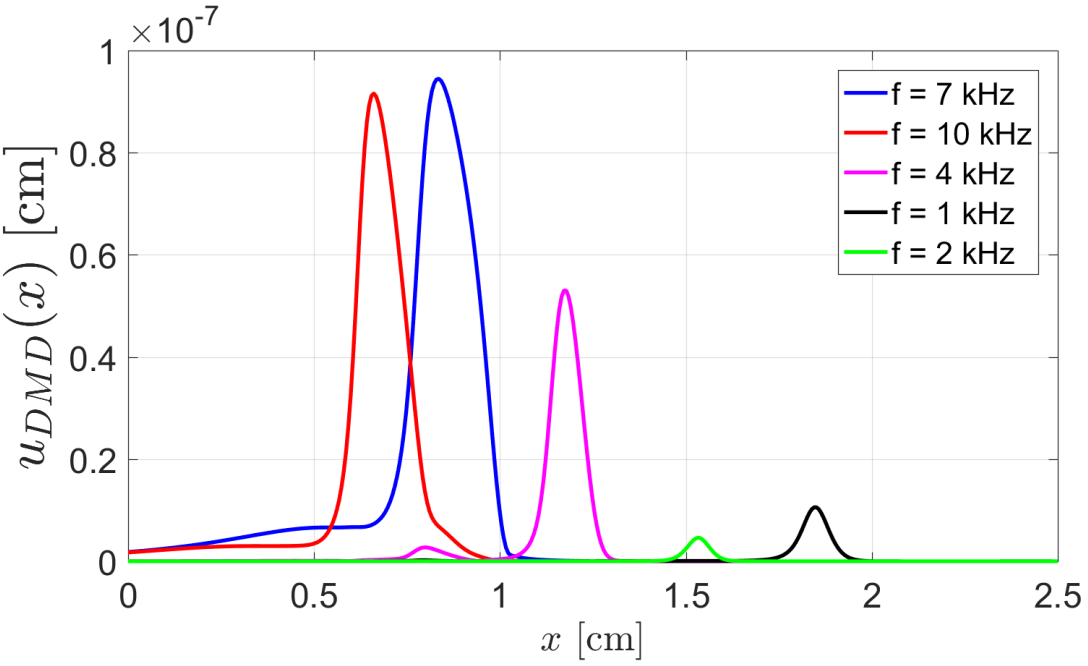

Figure 5.6: Dominant dynamic modes of the basilar membrane vibrations for a stimulus of two tones of 7 and $10kHz$ at $60dB$.

5.4 Conclusion

This chapter reviewed the theory underlying dynamic mode decomposition and a comparison with Fourier transforms was given. Then, DMD was applied on cochlear response to different stimuli. Typical features in cochlear response was shown using DMD. To our knowledge, two new observations were made using the dynamic modes extracted: (a) the detuning phenomenon is more intense on apical locations on the basilar membrane and (b) large perturbations of the structural properties of the cochlea at a particular location initiate a limit cycle vibrating at a single frequency. The second observation might be an explanation of tinnitus or spontaneous otoacoustic emissions of a single pure tone.

Chapter 6

Estimating Basilar Membrane Vibration using Extended Kalman Filters

Taking measurements of vibrations in the cochlea is essential to understand the underlying mechanics. Throughout the literature, several experiments and techniques were devised to take measurements (in vivo and in vitro) of vibrations in the cochlea ([26], [27], [1]). Recently, displacement-sensitive heterodyne laser interferometers are most widely used to measure extremely small vibrations, in the order of nanometers, as in the case of the cochlea ([28], [29]). However, these techniques give only point-wise measurements as the laser is directed towards a single vibrating point. Furthermore, to understand the active nature of the cochlea, measurements need to be done while the cochlea is still intact. In fact, particular locations might be easier to measure in order to avoid destroying structures in the cochlea.

This chapter aims at estimating distributed spatial vibrations using (1) developed mathematical models for the cochlea and (2) (simulated) point-wise measurements given, for example, by the laser interferometer. Particularly, extended Kalman filters are used for the estimation process since the cochlear model is nonlinear.

6.1 Kalman Filter Framework in Distributed Environments

In this section, we review the work done by [30] to describe the Kalman filter algorithm for linear spatio-temporal distributed systems. The algorithm is very similar to the finite dimensional case, however the notation needs to be stated carefully.

Let x and t be the space and time variables, respectively. Consider the linear distributed system given in descriptor state space form, with a state space variable ψ, an

input u and an output y:

$$\mathcal{E}\frac{\partial}{\partial t}\psi(x,t) = \mathcal{A}\psi(x,t) + \mathcal{B}u(x,t) + \mathcal{L}w(x,t); \quad \psi(x,0) = \psi_0(x)$$
$$y_k = \mathcal{C}\psi_k(x) + v_k$$

where $\mathcal{A}, \mathcal{B}, \mathcal{L}, \mathcal{E}$ and $\mathcal{C}$ are matrices of linear operators. ψ, u and w are vectors of functions. The output equation is given in discrete time such that $y_k := y(t_k)$, $\psi_k(x) := \psi(t_k, x)$ and $v_k := v(t_k)$ are vectors, where $t_k := k\Delta t$ and Δt is the time step. The process noise w and measurement noise v are assumed to be uncorrelated Gaussian white noise such that:

$$\begin{aligned} E\{w(x,t)w^*(\chi,\tau)\} &= Q_c(x,\chi)\delta(t-\tau) \\ E\{w(x,t)\} &= 0 \\ E\{v_k, v_k^T\} &= R_k \\ E\{v_k\} &= 0 \\ E\{w(x,t)v_k\} &= 0 \end{aligned}$$

where w^* is the adjoint of w, $Q_c(x,\xi)$ is the covariance kernel of w and R_k is the covariance matrix of v_k. Clearly, we are dealing with a hybrid system where the state evolution equation is in continuous time, and the measurement equation is in discrete time. Now, define the state estimate $\hat{\psi}$ and the state estimation error covariance $\mathcal{P}$ as follows:

$$\begin{aligned} &\hat{\psi}(x,t) = E\{\psi(x,t)\} \\ &E\left\{\left(\psi(x,t) - \hat{\psi}(x,t)\right)\left(\psi(\chi,\tau) - \hat{\psi}(\chi,\tau)\right)^*\right\} = \mathcal{P}(x,\chi;t)\delta(t-\tau) \end{aligned} \tag{6.1}$$

For notational convenience, the covariance kernel evaluated at time instant t_k is denoted by $\mathcal{P}_k(x,\chi)$. The discrete time covariance kernel of the measurement noise is approximated by $\mathcal{Q}(x,\chi) = \mathcal{Q}_c(x,\chi)(1-e^{-\Delta t})$. Moreover, define the state transition operator $\mathcal{F} := e^{\mathcal{E}^{-1}\mathcal{A}\Delta t}$. Therefore, the Kalman filter algorithm for distributed hybrid systems can be stated as follows:

1. **Initialization**: Set $k = 1$ and start with some initial estimates of the state and the covariance kernel:
   - $\hat{\psi}_0^+(x)$
   - $P_0^+(x,\xi)$
2. **Model Dynamics** : Propagate the state and the covariance kernel through the model dynamics from time instants t_{k-1} to t_k:
   - Integrate $\mathcal{E}\frac{\partial}{\partial t}\hat{\psi}(x,t) = \mathcal{A}\hat{\psi}(x,t) + \mathcal{B}u(x,t)$ from $\{t_{k-1}, \hat{\psi}_{k-1}^+(x)\}$ to $\{t_k, \hat{\psi}_k^-(x)\}$
   - Compute: $\mathcal{P}_k^-(x,\chi) = \mathcal{F}\mathcal{P}_{k-1}^+(x,\chi)\mathcal{F}^* + \mathcal{L}\mathcal{Q}(x,\chi)\mathcal{L}^*$
3. **Kalman Gain**: Calculate the optimal Kalman gain:

- $K_k(x) = \mathcal{P}_k^-(x,\chi)\mathcal{C}^* \left[\mathcal{C}\mathcal{P}_k^-(x,\chi)\mathcal{C}^* + \mathcal{R}_k\right]^{-1}$

4. **Measurement Update**: Update the state and covariance kernel estimates from the model dynamics by incorporating the measurement information:

   - $\hat{\psi}_k^+(x) = \hat{\psi}_k^-(x) + K_k(x)\left[y_k - \mathcal{C}\hat{\psi}_k^-(x)\right]$
   - $\mathcal{P}_k^+(x,\chi) = \left[\mathcal{I} - K_k(x)\mathcal{C}\right]\mathcal{P}_k^-(x,\chi)\left[\mathcal{I} - K_k(x)\mathcal{C}\right]^* + K_k(x)R_kK_k(x)^*$

   Set $k = k+1$ and go to step 2.

where " $*$ " is the adjoint operator. Note that, operators acting from the left side operate on the first spatial variable x, and those acting form the right side operate on the second spatial variable χ.
For a linear system, the operator $\mathcal{F}$ can be calculated once and off-line. However, for nonlinear systems of the form:

$$\mathcal{E}\frac{\partial}{\partial t}\psi(x,t) = [f(\psi,u)](x,t) + \mathcal{L}w(x,t); \qquad \psi(x,0) = \psi_0(x)$$

Extended Kalman filters can be employed instead. The Extended Kalman filter is the same as the algorithm stated above except that Step 2 is replace by the following:

- Integrate $\mathcal{E}\frac{\partial}{\partial t}\hat{\psi}(x,t) = [f(\hat{\psi},u)](x,t)$ from $\{t_{k-1}, \hat{\psi}_{k-1}^+(x)\}$ to $\{t_k, \hat{\psi}_k^-(x)\}$
- Compute: $\mathcal{P}_k^-(x,\chi) = \mathcal{F}_k\mathcal{P}_{k-1}^+(x,\chi)\mathcal{F}_k^* + \mathcal{L}\mathcal{Q}(x,\chi)\mathcal{L}^*$

where: $\mathcal{F}_k := e^{\mathcal{E}^{-1}\mathcal{A}_k\Delta t}$ and $\mathcal{A}_k := \frac{\partial}{\partial\psi}f(\psi_k,u_k)$. Note that, for extended Kalman filters, $\mathcal{F}_k$ is not a constant anymore and it has to be calculated at each time step. In this chapter, the Pade approximation method was used to efficiently calculate the exponential of a matrix.

6.2 System Linearization

In order to apply the extended Kalman filter to the cochlear model given in descriptor form (2.11), we proceed by linearizing the system dynamics around some given state $\bar{\psi} = \begin{bmatrix}\bar{u} & \bar{v} & \dot{\bar{u}} & \dot{\bar{v}}\end{bmatrix}^T$. Hence, we wish to give a linear approximation of the nonlinear operator defined by $f(\psi) := \mathcal{A}_u\psi$ around $\bar{\psi}$, where $\mathcal{A}_u$ is repeated here for convenience.

$$\mathcal{A}_u := \begin{bmatrix} 0 & 0 & \mathcal{I} & 0 \\ 0 & 0 & 0 & \mathcal{I} \\ \gamma(u)k_4 - (k_1+k_3) & k_3 - \gamma(u)k_4 & \gamma(u)c_4 - (c_1+c_3) & c_3 - \gamma(u)c_4 \\ k_3 & -(k_2+k_3) & c_3 & -(c_2+c_3) \end{bmatrix}$$

We can rewrite $\mathcal{A}_u$ as a sum of two terms: $\mathcal{A}_u = \mathcal{A}_0 + \mathcal{B}_0\gamma(u)\mathcal{C}_0$, where

$$\mathcal{A}_0 := \begin{bmatrix} 0 & 0 & \mathcal{I} & 0 \\ 0 & 0 & 0 & \mathcal{I} \\ -(k_1+k_3) & k_3 & -(c_1+c_3) & c_3 \\ k_3 & -(k_2+k_3) & c_3 & -(c_2+c_3) \end{bmatrix} \quad \mathcal{B}_0 := \begin{bmatrix} 0 \\ 0 \\ \mathcal{I} \\ 0 \end{bmatrix}$$
$$\mathcal{C}_0 := \begin{bmatrix} k_4 & -k_4 & c_4 & -c_4 \end{bmatrix} \qquad \mathcal{C} := \begin{bmatrix} \mathcal{I} & 0 & 0 & 0 \end{bmatrix}$$

Let $\tilde{\psi}$ be a small perturbation from $\bar{\psi}$ so that $\psi = \bar{\psi} + \tilde{\psi}$.
Then $f(\psi) = f(\bar{\psi} + \tilde{\psi}) \approx f(\bar{\psi}) + \left[\frac{\partial}{\partial\psi} f(\bar{\psi})\right]\left(\tilde{\psi}\right)$, where $\left[\frac{\partial}{\partial\psi} f(\bar{\psi})\right]\left(\tilde{\psi}\right)$ is the Fréchet derivative of f evaluated at $\bar{\psi}$ in the direction of the perturbation $\tilde{\psi}$. The Fréchet derivative is calculated to be:

$$\left[\frac{\partial}{\partial\psi} f(\bar{\psi})\right]\left(\tilde{\psi}\right) = \left[\mathcal{A}_{\bar{u}}\right]\left(\tilde{\psi}\right) + \left[d\mathcal{A}_{\bar{\psi}}\right]\left(\tilde{\psi}\right)$$

where $d\mathcal{A}_{\bar{\psi}}$ is a linear operator whose action on $\tilde{\psi}$ is defined as follows:

$$\left[d\mathcal{A}_{\bar{\psi}}\right](\tilde{\psi}) := \mathcal{B}_0 \left[\frac{\partial}{\partial u}\gamma(\bar{u})\right]\left(\mathcal{C}\tilde{\psi}\right)\mathcal{C}_0\bar{\psi}$$

such that $\left[\frac{\partial}{\partial u}\gamma(\bar{u})\right](\tilde{u})$ is the Fréchet derivative of the active gain γ evaluated at $\bar{u}$ in the direction of the BM perturbation $\tilde{u}$ and it is easy to show that:

$$\left[\frac{\partial}{\partial u}\gamma(\bar{u})\right](\tilde{u})\Big|_x = -\frac{2\theta}{R^2}\frac{\gamma_0(x)\left[\mathcal{G}_\lambda(\bar{u}\tilde{u})\right](x)}{\left(1+\theta\left[\mathcal{G}_\lambda\left(\frac{u^2}{R^2}\right)\right](x)\right)^2}$$

To summarize, given the cochlear model in (2.11): $\mathcal{E}\frac{\partial}{\partial t}\psi = \mathcal{A}_u\psi + \mathcal{B}\ddot{s}$, the linearized dynamics around $\bar{\psi} = \begin{bmatrix}\bar{u} & \bar{v} & \dot{\bar{u}} & \dot{\bar{v}}\end{bmatrix}^T$ are given by:

$$\mathcal{E}\frac{\partial}{\partial t}\psi = \left(\mathcal{A}_{\bar{u}} + d\mathcal{A}_{\bar{\psi}}\right)\psi + \mathcal{B}\ddot{s} - d\mathcal{A}_{\bar{\psi}}\bar{\psi} \tag{6.2}$$

where

$$\mathcal{E} := \begin{bmatrix} \mathcal{I} & 0 & 0 & 0 \\ 0 & \mathcal{I} & 0 & 0 \\ 0 & 0 & m_1\mathcal{I} + \mathcal{M}_f & 0 \\ 0 & 0 & 0 & m_2\mathcal{I} \end{bmatrix} \qquad \mathcal{B} := \begin{bmatrix} 0 \\ 0 \\ -\mathcal{M}_s \\ 0 \end{bmatrix}$$
$$\mathcal{A}_{\bar{u}} := \begin{bmatrix} 0 & 0 & \mathcal{I} & 0 \\ 0 & 0 & 0 & \mathcal{I} \\ \gamma(\bar{u})k_4 - (k_1+k_3) & k_3 - \gamma(\bar{u})k_4 & \gamma(\bar{u})c_4 - (c_1+c_3) & c_3 - \gamma(\bar{u})c_4 \\ k_3 & -(k_2+k_3) & c_3 & -(c_2+c_3) \end{bmatrix}$$

$$\left[d\mathcal{A}_{\bar{\psi}}\right](\tilde{\psi}) := \mathcal{B}_0\left[\frac{\partial}{\partial u}\gamma(\bar{u})\right]\left(\mathcal{C}\tilde{\psi}\right)\mathcal{C}_0\bar{\psi}$$

$$\mathcal{B}_0 := \begin{bmatrix}0\\0\\\mathcal{I}\\0\end{bmatrix} \qquad \mathcal{C}_0 := \begin{bmatrix}k_4 & -k_4 & c_4 & -c_4\end{bmatrix} \qquad \mathcal{C} := \begin{bmatrix}\mathcal{I} & 0 & 0 & 0\end{bmatrix}$$

$$[\gamma(u)](x) := \frac{\gamma_0(x)}{1+\theta\left[\mathcal{G}_\lambda\left(\frac{u^2}{R^2}\right)\right](x)} \qquad \left[\frac{\partial}{\partial u}\gamma(\bar{u})\right](\tilde{u})\Big|_x = -\frac{2\theta}{R^2}\frac{\gamma_0(x)\left[\mathcal{G}_\lambda(\bar{u}\tilde{u})\right](x)}{\left(1+\theta\left[\mathcal{G}_\lambda\left(\frac{u^2}{R^2}\right)\right](x)\right)^2}$$

We note that, given the finite realization of the operator $\mathcal{G}_\lambda$ in (3.4), we can realize the operators $\frac{\partial}{\partial u}\gamma(\bar{u})$ and $d\mathcal{A}_{\bar{u}}$ by the following matrices, respectively:

$$d\Gamma_{\bar{u}} := -\frac{2\theta}{R^2}\mathcal{D}\{\gamma_0\}\mathcal{D}\left\{\left(1+\frac{\theta}{R^2}G_\lambda\bar{u}^2\right)^{-2}\right\}G_\lambda\mathcal{D}\{\bar{u}\}$$

$$dA_{\bar{\psi}} := B_0\mathcal{D}\{C_0\bar{\psi}\}d\Gamma_{\bar{u}}C$$

where all the variables here are meant to be vectors with each entry corresponding to a spatial location x. $\mathcal{D}$ is the operator that forms a diagonal matrix from a vector.

6.3 Numerical Results and Analysis

In this section, we use a sound signal of three tones at 1, 4 and 8kHz with a magnitude of 60dB to simulate the cochlear model with a grid size of $N_x = 500$. This simulation is used to generate the measurements. Now, to study the performance of the Kalman filter, we carry out two scenarios as described in the subsequent section. In order to design the process and measurement noise covariances Q_c and R_c, we note the order of vibrations, velocities and accelerations of the Tactorial and Basilar membranes. Displacements are in the order of 1nm, velocities are in the order of 1cms^{-1}. Accelerations are in the order of 100cms^{-2}. These values are the basis of the selection of the modeled process and measurement noise. Before presenting simulation results, we define an error measure on which we base our comparisons. Let $\hat{u}(x;t)$ be an estimate of $u(x;t)$, then the error is defined to be:

$$e(t) = \frac{\int_0^L (u(x,t)-\hat{u}(x,t))^2 dx}{\int_0^L u^2(x,t)dx} \tag{6.3}$$

Furthermore, for the purpose of reducing the computational load of the extended Kalman filter, the linearization of the dynamics is not carried out at each time step. In fact, the linearization is carried out N_l times such that the Jacobians are approximated to be equal between two subsequent linearizations. We leave N_l as a design parameter that compromises between the desired accuracy and the computational load. In the subsequent sections, we set $N_l = 100$.

6.3.1 Uncertain Initial Conditions

In this section, we assume that we have a perfect model of the cochlea with perfect measurements. However, the initial conditions are assumed to be unknown. First, we spread 20 equally spaced sensors on each of the two membranes to take measurements of the displacements. The design parameters of the filter are as follows:

$$\mathcal{Q} = \begin{bmatrix} 10^{-4}\mathcal{I}\mathrm{cm}^2\,\mathrm{s}^{-2} & 0 & 0 & 0 \\ 0 & 10^{-4}\mathcal{I}\mathrm{cm}^2\,\mathrm{s}^{-2} & 0 & 0 \\ 0 & 0 & 10^{4}\mathcal{I}\mathrm{cm}^2\,\mathrm{s}^{-4} & 0 \\ 0 & 0 & 0 & 10^{4}\mathcal{I}\mathrm{cm}^2\,\mathrm{s}^{-4} \end{bmatrix};$$

$$\mathcal{P}_0 = \begin{bmatrix} 10^{-10}\mathcal{I}\mathrm{cm}^2 & 0 & 0 & 0 \\ 0 & 10^{-10}\mathcal{I}\mathrm{cm}^2 & 0 & 0 \\ 0 & 0 & \mathcal{I}\mathrm{cm}^2\,\mathrm{s}^{-2} & 0 \\ 0 & 0 & 0 & \mathcal{I}\mathrm{cm}^2\,\mathrm{s}^{-2} \end{bmatrix}; \qquad \mathcal{R} = 10^{-24}\mathcal{I}\mathrm{cm}^2;$$

where $\mathcal{I}$ is the identity operator. These design parameters reflect our trust in our modeled dynamics and the available measurements. But the large initial covariance $\mathcal{P}_0$ reflects our distrust in our estimation of the initial condition.

To asses the precision of the designed extended kalman filter and how well it responds to uncertain initial conditions, we generate a random initial condition as shown in Figure 6.1(a). The initial condition is considerably erroneous compared to the true initial condition which is zero. The rest of Figure 6.1 shows three snapshots of the BM displacement profile at $t = 0.1, 0.5$ and 3ms, respectively. Clearly, the extended kalman filter locks to the true profile after some time. To show this more explicitly, we plot the time evolution of the estimation error using equation (6.3) in the presence and absence of measurements. Figure 6.2 shows that in the absence of measurements, the error decreases to some steady state value. On the other hand, with available measurements, the error is large initially because of the erroneous estimate of the initial condition. However, it decreases with time until the estimate locks onto the true states. Furthermore, we test the performance of the extended Kalman filter by spreading less sensors. Figure 6.3 shows the time evolution of the relative estimation error as computed using equation (6.3) for the case where no measurements are available, and for 20, 10 and 5 sensors spread equally on each of the two membranes. Clearly, the estimation accuracy is higher when more sensors are introduced.

6.3.2 Uncertain Model Dynamics

In this section, we asses the robustness of the designed filter when the available model is inaccurate. First, we start by choosing a grid size $N_x = 200$ instead of $N_x = 500$. This coarse discretization of the spatial variable introduces erroneous behavior of the dynamics. Particularly, linearized instabilities arise near the stapes for such coarse grids. Figure 6.4 (a) shows a snapshot at $t = 10$ms of the true and estimated basilar membrane

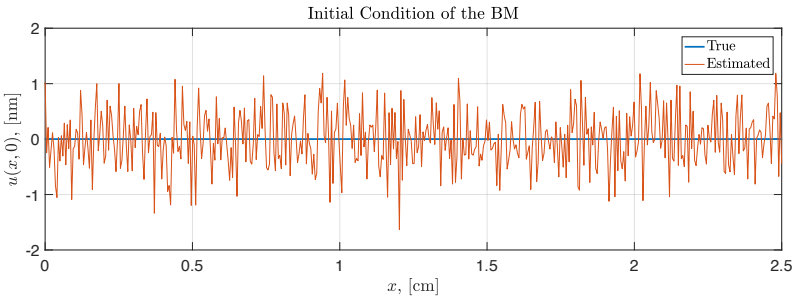

(a)

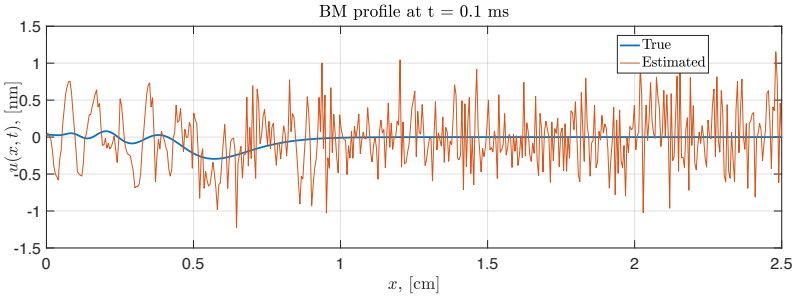

(b)

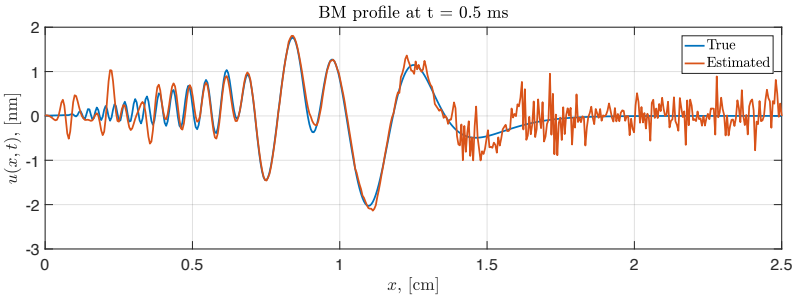

(c)

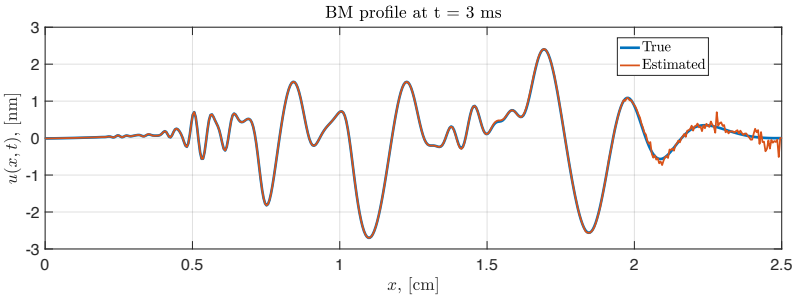

(d)

Figure 6.1: Snapshots of the true and estimated basilar membrane displacement profile. The figure to the top shows the true initial condition which is zero but assumed to be unknown. The estimated initial condition is randomly generated to asses the response of the extended Kalman filter to uncertain initial conditions. The subsequent figures show three snapshots of the BM displacement profile at $t = 0.1, 0.5$ and 3ms, respectively.

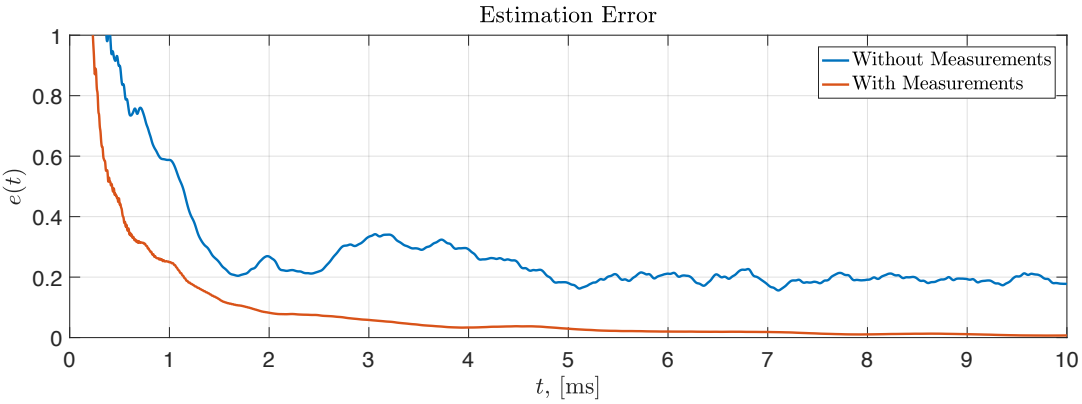

Figure 6.2: The evolution of the estimation error in the presence and absence of measurements.

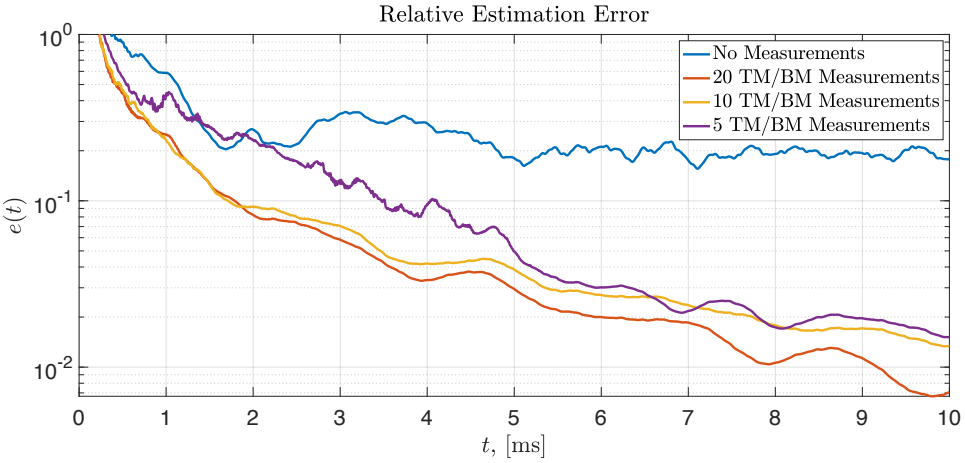

Figure 6.3: Comparison of the relative estimation error for different number of measurements.

profiles where 20 sensors are equally spread along the two membranes. Figure 6.4 shows the relative estimation error with and without measurements. The filter is doing a good job in rejecting the linearized instabilities that occur near the stapes. However, small oscillations were inevitable. To get rid of these kind of artifacts, more sensors can be deployed near the stapes.

Finally, we asses the performance of the filter when there are defects in the structural parameters of the model. For example, we modify θ and λ from their values given in table 2 to be 0.7 and 0.4, respectively. Figure 6.5(a) shows snapshots of the true and estimated basilar membrane profiles at $t = 10$ms where, again, 20 sensors are equally spread along the two membranes. In the absence of measurements, the relative estimation error is around 25%, which shows the sensitivity of the model to the values of the defected parameters θ and λ. However, with measurements available, the estimation error drops to less than 10%.

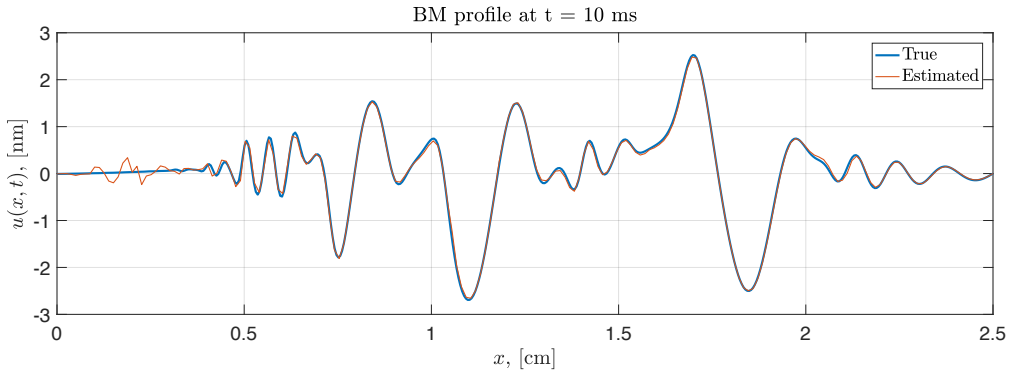

(a)

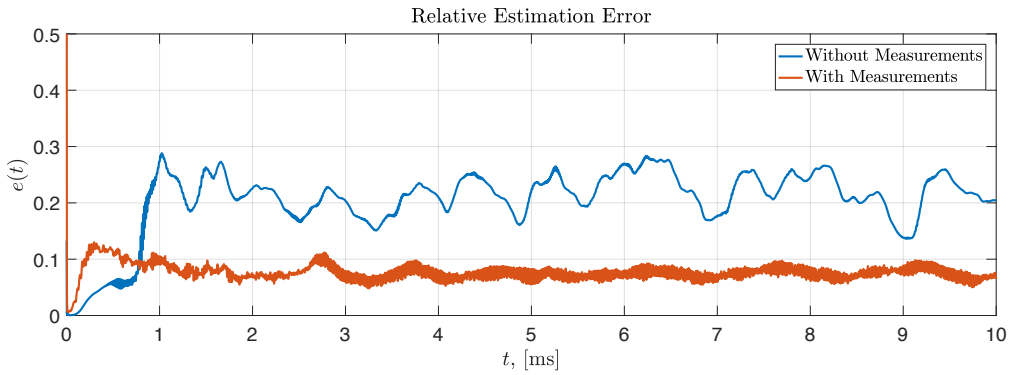

(b)

Figure 6.4: Estimation performance of the extended Kalman filter with a coarse spatial grid. (a) Snapshots of the true and estimated basilar membrane displacement profile. (b) The evolution of the estimation error in the presence and absence of measurements.

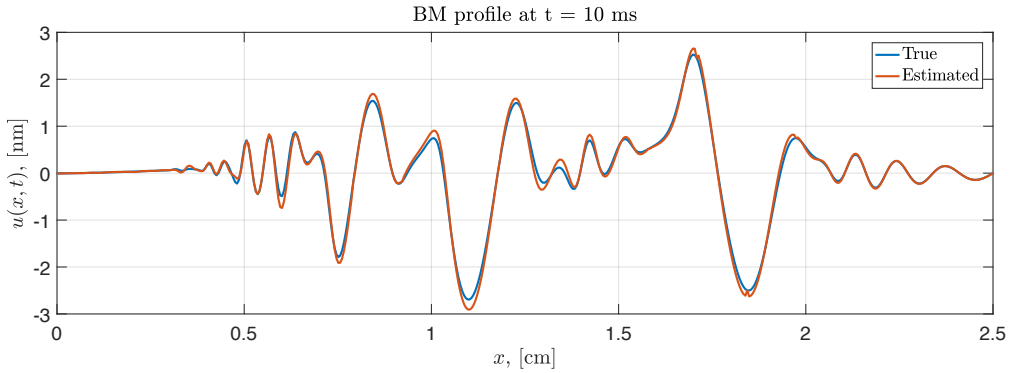

(a)

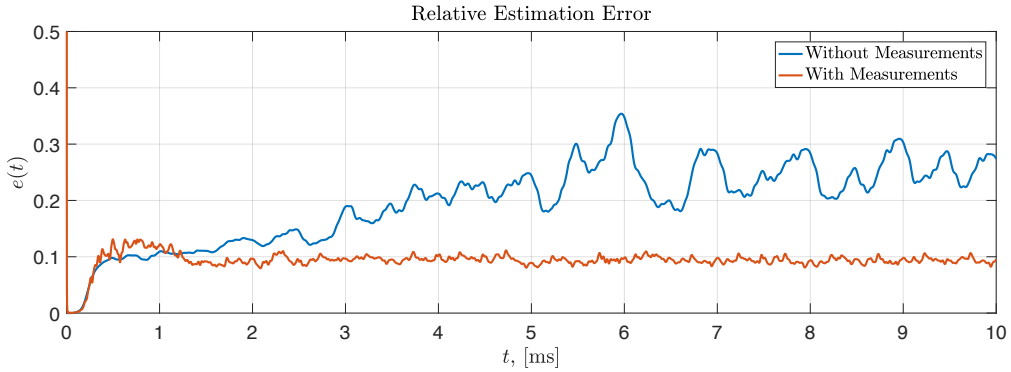

(b)

Figure 6.5: Estimation performance of the extended Kalman filter with defected parameters. (a) Snapshots of the true and estimated basilar membrane displacement profile. (b) The evolution of the estimation error in the presence and absence of measurements.

Bibliography

[1] S. S. Gao, R. Wang, P. D. Raphael, Y. Moayedi, A. K. Groves, J. Zuo, B. E. Applegate, and J. S. Oghalai, "Vibration of the organ of corti within the cochlear apex in mice," *Journal of neurophysiology*, pp. jn–00306, 2014.

[2] H. Y. Lee, P. D. Raphael, J. Park, A. K. Ellerbee, B. E. Applegate, and J. S. Oghalai, "Noninvasive in vivo imaging reveals differences between tectorial membrane and basilar membrane traveling waves in the mouse cochlea," *Proceedings of the National Academy of Sciences*, vol. 112, no. 10, pp. 3128–3133, 2015.

[3] L. Robles and M. A. Ruggero, "Mechanics of the mammalian cochlea," *Physiological reviews*, vol. 81, no. 3, pp. 1305–1352, 2001.

[4] G. Von Békésy and E. G. Wever, *Experiments in hearing*, vol. 8. McGraw-Hill New York, 1960.

[5] M. R. Hasan, M. Jamil, M. G. R. M. S. Rahman, *et al.*, "Speaker identification using mel frequency cepstral coefficients," *variations*, vol. 1, no. 4, 2004.

[6] A. Eronen and A. Klapuri, "Musical instrument recognition using cepstral coefficients and temporal features," in *Acoustics, Speech, and Signal Processing, 2000. ICASSP'00. Proceedings. 2000 IEEE International Conference on*, vol. 2, pp. II753–II756, IEEE, 2000.

[7] B. Logan *et al.*, "Mel frequency cepstral coefficients for music modeling.," in *ISMIR*, 2000.

[8] S. S. Stevens, J. Volkmann, and E. B. Newman, "A scale for the measurement of the psychological magnitude pitch," *The Journal of the Acoustical Society of America*, vol. 8, no. 3, pp. 185–190, 1937.

[9] A. Hudspeth, "Making an effort to listen: mechanical amplification in the ear," *Neuron*, vol. 59, no. 4, pp. 530–545, 2008.

[10] S. S. Narayan, A. N. Temchin, A. Recio, and M. A. Ruggero, "Frequency tuning of basilar membrane and auditory nerve fibers in the same cochleae," *Science*, vol. 282, no. 5395, pp. 1882–1884, 1998.

[11] W. Murphy, C. Talmadge, A. Tubis, and G. Long, "Relaxation dynamics of spontaneous otoacoustic emissions perturbed by external tones. i. response to pulsed single-tone suppressors," *The Journal of the Acoustical Society of America*, vol. 97, no. 6, pp. 3702–3710, 1995.

[12] M. van der Heijden and P. X. Joris, "Panoramic measurements of the apex of the cochlea," *Journal of Neuroscience*, vol. 26, no. 44, pp. 11462–11473, 2006.

[13] D. Bendor and X. Wang, "The neuronal representation of pitch in primate auditory cortex," *Nature*, vol. 436, no. 7054, pp. 1161–1165, 2005.

[14] E. R. Joosten and P. Neri, "Human pitch detectors are tuned on a fine scale, but are perceptually accessed on a coarse scale," *Biological cybernetics*, pp. 1–18, 2012.

[15] A. V. Medvedev, F. Chiao, and J. S. Kanwal, "Modeling complex tone perception: grouping harmonics with combination-sensitive neurons," *Biological cybernetics*, vol. 86, no. 6, pp. 497–505, 2002.

[16] J. O. Pickles, *An introduction to the physiology of hearing*, vol. 2. Academic press London, 1988.

[17] M. D. LaMar, J. Xin, and Y. Qi, "Signal processing of acoustic signals in the time domain with an active nonlinear nonlocal cochlear model," *Signal processing*, vol. 86, no. 2, pp. 360–374, 2006.

[18] S. J. Elliott, E. M. Ku, and B. Lineton, "A state space model for cochlear mechanics," *The Journal of the Acoustical Society of America*, vol. 122, no. 5, pp. 2759–2771, 2007.

[19] S. T. Neely, "Finite difference solution of a two-dimensional mathematical model of the cochlea," *The Journal of the Acoustical Society of America*, vol. 69, no. 5, pp. 1386–1393, 1981.

[20] S. T. Neely and D. Kim, "A model for active elements in cochlear biomechanics," *The Journal of the Acoustical Society of America*, vol. 79, no. 5, pp. 1472–1480, 1986.

[21] Y. Kim and J. Xin, "A two-dimensional nonlinear nonlocal feed-forward cochlear model and time domain computation of multitone interactions," *Multiscale Modeling & Simulation*, vol. 4, no. 2, pp. 664–690, 2005.

[22] D. Bertaccini and R. Sisto, "Fast numerical solution of nonlinear nonlocal cochlear models," *Journal of Computational Physics*, vol. 230, no. 7, pp. 2575–2587, 2011.

[23] M. Filo, F. Karameh, and M. Awad, "Order reduction and efficient implementation of nonlinear nonlocal cochlear response models," *Biological cybernetics*, vol. 110, no. 6, pp. 435–454, 2016.

[24] T. A. Driscoll, "Automatic spectral collocation for integral, integro-differential, and integrally reformulated differential equations," *Journal of Computational Physics*, vol. 229, no. 17, pp. 5980–5998, 2010.

[25] E. M. Ku, S. J. Elliott, and B. Lineton, "Statistics of instabilities in a state space model of the human cochlea," *The Journal of the Acoustical Society of America*, vol. 124, no. 2, pp. 1068–1079, 2008.

[26] S. Khanna and D. Leonard, "Measurement of basilar membrane vibrations and evaluation of the cochlear condition," *Hearing research*, vol. 23, no. 1, pp. 37–53, 1986.

[27] T. Ren, "Longitudinal pattern of basilar membrane vibration in the sensitive cochlea," *Proceedings of the National Academy of Sciences*, vol. 99, no. 26, pp. 17101–17106, 2002.

[28] T. Ren, W. He, and P. G. Gillespie, "Measurement of cochlear power gain in the sensitive gerbil ear," *Nature communications*, vol. 2, p. 216, 2011.

[29] N. P. Cooper, "An improved heterodyne laser interferometer for use in studies of cochlear mechanics," *Journal of neuroscience methods*, vol. 88, no. 1, pp. 93–102, 1999.

[30] S. Särkkä and J. Hartikainen, "Infinite-dimensional kalman filtering approach to spatio-temporal gaussian process regression.," in *AISTATS*, vol. 22, pp. 993–1001, 2012.